



GR Focus Review

Establishing the link between Permian volcanism and biodiversity changes: Insights from geochemical proxies

Jun Chen ^{a,*}, Yi-gang Xu ^{a,b,c,*}^a State Key Laboratory of Isotope Geochemistry, Guangzhou Institute of Geochemistry, Chinese Academy of Sciences, Guangzhou 510640, China^b Institutions of Earth Sciences, Chinese Academy of Sciences, Beijing 100029, China^c College of Earth and Planetary Sciences, University of Chinese Academy of Sciences, Beijing 100049, China

ARTICLE INFO

Article history:

Received 14 January 2019

Received in revised form 23 March 2019

Accepted 14 April 2019

Available online xxxx

Handling Editor: M. Santosh

Keywords:

Permian

Large igneous province

Continental arc volcanism

Environmental change

Mass extinction

Geochemical proxies

ABSTRACT

Current understanding of biodiversity changes in the Permian is presented, especially the consensus and disagreement on the tempo, duration, and pattern of end-Guadalupian and end-Permian mass extinctions. The end-Guadalupian mass extinction (EGME; i.e., pre-Lopingian crisis) is not as severe as previously thought. Moreover, the turnovers of major fossil groups occurred at different temporal levels, therefore the total duration of the end-Guadalupian mass extinction is relatively extended. By comparison, fossil records constrained with high-precision geochronology indicate that the end-Permian mass extinction (EPME) was a single-pulse event and happened geologically instantaneous. Variation of geochemical proxies preserved in the sedimentary records is important evidence in examining potential links between volcanisms and biodiversity changes. Some conventional and non-traditional geochemical proxy records in the Permian show abrupt changes across the Permian-Triassic boundary, reflecting climate change, ocean acidification and anoxia, carbon cycle perturbation, gaseous metal loading, and enhanced continental weathering. These, together with the stratigraphic coincidence between volcanic ashes and the end-Permian mass extinction horizon, point to large-scale volcanism as a potential trigger mechanism.

To further define the nature of volcanism which was responsible for global change in biodiversity, main characteristics of four Permian large igneous provinces (LIPs; i.e., Tarim, Panjal, Emeishan, and Siberian) are compared, in terms of timing and tempo, spatial distribution and volume, and magma-wall rock interactions. The comparison indicates that volcanic fluxes (i.e., eruption rates) and gas productions are the key features distinguishing the Siberian Traps from other LIPs, which also are the primary factors in determining the LIP's potential of affecting Earth's surface system. We find that the Siberian Traps volcanism, especially the switch from dominantly extrusive eruptions to widespread sill intrusions, has the strongest potential for destructive impacts, and most likely is the ultimate trigger for profound environmental and biological changes in the latest Permian-earliest Triassic. The role of Palaeotethys subduction-related arc magmatism cannot be fully ruled out, given its temporal coincidence with the end-Permian mass extinction. As for the Emeishan LIP, medium volcanic flux and gas emission probably limited its killing potential, as evident from weak changes in geochemical proxies and biodiversity. Because of its long-lasting but episodic nature, the Early Permian magmatism (e.g., Tarim, and Panjal) may have played a positive role in affecting the contemporaneous environment, as implicated by coeval progressive climate warming, termination of the Late Palaeozoic Ice Age (LPIA), and flourishing of ecosystems.

© 2019 International Association for Gondwana Research. Published by Elsevier B.V. All rights reserved.

Contents

1. Introduction	69
2. Permian timescale	69
3. Permian biodiversity changes and mass extinctions	71
4. Variation of geochemical proxies in the Permian	71
4.1. Cisuralian	73

* Corresponding authors at: State Key Laboratory of Isotope Geochemistry, Guangzhou Institute of Geochemistry, Chinese Academy of Sciences, Guangzhou 510640, China.
E-mail addresses: junchen@gig.ac.cn (J. Chen), yigangxu@gig.ac.cn (Y. Xu).

4.2.	Late Guadalupian-early Lopingian	74
4.3.	Latest Permian-Early Triassic	75
4.3.1.	Carbon isotopes	75
4.3.2.	Oxygen isotopes	77
4.3.3.	Calcium isotopes	78
4.3.4.	Boron isotopes	78
4.3.5.	Redox proxies (Fe, Mo, U)	79
4.3.6.	Hg, Zn, and Ni anomalies	79
4.3.7.	Terrestrial impacts and weathering proxies	81
5.	Permian LIPs as potential causes of environmental/biodiversity changes	82
5.1.	Tarim Large Igneous Province	82
5.2.	Panjil Traps	82
5.3.	Emeishan Large Igneous Province	83
5.4.	Siberian Traps	84
5.5.	Examining the LIP-mass extinction association	85
6.	Arc magmatism and the end-Permian mass extinction	88
7.	Conclusion	89
	Acknowledgements	89
	References	89

1. Introduction

To better understand how life on Earth has responded to natural and anthropogenic forcing over the geologically ancient and recent past, it is fundamental to view Earth as a complex system of interacting components, or as a collection of many open, interacting (and often overlapping) sub-systems. Three major geosystems constitute the Earth System: the geodynamo system involves interactions between the inner and outer cores; the plate tectonic system involves interactions among the lithosphere, asthenosphere, and deep mantle; and the climate system involves interactions among the atmosphere, hydrosphere, biosphere, cryosphere, and lithosphere (Grotzinger and Jordan, 2014). Volcanism, on the other hand, penetrates these three major geosystems, as it constitutes the entire sequence of events from melting to eruption. Therefore, volcanism, especially major eruptions that generate LIPs and occur at continental margins, can be viewed as a vital link between geodynamic processes in Earth's deep interior and surface system evolution, particularly the lithosphere, atmosphere and biosphere.

Quantitative analyses of fossil records have long revealed that five major mass extinctions ("Big Five"; i.e., the end-Ordovician, late Devonian Frasnian/Famennian, end-Permian, end-Triassic, end-Cretaceous mass extinctions) occurred in the Phanerozoic (Sepkoski, 1981; Raup and Sepkoski, 1982), along with many other biotic crisis with smaller magnitude of diversity loss (Peters and Foote, 2001; Bambach, 2006; Alroy et al., 2008; Stanley, 2016). The temporal coincidence between LIPs and mass extinctions (Courtillot, 1999; Wignall, 2001; Courtillot and Renne, 2003) has resulted in a plethora of multidisciplinary studies seeking to understand biotic crisis associated with massive volcanism through environmental changes. Progressive advances in reconstruction of the Phanerozoic biodiversity patterns, high-precision geochronology, and conventional and non-traditional geochemical proxies have provided rigorous tools for constantly scrutinizing the LIP/extinction association. Recent assessments on mass extinctions and their causes (Rong and Huang, 2014; Bond and Grasby, 2017; Shen and Zhang, 2017) suggested that the link between LIPs and mass extinctions might not be straightforward as previously thought (Bond and Wignall, 2014; Bond and Grasby, 2017; Ernst and Youbi, 2017). Recently, continental arc magmatism has been proposed as an alternative factor to potentially trigger major climatic and environmental changes throughout Earth's history (He et al., 2014; Lee et al., 2015; McKenzie et al., 2016). Thus, a conservative but logical strategy of testing the volcanism/extinction relationship is highly desired.

In this review, we will introduce current understanding of the biodiversity changes in the Permian, especially the consensus and

disagreement on the tempo, duration, and pattern of end-Guadalupian and end-Permian mass extinctions. This is followed by a detailed evaluation of various conventional and non-traditional geochemical proxy records in the Permian, with special interests on proxies that are closely associated with major environmental changes such as climate warming or cooling, ocean acidification and anoxia, or indicative of massive volcanic eruptions (e.g., carbon cycle perturbation, gaseous metal loading, and continental weathering). Then we will show evidence for the decisive role played by massive volcanism in environmental and biological changes in the Permian. Finally attempts are made to decipher whether plume-generated LIP volcanism, or Palaeotethys arc magmatism, or both are responsible for the Permian biodiversity changes.

2. Permian timescale

Temporal correlation is the first-order evidence to establish the LIP/extinction associations (Rampino and Stothers, 1988; Wignall, 2001; Courtillot and Renne, 2003). The current Permian chronostratigraphic scale (Fig. 1) advocated by the Subcommission on Permian Stratigraphy consists of three series and nine stages: the Cisuralian (lower Permian) – Asselian, Sakmarian, Artinskian, and Kungurian; the Guadalupian (middle Permian) – Roadian, Wordian, and Capitanian; the Lopingian (upper Permian) – Wuchiapingian and Changhsingian. High-precision U–Pb geochronology in the past two decades (Bowring et al., 1998; Mundil et al., 2001, 2004; Ramezani et al., 2007; Shen et al., 2011a; Schmitz and Davydov, 2012; Burgess et al., 2014; Zhong et al., 2014; Wu et al., 2017; Ramezani and Bowring, 2018) has shown significant progress in refining the Permian timescale, through integration with biostratigraphic, magnetostratigraphic, and chemostratigraphic tools (Lucas and Shen, 2018a). A series of ten ages currently constrain the Permian, including 298.90 ± 0.15 Ma for the Carboniferous-Permian boundary (i.e., base-Asselian), 293.52 ± 0.17 Ma for the base-Sakmarian, 290.10 ± 0.26 Ma for the base-Artinskian, 283.5 ± 0.6 Ma for the base-Kungurian, 272.95 ± 0.11 Ma for the base-Roadian (i.e., Cisuralian-Guadalupian boundary), 268.8 ± 0.5 Ma for the base-Wordian, 265.1 ± 0.4 Ma for the base-Capitanian, 259.1 ± 0.5 Ma for the base-Wuchiapingian (i.e., Guadalupian-Lopingian boundary; GLB), 254.14 ± 0.07 Ma for the base-Changhsingian, and 251.902 ± 0.024 Ma for the Permian-Triassic boundary (PTB; i.e., base-Induan).

It is necessary to point out that, among the ten ages defining the stage boundaries of the Permian, the age 259.1 ± 0.5 Ma for the GLB is by definition different from the others, because it is a CA-TIMS (chemical abrasion-thermal ionization mass spectrometry) weighted mean U–Pb date from a felsic ignimbrite in the uppermost part of the

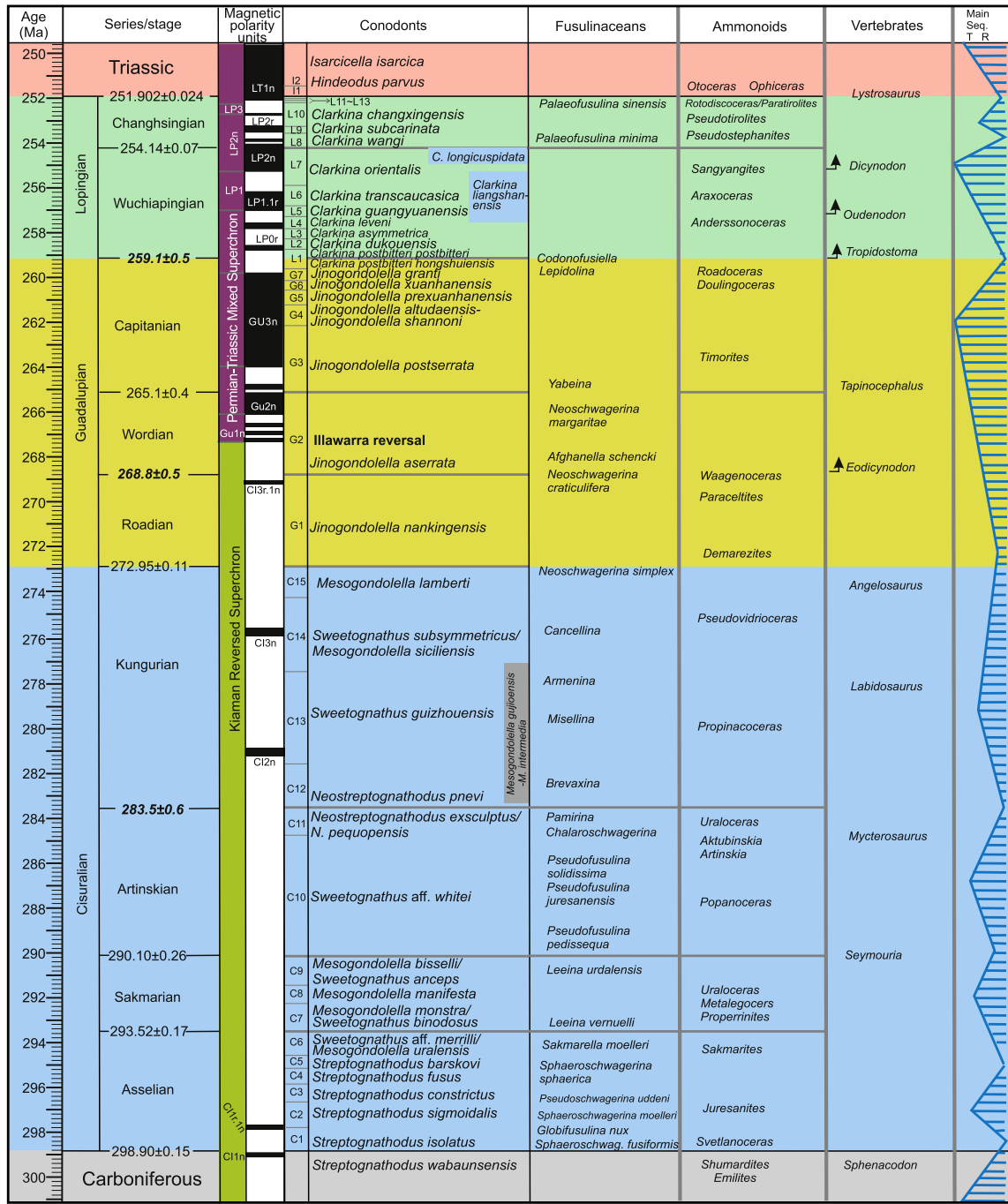


Fig. 1. Current Permian chronostratigraphic framework advocated by the Subcommission on Permian Stratigraphy; details can be found in Lucas and Shen (2018b) and Shen et al. (2019b). Boundary ages in bold and italic (base-Kungurian, base-Wordian, and base-Wuchiapingian) indicate that they are based on indirect calibrations (Henderson et al., 2012; Ramezani and Bowring, 2018).

Emeishan LIP lava succession (Zhong et al., 2014), not as in normal situation when the stage boundary ages are dated and calibrated from volcanic ash layers deposited in marine sedimentary sequences. Prior to the official ratification of the GSSP (Global Stratotype Section and Point) for the base-Wuchiapingian at the Penglaitan section in Guangxi, South China, multiple attempts have been made on dating tuff beds around the GLB, but no reliable ages have been acquired (Jin et al., 2006). Zhong et al. (2013) studied the mineralogy, geochemistry, and geochronology of six layers of claystones around the GLB at Penglaitan, and confirmed that these claystones are clastic in origin and not suitable for age determination. Using in situ SIMS (secondary ion mass spectrometry) U-Pb dating method, Qiu et al. (2016) reported zircon

U-Pb ages of 257.1 ± 2.2 and 257.0 ± 4.2 Ma for two bentonite layers above the GLB, which are stratigraphically equivalent to samples PLT-4 and PLT-5 in Zhong et al. (2013), and suggested 258.6 Ma as the age of the GLB. Given the large uncertainties of SIMS zircon U-Pb dates (Qiu et al., 2016), and those layers are not acidic tuff, but most likely detrital or clastic sedimentary rocks (Zhong et al., 2013), the recommendation of 258.6 Ma as the age of GLB (Qiu et al., 2016) is questionable, and it is by no means an improvement for solving the GLB age in marine sedimentary sequences.

However, several lines of evidence from the Penglaitan GSSP section, such as mineral components, REE pattern, $\text{Al}_2\text{O}_3/\text{TiO}_2$ and Th/Sc ratios (Zhong et al., 2013), indicated that the claystone about 60 cm below

the GLB was derived from a mafic source that is genetically associated with the Emeishan LIP, implying the synchronicity between the GLB and the Emeishan LIP volcanism. Therefore, the high-precision age of 259.1 ± 0.5 Ma from a felsic ignimbrite in the uppermost part of the Emeishan LIP lava succession in Dali, Yunnan (Zhong et al., 2014) can be used as an indirect constraint on the GLB, on prerequisites that the GLB claystones in SW China (e.g., Chaotian, and Penglaitan) were derived from the uppermost part of the lava succession in the Emeishan LIP, and the felsic member in the uppermost part of the Emeishan flood basalts and the GLB claystones lie on an isochron horizon (He et al., 2007, 2010; Shen et al., 2010; Zhong et al., 2014).

3. Permian biodiversity changes and mass extinctions

Our understanding of biodiversity changes throughout the Permian as a whole is less than ideal. Early studies (Sepkoski, 1981; Raup and Sepkoski, 1982) and recent progresses (Peters and Foote, 2001; Bambach, 2006; Alroy et al., 2008; Hannisdal and Peters, 2011; Zaffos et al., 2017) on global marine biodiversity changes in deep-time mostly aimed at the full Phanerozoic with a temporal resolution of ~10 Myr (million years) time bins, which is too coarse to reveal details of biodiversity changes and potential connections with LIP eruptions and subsequent environmental deterioration. Nonetheless, it is generally accepted that the Permian started with a substantial rise and ended with a sudden drop in biodiversity, as shown in the long-term trends (Peters and Foote, 2001; Alroy et al., 2008; Zaffos et al., 2017). Other studies specifically dealing with the Permian usually focused on individual fossil groups, such as brachiopods (Shen and Shi, 1996, 2002; Shen et al., 2006), corals (Wang and Sugiyama, 2000; Wang et al., 2006), ammonoids (Villier and Korn, 2004; Brayard et al., 2009; Leonova, 2009, 2011, 2016), and fusulinids (Groves and Wang, 2009, 2013; Zhang and Wang, 2018). Composite biodiversity patterns based on 1450 species of 16 fossil clades (cephalopods, brachiopods, foraminifers, fusulinids, conodonts, corals, bivalves, radiolarians, bryozoans, gastropods, ostracods, fishes, calcareous algae, spores and pollens, and plants) from 18 sections in South China and northern peri-Gondwanan region (Shen et al., 2011a; Wang et al., 2014) shown significant progresses in terms of temporal resolution and comprehensiveness. However, their dataset only covered the time span from the late Guadalupian to early Triassic (Wang et al., 2014).

Biodiversity changes from the late Carboniferous-early Triassic (Fig. 2) can be roughly subdivided into five intervals, interrupted by two mass extinctions occurred at the end-Guadalupian and end-Permian. A biodiversification event occurred in the late Carboniferous-Early Permian (Cisuralian), followed by a moderate decline in biodiversity, and fluctuation until around the GLB. After the end-Guadalupian mass extinction (i.e., pre-Lopingian crisis), biodiversity gradually increases until a sudden drop in the end-Permian, followed by a minor radiation in the Early Triassic.

Determining the tempo and duration of mass extinction is fundamental to understanding its cause(s) (Erwin, 2006, 2014), and it is decided by two factors: stratigraphy/palaeontology, and geochronology. The end-Guadalupian mass extinction has been recognized as a major biotic crisis separated from the end-Permian mass extinction for nearly three decades (Erwin, 1990; Jin, 1991, 1993; Jin et al., 1994; Stanley and Yang, 1994). However, as more and more evidence emerged in recent years, current views on this biotic crisis to some extent have changed. The extinction rate at the end-Guadalupian was ranked very high in the early studies, only lower than the end-Permian and end-Ordovician mass extinctions (Sepkoski, 1996; Bambach et al., 2004; Isozaki and Servais, 2018). Re-evaluation of the Phanerozoic taxonomic-severity (McGhee et al., 2013) suggested that the end-Guadalupian mass extinction is not severe as previously thought, and only happened at the community level and taxonomically selective (Shen and Shi, 2002; Clapham et al., 2009; McGhee et al., 2013; Clapham, 2015). In South China, especially in the Penglaitan-Tieqiao

area of Guangxi where the sedimentary record across the GLB is completely preserved, fossil evidence suggests that the turnover of major groups (e.g., rugose corals, brachiopods, fusulinids, conodonts, bivalves, and ammonoids) occurred at different temporal levels (Shen and Shi, 2009). If taking all the faunal evidence into account, the end-Guadalupian mass extinction most likely occurred in the latest Capitanian-earliest Wuchiapingian, in the interval between conodont *Jinogondolella xuanhanensis*-*Clarkina dukouensis* zones (Fig. 2). Direct geochronological constraint on the timing and duration of the end-Guadalupian mass extinction is problematic. Although the base-Capitanian was calibrated as 265.1 ± 0.4 Ma from its GSSP section at Nipple Hill, Guadalupian Mountains National Park, West Texas (Bowring et al., 1998; Ramezani and Bowring, 2018), there are uncertainties regarding the age of the GLB, as the temporally used age 259.1 ± 0.5 Ma is indirect constraint based on a U—Pb date from a felsic ignimbrite in the uppermost part of the Emeishan LIP lava succession (Zhong et al., 2014). Therefore, durations of the Capitanian conodont zones (Fig. 2) cannot be confidently calculated, although a rough estimation would suggest that the end-Guadalupian mass extinction most likely lasted for >1 Myr. A different view on the timing and duration of the end-Guadalupian mass extinction also exists. Based on the ranges of foraminifers and calcareous algae, a major negative excursion (>5‰) in $\delta^{13}\text{C}_{\text{carb}}$, and their relative positions to the Emeishan flood basalt units in western Guizhou, a middle-Capitanian mass extinction around the *Jinogondolella shannoni*-*J. altudaensis* zonal boundary, associated with the Emeishan volcanism and severe disturbance of carbon cycle was proposed (Wignall et al., 2009; Bond et al., 2010a, 2010b).

In contrast, the tempo and duration of the end-Permian mass extinction are well constrained, mainly benefit from high-resolution conodont biostratigraphy (Yuan et al., 2014, 2019) and high-precision U—Pb geochronology (Shen et al., 2011a, 2019a; Burgess et al., 2014). Statistical analyses of fossil records at the Meishan GSSP section using confidence interval approach (Jin et al., 2000), and on a composition of 18 sections across South China and the northern peri-Gondwanan region using constrained optimization (CONOP) method (Shen et al., 2011a; Wang et al., 2014), revealed a single pulse of mass extinction, beginning at the top of Bed 24 and just below Bed 25 and with some survival taxa lingered on no later than Bed 28 when projecting onto the Meishan section. The progressive development in zircon U—Pb geochronology and its applications at the Meishan section, especially on Beds 25 and 28 (Bowring et al., 1998; Mundil et al., 2001, 2004; Shen et al., 2011a; Burgess et al., 2014), provide a temporal framework for the end-Permian mass extinction, with the latest high-precision dating from Burgess et al. (2014) suggesting the extinction occurred between 251.941 ± 0.037 and 251.880 ± 0.031 Ma, with a maximum duration of 61 ± 48 kyr (thousand years). Integrated high-precision U—Pb geochronology, biostratigraphy, and chemostratigraphy from a highly expanded PTB section at Penglaitan, Guangxi, South China (Shen et al., 2019a) indicated a sudden end-Permian mass extinction that occurred at 251.939 ± 0.031 Ma, which is temporally coincident with the extinction recorded in Bed 25 of the Meishan section (Burgess et al., 2014). More importantly, fossil data from the expanded Penglaitan section suggested that the mass extinction was nearly instantaneous and no evidence of a decline of biodiversity existed prior to the extinction interval that was limited to 31 ± 31 kyr, and no Permian-type species survived the extinction (Shen et al., 2019a). Other studies (Yin et al., 2007; Song et al., 2013) argued for two or more pulses of extinction during the latest Permian-earliest Triassic. However, this does not change the fact that the onset of the EPME happened at an equivalent level to the top of Bed 24 and just below Bed 25 at Meishan.

4. Variation of geochemical proxies in the Permian

In general, massive volcanism potentially can affect the environments and ecosystems through many complex pathways (Self et al., 2006, 2014; Bond and Grasby, 2017; Ernst and Youbi, 2017), depending

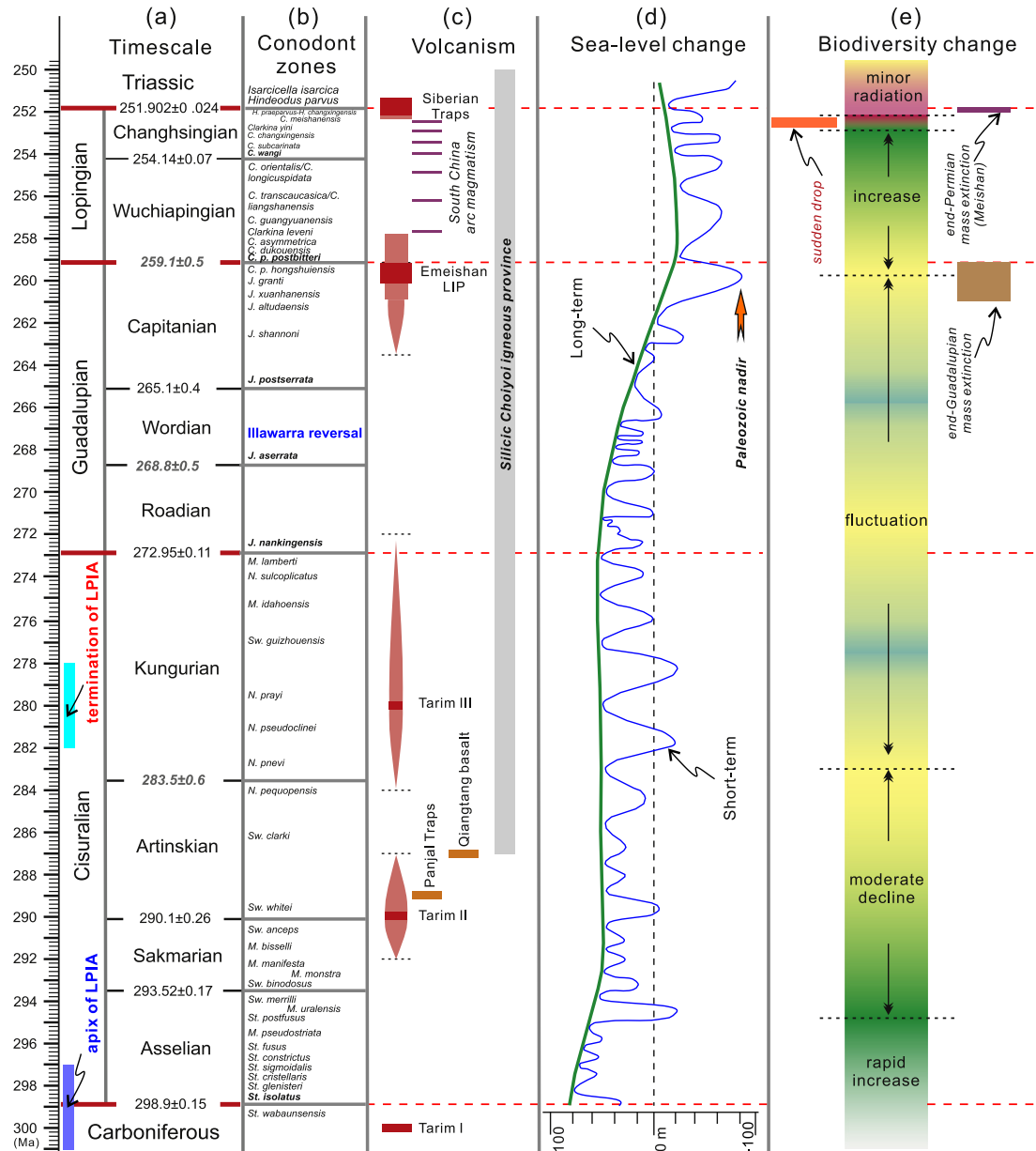


Fig. 2. Biodiversity changes from the late Carboniferous to early Triassic, with two mass extinctions occurred at the end-Gadalupian and end-Permian, and correlation with major volcanic events including four LIPs (Tarim, Panjal, Emeishan, and Siberian) and the long-lasting Choiyoi silicic igneous province. Long-term and short-term sea-level changes are also presented (Haq and Schutter, 2008); timing of the apex and termination of the Late Palaeozoic Ice Age (LPIA) are according to Chen et al. (2018) and Chen et al. (2013), respectively; timing of the Illawarra reversal is according to Hounslow and Balabanov (2018).

on the style (explosive vs. effusive vs. intrusive), timing and duration of each phase, volcanic products (e.g., pyroclasts, lava, CO₂, SO₂, halogen, sulfate aerosol, and gaseous toxic metals), and feedback in the lithosphere, atmosphere and biosphere. Examining potential links between massive volcanism and biodiversity changes, especially mass extinctions, rely heavily on continuous and high-resolution geochemical records preserved in sedimentary rocks, preferably in marine settings.

The late Permian-early Triassic interval has been intensively studied for many years, and consequently produced a plethora of geochemical evidence suggesting the causal relationship between the Siberian Traps eruptions and the end-Permian mass extinction. By comparison, the Emeishan LIP and contemporaneous environmental and biological changes are less well understood due to inadequate temporal controls (Ramezani and Bowring, 2018). Moreover, a pivotal part of strata (conodont *Jinogondolella xuanhanensis*-*Clarkina dukouensis* zones) for deciphering the connections between the Emeishan LIP and end-

Guadalupian mass extinction (Fig. 2) are often absent in most regions of South China (Shen et al., 2019b) due to large-scale regression during the middle-late Guadalupian (Haq and Schutter, 2008). For the Cisuralian, with the base-Artinskian and base-Kungurian GSSPs remaining to be established, the chronostratigraphic framework is yet to be completed. Therefore, palaeoenvironmental records in various palaeogeographic realms such as southern Urals (type locality of the Cisuralian), South China, North American midcontinent, and Gondwana often cannot be correlated with confidence, and whether a common source such as massive volcanism was responsible for the environmental and biological changes during the late Carboniferous-early Permian (Cisuralian) is largely uncertain.

In this section, we summarize some of the recent advances in investigating the variation of geochemical proxies preserved in sedimentary sequences in the Cisuralian, around the GLB, and across the PTB interval. Since studies on the Cisuralian and GLB interval are inadequate

comparing to the extensively investigated PTB interval, geochemical proxies covered in each period are different and uneven. Moreover, we should explain herein that, even for the PTB interval, the geochemical proxies assessed are not meant to be comprehensive without omissions. Instead, we focus on proxies that are closely associated with the three highly suspected kill mechanisms (i.e., climate change, ocean acidification, and anoxia), and most likely linked with massive volcanic eruptions (e.g., carbon cycle perturbation, gaseous metal loading, and continental weathering).

4.1. Cisuralian

The Cisuralian carbon isotopes data measured on brachiopod shells and whole rock carbonates have been reported from the southern Urals, South China, North American midcontinent, Southern Alps, and Australia in a number of studies (Korte et al., 2005; Grossman et al., 2008; Tierney, 2010; Buggisch et al., 2011, 2015; Koch and Frank, 2012; Mii et al., 2012, 2013; Zeng et al., 2012; Liu et al., 2017a, 2017b, 2018; Cheng et al., 2019). Among those studied sections, only several of them have produced long-term and continuous profiles for the ~30 Myr interval from the latest Carboniferous to early Guadalupian (i.e., the maximum duration of the Early Permian LIP volcanism; Fig. 2), such as the Naqing section in Guizhou (Buggisch et al., 2011), Gongchuan section in Guangxi (Liu et al., 2017b), and Xikou section in Shaanxi (Cheng et al., 2019). Carbon isotope records based on bulk carbonates from the southern Urals (Zeng et al., 2012), Nine Mile Canyon and Rockland Ridge in Nevada (Tierney, 2010), Orogenome Basin in New Mexico (Koch and Frank, 2012), and brachiopods from North American midcontinent, Russian Platform (Grossman et al., 2008), and Western Australia (Mii et al., 2012, 2013) are also important tie-points for global correlation, but those profiles are either low in temporal resolution, incomplete, or composites from multiple sections. Comparisons of global carbon isotope records (Buggisch et al., 2015; Liu et al., 2017b; Cheng et al., 2019) suggest that $\delta^{13}\text{C}_{\text{carb}}$ patterns during the latest

Carboniferous-early Guadalupian are highly variable. Even regionally, the overall trends in the continuous profiles from Naqing (Buggisch et al., 2011), Gongchuan (Liu et al., 2017b), and Xikou (Cheng et al., 2019) in South China are different from one another. Imprecise biostratigraphic correlation, difference in depositional settings, and diagenetic effects could be the potential causes. Nonetheless, continuous and high-resolution data from the Naqing section (Fig. 3) demonstrated that $\delta^{13}\text{C}_{\text{carb}}$ trend started with a high plateau (>5‰) in the Gzhelian-early Asselian, followed by an overall two-step decrease that are most prominent in the late Asselian and early Kungurian, and ended with a rebound from ~2‰ in the early-middle Kungurian to ~5‰ in the early Wordian (Buggisch et al., 2011).

A continuous, long-term oxygen isotopic record measured on conodont apatite ($\delta^{18}\text{O}_{\text{apatite}}$) spanning the late Viséan to Roadian was reported from the Naqing section, Guizhou, South China (Chen et al., 2013, 2016a). The results indicated that after the maximum value occurred in the middle Bashkirian, $\delta^{18}\text{O}_{\text{apatite}}$ values show stepwise decrease during the Pennsylvanian-Cisuralian (Chen et al., 2016a). Unlike the two obvious decreases occurred in the late Bashkirian and Gzhelian, the overall decreasing trend in the Cisuralian (Fig. 3) is smooth, suggesting a gradual warming of ~4 °C from the latest Carboniferous to earliest Guadalupian.

Coeval seawater strontium data ($^{87}\text{Sr}/^{86}\text{Sr}$ ratios) (McArthur et al., 2012; Chen et al., 2018; Wang et al., 2018b) demonstrated a long and continuous decrease (Fig. 3), with the onset constrained in the early Viséan (~303 Ma) (Chen et al., 2018) and the termination in the late Capitanian (Wang et al., 2018b). According to Wang et al. (2018b), the declining trend of $^{87}\text{Sr}/^{86}\text{Sr}$ ratios in the Cisuralian and Guadalupian probably was caused by the suppressed riverine flux into the ocean during the convergence between Gondwana and Laurussia, and the increasing input of hydrothermal flux into the ocean associated with the mid-ocean spreading in association with the formation of the supercontinent Pangaea.

Whether the widespread and episodic Early Permian LIP eruptions (e.g., Tarim, and Panjal) was associated with the $\delta^{13}\text{C}_{\text{carb}}$, $\delta^{18}\text{O}_{\text{apatite}}$,

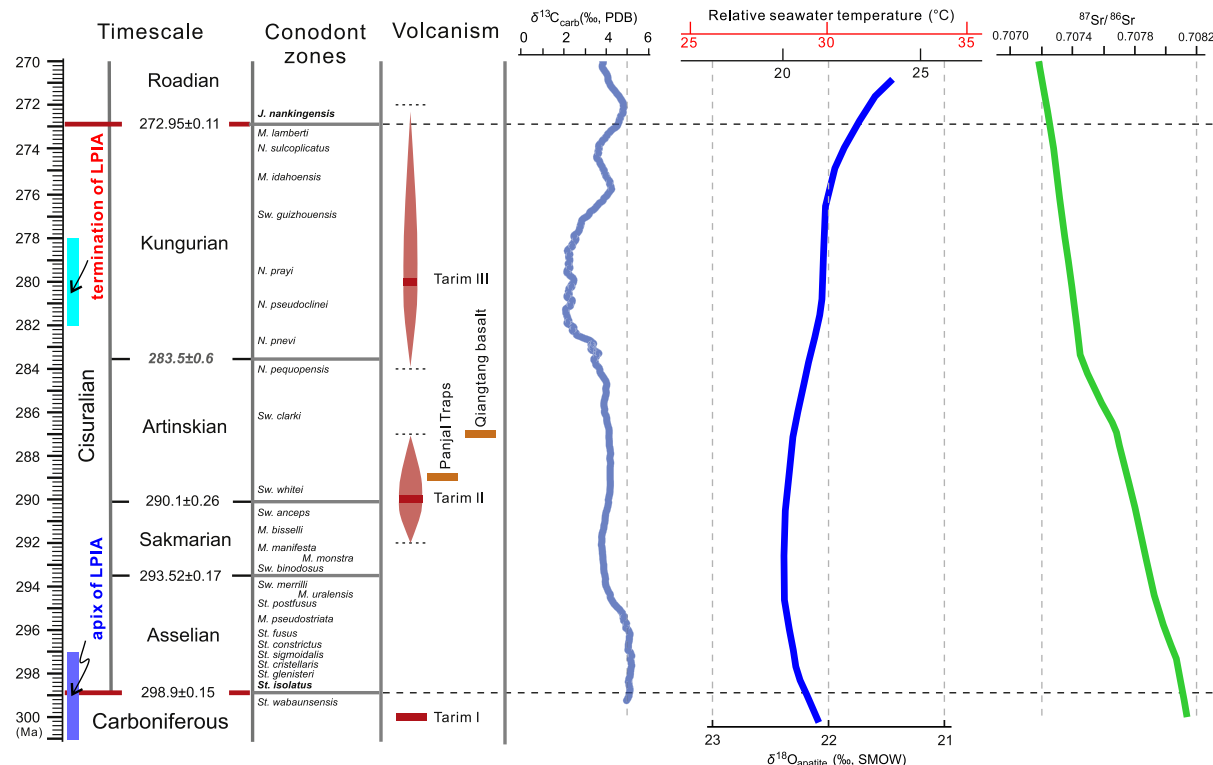


Fig. 3. Cisuralian $\delta^{13}\text{C}_{\text{carb}}$, $\delta^{18}\text{O}_{\text{apatite}}$, and $^{87}\text{Sr}/^{86}\text{Sr}$ profiles in South China. $\delta^{13}\text{C}_{\text{carb}}$ trend is based on data from the Naqing section in Guizhou (Buggisch et al., 2011); $\delta^{18}\text{O}_{\text{apatite}}$ and calculated relative seawater temperatures (black scale and red scale assume the oxygen isotopic compositions of seawater as -1‰ and +1‰, VSMOW, respectively) are also from Naqing (Chen et al., 2013); $^{87}\text{Sr}/^{86}\text{Sr}$ trend is the LOWESS fitted curve based on data from Naqing and Tieqiao sections (Wang et al., 2018b).

and $^{87}\text{Sr}/^{86}\text{Sr}$ trends is largely uncertain, as there are no obvious changes precisely corresponding to each episode of massive volcanism (Fig. 3). However, this does not rule out the possibility that the Early Permian LIP volcanism has contributed to contemporaneous environmental and biological changes, especially the gradual climate warming and flourishing of ecosystems.

4.2. Late Guadalupian-early Lopingian

Carbon isotope changes during the late Guadalupian-early Lopingian are also complicated (Bond et al., 2010b; Shen et al., 2013; Jost et al., 2014; Cao et al., 2018), particularly in the equivalent interval of conodont *Jinogondolella altudaensis*-*Clarkina postbitteri postbitteri* zones, which most likely represents the main phase of the Emeishan LIP (Fig. 4). A full understanding of the carbon isotope changes and possible association with the Emeishan LIP is hindered by several key factors. First, large scale sea-level drop (Haq and Schutter, 2008) and/or pre-eruptive uplift (He et al., 2003) resulted in a depositional hiatus on top of the Maokou Limestone with subsequent deposits of the "Wangpo Bed", which is widespread in South China and varies in the form of terrigenous clastics, coal seams, and tuff layers. Therefore, a gap usually exists in each of the carbon isotope profiles between the Maokou and Wuchiaping formations (Cao et al., 2018), with exception of the Penglaitan and Tieqiao sections (Fig. 4) (Wang et al., 2004; Chen et al., 2011; Jost et al., 2014). Second, even with assistance from conodont biostratigraphy (Sun et al., 2010; Yuan et al., 2017), there are still uncertainties in constraining the extent of the gap and correlating the carbon isotope profiles across various sections (Bond et al., 2010b; Chen et al., 2011; Jost et al., 2014; Cao et al., 2018). Third, diagenetic effects and regional litho-facies controls (Jost et al., 2014; Cao et al., 2018) have also made it difficult to identify the primary carbon cycle perturbations and potential connections with the Emeishan LIP.

Nonetheless, previous studies demonstrated that several features in the $\delta^{13}\text{C}_{\text{carb}}$ records around the Guadalupian-Lopingian transition are worth noting. A high positive plateau in $\delta^{13}\text{C}_{\text{carb}}$ values over +5‰ was

initially recognized in a mid-Panthalassan palaeo-atoll limestone in the Kamura area, Japan (Isozaki et al., 2007b). A subsequent study with longer stratigraphic coverage (Isozaki et al., 2007a) indicated that $\delta^{13}\text{C}_{\text{carb}}$ values started to rise over +4.5‰ and reached the maximum of +7.0‰ within the fusuline *Yabeina* Zone, and sustained high values over +5‰ in the overlying *Lepidolina* Zone and most of a barren interval, followed by a negative shift and a rebound in the latest Guadalupian, and a prominent negative shift above the GLB. According to their age assignments based on fusulines (Isozaki et al., 2007a, 2007b), this unique interval of high $\delta^{13}\text{C}_{\text{carb}}$ values, termed as the "Kamura event", spanned throughout almost the entire Capitanian, except for the uppermost and possibly the lowest parts, with an estimated duration of 3–4 Myr. Later finding of high $\delta^{13}\text{C}_{\text{carb}}$ values (+4 to +6‰) in the *Yabeina* Zone in the Velebit Mtn., central Croatia of European Palaeotethys, and previous reports from West Texas, East Greenland, and West Spitsbergen, enabled Isozaki et al. (2011) to argue that the "Kamura event" was global in context. High levels of marine primary productivity, high organic carbon burial rates, combined with increased terrogenous flux and accelerated oceanic circulation, were suggested as the possible causes for the "Kamura event" on a global scale (Isozaki et al., 2011). Another unusual feature is a major negative excursion (>5‰) superimposed on typically high $\delta^{13}\text{C}_{\text{carb}}$ values (+4–5‰), which was recognized at the Xiongjichang and Gouchang sections, western Guizhou in the outer zone of the Emeishan LIP, spanning the interval of conodont *Jinogondolella altudaensis*-*J. prexuanhanensis* zones (Wignall et al., 2009; Bond et al., 2010b; Sun et al., 2010). Moreover, since this sharp negative excursion is largely coincide with the first eruptive unit of the Emeishan LIP and extinction of foraminifers and calcareous algae in their studies, a middle-Capitanian mass extinction associated with the Emeishan volcanism and subsequent severe disturbance of carbon cycle was proposed (Wignall et al., 2009; Bond et al., 2010a, 2010b).

As shown in several comparisons (Chen et al., 2011; Jost et al., 2014; Cao et al., 2018), the high positive plateau in $\delta^{13}\text{C}_{\text{carb}}$ values in the *Yabeina* Zone (Isozaki et al., 2007a, 2007b, 2011) and sharp negative

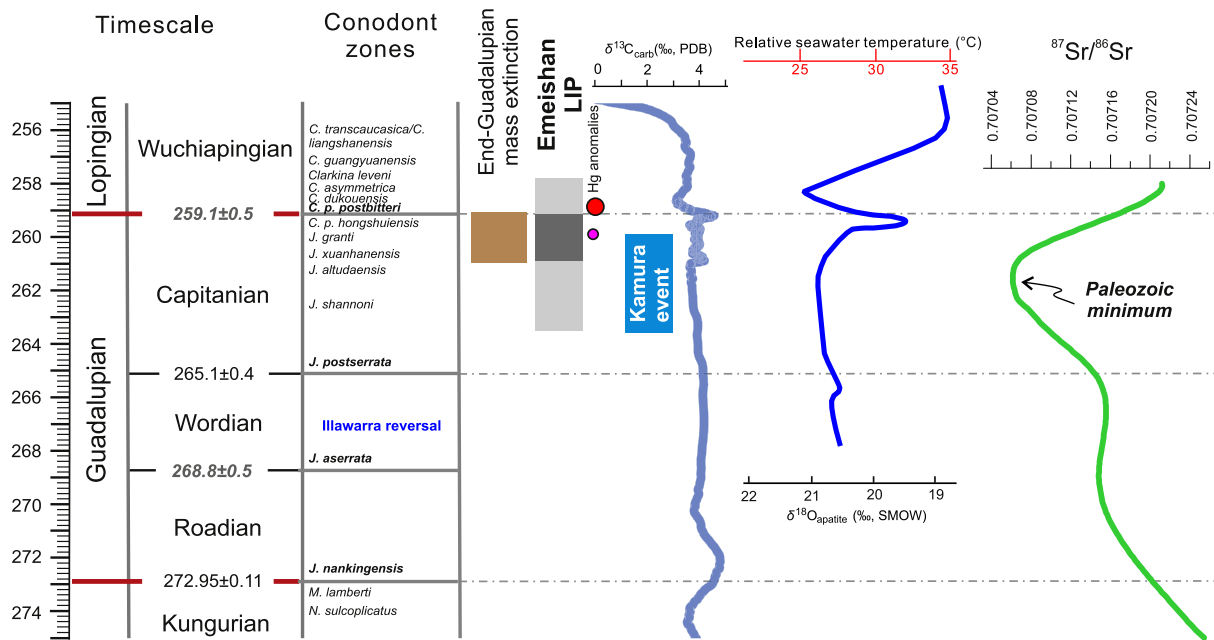


Fig. 4. $\delta^{13}\text{C}_{\text{carb}}$, $\delta^{18}\text{O}_{\text{apatite}}$, and $^{87}\text{Sr}/^{86}\text{Sr}$ profiles across the Guadalupian-Lopingian boundary, and their temporal correlation with the Emeishan LIP and end-Guadalupian mass extinction. $\delta^{13}\text{C}_{\text{carb}}$ trend is based on composite dataset from Naqing, Penglaitan, and Shangsi sections, modified after Shen et al. (2019b); the "Kamura event" (Isozaki et al., 2007a, 2007b, 2011), characterized by long-lasting high $\delta^{13}\text{C}_{\text{carb}}$ values (> +5‰), is also implicated. $\delta^{18}\text{O}_{\text{apatite}}$ and calculated relative seawater temperatures (assuming the oxygen isotopic compositions of seawater as -1‰, VSMOW) are from the Penglaitan and Tieqiao sections (Chen et al., 2011). $^{87}\text{Sr}/^{86}\text{Sr}$ trend is the LOWESS fitted curve based on data from Penglaitan and Tieqiao (Wang et al., 2018b). Total duration and main phase of the Emeishan LIP likely occurred in ~263.5–257.8 Ma (in grey) and ~260.9–259.1 Ma (in black), respectively. Purple and red circles indicate a minor and larger Hg/TOC peaks (i.e., Hg anomalies) found near the top of *Jinogondolella granti* Zone (Bed 6b) and in the *Clarkina postbitteri postbitteri*-*C. dukouensis* zones at the Penglaitan section (Huang et al., 2019b), respectively.

excursion in the *Jinogondolella altudaensis*-*J. prexuanhanensis* zones (Wignall et al., 2009; Bond et al., 2010b) can rarely be confirmed in terms of the pattern and magnitude from most of the studied sections covering the Capitanian-Wuchiapingian strata. Therefore, local depositional environments, regional litho-facies controls and diagenetic effects (Jost et al., 2014; Cao et al., 2018) most likely have profound impacts on the $\delta^{13}\text{C}_{\text{carb}}$ records.

Calcium isotopes ($\delta^{44/40}\text{Ca}$) analyzed on bulk carbonates (Penglaitan and Chaotian in South China, and Köselerlik Tepe in Turkey) and conodont apatite (only at Penglaitan) were presented in Jost et al. (2014) to constrain the cause of a negative excursion in $\delta^{13}\text{C}_{\text{carb}}$ across the GLB (Fig. 4), as the carbon and calcium cycles are coupled via CaCO_3 burial. The coupled $\delta^{44/40}\text{Ca}$ and $\delta^{13}\text{C}_{\text{carb}}$ records (Jost et al., 2014) showed that there is no consistent pattern among studied sections, indicating that changes at each section are not related to disturbances in global carbon and calcium cycles, and any environmental perturbations at the end-Guadalupian were most likely small, which are compatible with emerging palaeobiological evidence suggesting that the end-Guadalupian mass extinction was not severe as originally thought.

Oxygen isotopic compositions of conodont apatite during the late Guadalupian-earliest Lopingian at the Penglaitan and Tieqiao sections were studied by Chen et al. (2011). According to their results (Fig. 4), warming of about 4 °C occurred in the late Capitanian (*Jinogondolella postserrata* to *J. granti* zones), followed by cooling of about 6–8 °C across the GLB and in the earliest Wuchiapingian, and again significant warming of ~10 °C in the Wuchiapingian (*Clarkina dukouensis* to *C. liangshanensis* zones). An alternative explanation was also proposed for the observed changes in $\delta^{18}\text{O}_{\text{apatite}}$ values, as changes in sea-level seem to parallel reconstructed seawater temperatures, suggesting that changes in water depth may also contributed to the observed temperature changes, in addition to a sole climatic effect resulted from the main phase of the Emeishan LIP volcanism (Chen et al., 2011).

Sr isotopes ($^{87}\text{Sr}/^{86}\text{Sr}$ ratios) in seawater, either measured from bulk carbonate or brachiopod calcite and conodont apatite, essentially reflect the relative change in continental-derived riverine flux and mantle-derived hydrothermal flux into the ocean, and potentially can be used to identify geological and climatic events. A highly distinct geochemical feature in the Permian is the progressive and prominent decrease in $^{87}\text{Sr}/^{86}\text{Sr}$ ratios during the early-middle Permian and reaching the Paleozoic minimum around the GLB (Fig. 4), which has long been recognized (Burke et al., 1982). Recent high-resolution records identified the onset of this prominent decrease around the conodont *Idiognathodus simulator* Zone of the early Gzhelian (Chen et al., 2018), and the termination (i.e., the Paleozoic minimum) around the *Jinogondolella shannoni*/*J. altudaensis* and *J. xuanhanensis* zones of the late Capitanian (Wang et al., 2018b). The timing of the turning point, however, is relatively more important. Since the subsequent increase in $^{87}\text{Sr}/^{86}\text{Sr}$ ratios largely coincides with the main pulse of the Emeishan LIP magmatism and seawater temperature changes (Fig. 4), a common volcanic trigger is highly plausible. However, it is worth noting that the change in seawater temperatures consists of three steps (i.e., warming, cooling, and again warming) (Chen et al., 2011), not a continuous decrease as expected from an enhanced continental weathering condition, therefore the balance between CO_2 emission due to the Emeishan LIP volcanism and CO_2 consumption due to enhanced continental weathering and subsequent increased riverine flux, most likely have rapidly shifted during the late Capitanian-early Wuchiapingian. Independent confirmation with other geochemical proxies in the future hopefully can provide more details on the underlying mechanism(s) governing the environmental changes around the GLB.

Pyrite framboid sizes and sulfur isotopes have been applied to indicate redox condition changes during the late Capitanian-early Wuchiapingian (Yan et al., 2013; Zhang et al., 2015; Wei et al., 2016). Comparative multiple sulfur isotopes data from the Penglaitan and Tieqiao sections in South China and the EF section in the Apache

Mountains, West Texas (Zhang et al., 2015) demonstrated a pronounced decrease in $\delta^{34}\text{S}$ near the GLB, and the common occurrence of negative $\Delta^{33}\text{S}$ for ^{34}S -depleted samples, suggesting a causal link between widespread shoaling of sulfidic waters and the end-Guadalupian mass extinction.

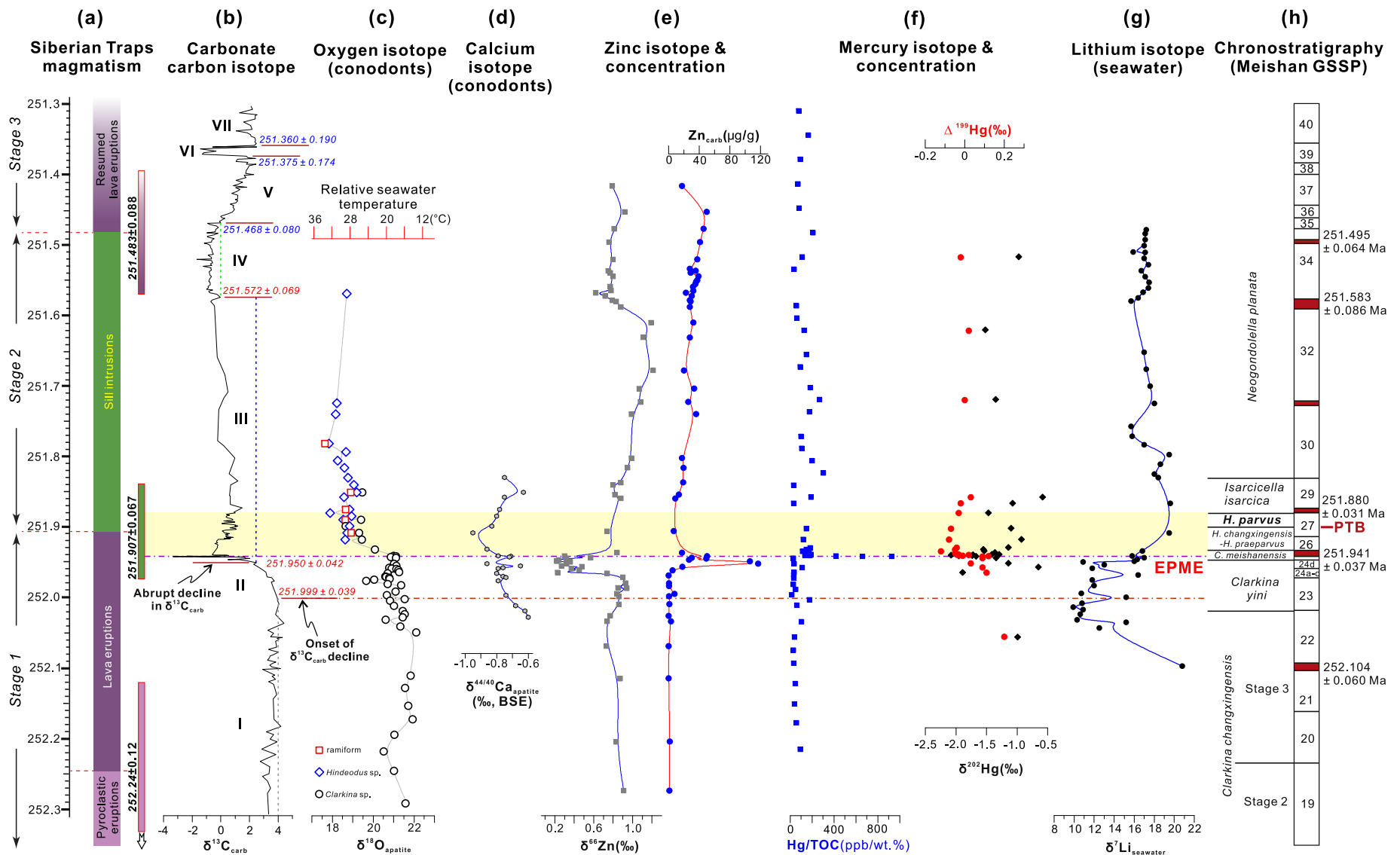
Ever since abnormal mercury concentrations were found in the Neoproterozoic cap carbonates in Brazil, and mercury anomalies were suggested as proxies of enhanced volcanic activity (Sial et al., 2010), mercury proxy has been increasingly used as a geochemical signal of LIP volcanism recorded in the sediments, as shown in some representative studies (Sanei et al., 2012; Font et al., 2016; Sial et al., 2016; Thibodeau et al., 2016; Charbonnier and Follmi, 2017; Percival et al., 2017; Keller et al., 2018; Racki et al., 2018; Wang et al., 2018c; Zheng et al., 2018; Huang et al., 2019b), or in a recent comprehensive review (Percival et al., 2018). Mercury anomalies across the GLB have been reported from the Festningen section in Spitsbergen (Grasby et al., 2016), Danyang section in central eastern Korea (Kwon et al., 2019), and the Penglaitan GSSP section in South China (Huang et al., 2019b). According to the results from Penglaitan (Huang et al., 2019b), two Hg/TOC anomalies occurred around the GLB, with one minor peak near the top of *Jinogondolella granti* Zone (Bed 6b) and a major increase across the GLB with its peak located in the *Clarkina postbitteri postbitteri-C. dukouensis* zones (Fig. 4). If the Hg/TOC values can faithfully indicate the intensity of Emeishan LIP volcanism, this could further constrain the onset of major volcanic pulse at ~260 Ma, and the acme of Emeishan LIP volcanism in the earliest Lopingian, which is different from previous views (Sun et al., 2010; Zhong et al., 2014). Confirmation of the Penglaitan Hg/TOC pattern in other sections, high-precision geochronological dating on the Emeishan LIP volcanism, and correlating the Emeishan LIP history with chronostratigraphic framework around the GLB, are needed to examine this new timeline (Huang et al., 2019b).

4.3. Latest Permian-Early Triassic

4.3.1. Carbon isotopes

Carbon isotope analyses ($\delta^{13}\text{C}_{\text{carb}}$, $\delta^{13}\text{C}_{\text{org}}$, and TOC) have become common practices in geochemical studies around the PTB, especially after a prominent negative carbon isotope excursion (NCIE) was recognized in the Gartnerkofel core (GK-1) from the Carnic Alps of Austria (Holser et al., 1989), and later found in a plethora of marine and non-marine sediments from many localities worldwide (Baud et al., 1989; Korte and Kozur, 2010; Shen et al., 2013; Zhang et al., 2016; Cui et al., 2017). For the Meishan GSSP section, since the first report of carbon isotope data by Chen et al. (1984), several updates have been presented in the past, most of which can be found in the compilation of Korte and Kozur (2010) and Schobben et al. (2017). The high-resolution dataset covering the timespan of the Siberian Traps magmatism (Fig. 5b) is a compilation from the Meishan outcrop and core data, which have been partially presented in Cao et al. (2002, 2009), Shen et al. (2013), Burgess et al. (2014), and Chen et al. (2016b). To have a better understanding on how the carbonate carbon isotopes ($\delta^{13}\text{C}_{\text{carb}}$) changed with time, we convert the stratigraphic depth of each data point into absolute age, using the high-precision zircon U—Pb ages (Shen et al., 2011a; Burgess et al., 2014) and assuming constant sediment accumulation rates between two dated ash beds (Burgess et al., 2014; Chen et al., 2016b). For the interval that are not bracketed by two ash beds, we assume its sediment accumulation rate is the same as the one from interval between the two stratigraphically closest ash beds.

As shown in Fig. 5b, seven intervals can be subdivided for the 1-Myr span (252.3–251.3 Ma) of $\delta^{13}\text{C}_{\text{carb}}$ variations. Prior to the onset of $\delta^{13}\text{C}_{\text{carb}}$ decline at 251.999 ± 0.039 Ma (Interval I), $\delta^{13}\text{C}_{\text{carb}}$ values remain stable and in the range of +3–4‰, indicating that the explosive pyroclastic eruptions and early phase of the effusive lava eruptions did not initiate dramatic feedback in the carbon cycle. The composite biodiversity patterns (Shen et al., 2011a; Wang et al., 2014) suggested that



biodiversity decline was on the way during Interval I, although most likely not catastrophic in this span of ~0.3 Myr.

The transitional Interval II, from the onset of $\delta^{13}\text{C}_{\text{carb}}$ decline at 251.999 ± 0.039 Ma to the beginning of an abrupt decrease in $\delta^{13}\text{C}_{\text{carb}}$ at 251.950 ± 0.042 Ma, is likely most critical. The $\delta^{13}\text{C}_{\text{carb}}$ values decrease from +4‰ to +2.5‰ in a duration of 49 ± 57 kyr. Sustained input and accumulation of CO_2 , whether from primary magma degassing or gas venting from negligible contact metamorphism during magma ascending (Svensen et al., 2009), probably reached a tipping point (Rothman, 2017) at 251.999 ± 0.039 Ma. Considering the analytical uncertainty (251.907 ± 0.067 Ma) and the position of the oldest dated sill sample (63.5 m above the base of the Noril'sk drill core G22) (Burgess and Bowring, 2015), the switch from dominantly extrusive eruptions to widespread sill intrusions of the Siberian Traps magmatism (Fig. 5a) likely also occurred within Interval II. As shown in a recent study (Svensen et al., 2018), widespread sill intrusions and contact metamorphism with evaporites, carbonates, and organic-rich sediments have much profound impact than the magma degassing alone. Thermal modeling suggested that the production of CO_2 during sill intrusions and contact metamorphism is typical in the 50–80 ton/m² range, and a gas production of 1000 Gt CO_2 would need an area of only 12,000–19,000 km², which is only some 0.7–1.2‰ of the known coverage of sill intrusions in the Siberian Traps (Svensen et al., 2018).

Interval III starts with a rapid drop of $\delta^{13}\text{C}_{\text{carb}}$ values from +2.5‰ to −3.3‰ in <20 kyr (Burgess et al., 2014), or 8 ± 56 kyr if we strictly apply Monte Carlo simulations for the interval from 251.950 ± 0.042 Ma (41.66 m) near the base of Bed 24e to 251.942 ± 0.037 Ma (41.90 m) at only 3 cm below the mass extinction horizon (Chen et al., 2016b). This is followed by a rebound to +0.5‰ immediately below the maximum extinction level, and oscillations between −0.7‰ and +1.5‰ until 251.572 ± 0.069 Ma, which cover almost exclusively the sill intrusion phase (Fig. 5a). Comparing with the range of +2.5–4‰ during intervals I and II, carbon cycle after the main mass extinction has switched to another state that were governed by the massive CO_2 and thermogenic methane emissions. A total duration of 427 ± 79 kyr from the onset of $\delta^{13}\text{C}_{\text{carb}}$ decline at 251.950 ± 0.042 Ma to the end of oscillations at 251.572 ± 0.069 Ma can be calculated (Burgess et al., 2014), or 378 ± 81 kyr if we choose the abrupt decrease in $\delta^{13}\text{C}_{\text{carb}}$ at 251.950 ± 0.042 Ma as a starting point.

The $\delta^{13}\text{C}_{\text{carb}}$ values remain constant around an average of −0.7‰ in Interval IV with a duration of 104 ± 106 kyr, followed by a gradual rise to ~+2‰ in the middle of Bed 39 (Interval V) that lasted for 93 ± 192 kyr. A sharp but short-lived decrease occurred in Interval VI, with a calculated duration of 15 ± 258 kyr. Above this transient change, $\delta^{13}\text{C}_{\text{carb}}$ values remain stable around +2‰ in Interval VII, until large perturbations started around the Griesbachian-Dienerian boundary (Payne et al., 2004; Zuo et al., 2006; Tong et al., 2007). It should be explained herein that because the strata above the ash bed near the top of Bed 24 are not bounded by two U–Pb ages (Fig. 5h), Monte Carlo simulations (Guex et al., 2012; Burgess et al., 2014) thus generate rather large uncertainties for the interpolated ages and durations, which should be considered with caution.

The Meishan carbon isotope record, especially the prominent change across the mass extinction horizon, is highly comparable with profiles from other marine and non-marine sections (Korte and Kozur, 2010; Shen et al., 2013; Zhang et al., 2016; Cui et al., 2017). With temporal constraints from high-resolution conodont biostratigraphy (Yuan et al., 2014) and high-precision geochronology (Burgess et al., 2014), it is a better representative to assess the link between the Siberian Traps magmatism and global carbon cycle changes recorded in sediments. As mentioned above, correlation with the timeline of the Siberian Traps magmatism strongly suggests that the abrupt change in the emplacement style from dominantly lava eruptions to sill intrusions is critical for triggering catastrophic environmental perturbations and subsequently the end-Permian mass extinction (Burgess et al., 2017; Svensen et al., 2018).

4.3.2. Oxygen isotopes

Gas emissions from large-scale LIP volcanism potentially can affect climate in many timescales (Robock, 2000; Wignall, 2001), among which SO_2 , H_2S and sulfate aerosols would cause short-term cooling, and greenhouse gases (CO_2 , CH_4) would lead to long-term warming. Therefore, high-resolution palaeotemperature profiles can help examining the potential link between LIP volcanism, environmental change, and mass extinction. Oxygen isotope palaeothermometry has been used to reconstruct temperatures in deep-time since the early work of Urey et al. (1951). Despite the inherent obstacles such as unknown of accurate oxygen isotopic compositions of ambient seawater and possibility of diagenesis during burial, this method is still widely used on prerequisites of careful selection of suitable materials, rigorous sample screening, and additional geochemical constraints (Grossman, 2012). Conodont apatite are preferred to bulk carbonates and brachiopod shells due to their resistance to diagenesis (Luz et al., 1984; Wenzel et al., 2000), as well as their spatial and temporal abundance. A number of studies have covered the Permian Period, using the conventional IRMS (isotope ratio mass spectrometry) method (Korte et al., 2004; Chen et al., 2011, 2013; Joachimski et al., 2012; Sun et al., 2012; Schobben et al., 2014) or the in situ SIMS (secondary ion mass spectrometry) method (Chen et al., 2016b; Shen et al., 2019a). The SIMS technique can perform multiple analyses on single conodont elements (Chen et al., 2016b), thus generating palaeotemperature records with higher temporal resolution that are critical for studying mass extinction events.

Oxygen isotopic compositions of conodont apatite from the Meishan, Shangsi, Daijiagou, Liangfengya (Chen et al., 2016b) and Penglaitan (Shen et al., 2019a) sections in South China, representing different environmental settings (e.g., carbonate platform, upper slope, lower slope, and ramp), demonstrated a consistent pattern of seawater temperature changes around the end-Permian mass extinction horizon. Such pattern has also been recognized at the Abadeh, Kuh-e-Ali Bashi, and Zal sections in central and northwestern Iran (Korte et al., 2004; Chen et al., 2013; Schobben et al., 2014), thus suggesting a global signal. Using the record from Meishan as an example (Fig. 5c), which has a longer temporal coverage and more precise chronostratigraphic controls from conodont biozones (Yuan et al., 2014) and zircon U–Pb ages (Burgess et al., 2014), $\delta^{18}\text{O}_{\text{apatite}}$ values fluctuate around ~21‰ for most of the Changhsingian, until a sudden decrease from 21.0‰ in Bed 25 to 18.6‰ in Bed 27a and 17.9‰ in Bed 28, which can be translated into a rapid warming of ~10 °C in 23 kyr, or a complete rising pulse of ~13 °C in 61 kyr (Burgess et al., 2014; Chen et al., 2016b). To fit with the two-pulse model, Xie (2018) used parts of the SIMS dataset from Chen et al. (2016b) and the Meishan IRMS data from Joachimski et al. (2012) to suggest two pulses of climate warming, with one prior to Bed 25 and another at the top of Bed 28. This treatment is rather a misdirection, as long-term trends (Chen et al., 2016b; Shen et al., 2019a) clearly showed that fluctuations with a magnitude of ±1‰ in $\delta^{18}\text{O}_{\text{apatite}}$ values are normal during the Changhsingian, and it seems unreasonable to regard the very last fluctuation prior to the mass extinction as climatic event associated with biotic crisis. Combining the calculated relative palaeotemperatures, carbonate carbon isotopes, and end-Permian mass extinction at Meishan with the Siberian Traps magmatism in a unified timescale (Fig. 5), it shows that the dramatic seawater temperature rise occurred only around the time of emplacement style switched from dominantly lava eruptions to widespread sill intrusions, and postdated the onset of negative shift in $\delta^{13}\text{C}_{\text{carb}}$ by ~81 kyr, the abrupt decline in $\delta^{13}\text{C}_{\text{carb}}$ by ~32 kyr, and the peak of mass extinction by ~23 kyr.

Palaeoclimatic reconstructions in terrestrial realm using direct palaeotemperature proxies are scarce, mainly due to the limitation of suitable materials and temporal resolution. Oxygen and carbon isotope compositions of vertebrate apatite ($\delta^{18}\text{O}_{\text{p}}$ and $\delta^{13}\text{C}_{\text{c}}$) from the Karoo Basin in South Africa (Rey et al., 2016, 2018) suggested constant temperatures around the end-Guadalupian mass extinction interval (Rey

et al., 2018), and an intense and fast warming of ~16 °C during the latest Permian-earliest Triassic (Rey et al., 2016). In a similar study, MacLeod et al. (2017) reported $\delta^{18}\text{O}$ values of phosphate in therapsid tusks and carbonate soil nodules from the Karoo Basin, and their results showed an increase of ~2‰ in the former and ~5‰ in the latter across the PTB, indicating warming and increased aridity during the earliest Triassic. However, correlating the PTB and mass extinction in the terrestrial sections of Karoo Basin with the well calibrated marine sections such as Meishan is in debate (Gastaldo et al., 2009, 2015, 2018; Smith and Botha-Brink, 2014; Gastaldo and Neveling, 2016; Lucas, 2018). Even when a consensus can be reached, limited temporal resolution of palaeotemperatures from terrestrial sections (Rey et al., 2016, 2018; MacLeod et al., 2017) leave large uncertainties when linking the Siberian Traps magmatism with environmental changes and mass extinction in the terrestrial realm.

Brachiopod shells are also often used for oxygen isotopic analyses (Veizer et al., 1999; Korte et al., 2005, 2008; Grossman et al., 2008; Prokoph et al., 2008; Brand et al., 2012; Mii et al., 2012, 2013; Veizer and Prokoph, 2015; Garbelli et al., 2016) and clumped isotope thermometry (Brand et al., 2012; Henkes et al., 2018). Although an overall trend can be established and compared with the record from conodont apatite, temporal resolution is a major drawback of fossil brachiopods, especially in the case of mass extinctions potentially linked with LIP magmatism. Oxygen isotopes measured on brachiopod low-Mg-calcite (bLMC) from the Dolomites, northern Italy (western Tethys) (Brand et al., 2012) and Gyanyima section, southern Tibet (Neotethys) (Garbelli et al., 2016) indicated that seawater temperatures have already increased to >35 °C prior to the mass extinction horizon, which contradicts the records measured on conodont apatite from other locations (Joachimski et al., 2012; Chen et al., 2013, 2016b; Schobben et al., 2014; Shen et al., 2019a). By measuring oxygen isotopic compositions of conodont apatite and brachiopod calcite recovered from the same stratigraphic successions, future studies hopefully can confirm whether $\delta^{18}\text{O}_{\text{apatite}}$ and $\delta^{18}\text{O}_{\text{calcite}}$ patterns are indeed different from one another, and find out the exact reasons for such puzzling discrepancy.

4.3.3. Calcium isotopes

Ocean acidification is a phenomenon fundamentally associated with the atmospheric CO₂ (Doney et al., 2009; Kump et al., 2009). Earth system modeling (Hönisch et al., 2012) suggested that the rate of CO₂ release is essential for identifying ocean acidification events. On long time scales (~10⁵ years), CaCO₃ saturation is ultimately regulated primarily by continental weathering of carbonate and silicate rocks, not atmospheric pCO₂. While weathering itself is related to atmospheric pCO₂, it is related much more weakly than ocean pH, which allows pH and CaCO₃ saturation to be almost decoupled for slowly increasing atmospheric pCO₂. As the rate of CO₂ release increases and sources (weathering) and sinks (CaCO₃ burial) are no longer balanced, progressive coupling between CaCO₃ saturation and pH occurs. Strictly speaking, “ocean acidification event” is only applied to (i) rapid (~10⁴ years and shorter) CO₂ release, (ii) ocean pH decline, and (iii) CaCO₃ saturation decline, although the latter is not always a necessity as long as the first two criteria are met (Kump et al., 2009; Hönisch et al., 2012).

Sedimentological features, such as the irregular truncation surface between the uppermost Permian skeletal limestone and the overlying microbialite in shallow-water carbonates has also been linked with submarine dissolution driven by a pulse of ocean acidification (Payne et al., 2007; Lehrmann et al., 2015; Bagherpour et al., 2017), although the precise timing and duration of this dissolution awaits further clarification (Chen et al., 2009; Payne et al., 2009). The effects of the latest Permian ocean acidification are also evident in the fossil records (Knoll et al., 2007; Clapham and Payne, 2011; Garbelli et al., 2017), as exemplified by the Rhynchonelliformea brachiopods, which are organisms with an organocarbonate multilayered shell that is vulnerable to changes in the pCO₂ and CaCO₃ saturation (Garbelli et al., 2017). The loss of columnar tertiary layer and the reduction of fiber size, as observed in the

Rhynchonellata from the Shangsi section, suggested not only ocean acidification, but also a successful strategy to cope with such disastrous change, which enabled them to survive the end-Permian mass extinction. In contrast, the Strophomenata became extinct as the pH decreased, since after the loss of their type 1 fabric, they could not further reduce their calcite structural units (Garbelli et al., 2017).

In comparison, geochemical proxies indicating ocean geochemistry changes can provide direct evidence of acidification. A negative ~0.4‰ excursion in $\delta^{44/40}\text{Ca}$, from ~−0.3‰ to −0.7‰ across the mass extinction horizon, accompanied by the well-known latest Permian NCIE of 3‰, were first recognized in bulk rock samples at the Dajiang section in the Great Bank of Guizhou, an isolated carbonate platform within the Nanpanjiang Basin (Payne et al., 2010). This pattern was also found in Turkey, Italy, and Oman in terms of the direction, magnitude, and timing of the calcium isotope excursion (Lau et al., 2017; Silva-Tamayo et al., 2018). Hinojosa et al. (2012) measured calcium isotopic compositions of conodont apatite ($\delta^{44/40}\text{Ca}_{\text{apatite}}$) from the Meishan GSSP section, and confirmed the same trend in bulk carbonates (Payne et al., 2010). In a more recent study, Silva-Tamayo et al. (2018) compiled all the available data together and argued whether the identified $\delta^{44/40}\text{Ca}$ signature is primary and global, and most importantly, its implication for the calcium and carbon cycles around the mass extinction horizon, as a response to the questions raised by Komar and Zeebe (2016). Based on updated modeling experiments, Silva-Tamayo et al. (2018) acknowledged the concerns from Komar and Zeebe (2016), and concluded that the observed parallel negative excursions in carbonate $\delta^{44/40}\text{Ca}$ and $\delta^{13}\text{C}$ is best explained by a series of consequences arising from the Siberian Traps volcanic CO₂ release, including a temporary decrease in seawater $\delta^{44/40}\text{Ca}$ due to short-lived ocean acidification and a more protracted increase in calcium isotope fractionation associated with a shift towards more primary aragonite in the sediment and, potentially, subsequently elevated carbon saturation states caused by the persistence of elevated CO₂ delivery from volcanism. More interestingly, both modeling (Komar and Zeebe, 2016; Silva-Tamayo et al., 2018) indicated that the negative shift in $\delta^{44/40}\text{Ca}$ measured on conodont apatite from the Meishan GSSP section with smaller magnitude (Fig. 5d) may be the more faithful indicator of seawater calcium cycle changes, as it is independent from fractionation factor between carbonate sediments and seawater. Nonetheless, calcium proxy as an indicator for ocean acidification prior to and during the end-Permian mass extinction still needs further clarifying.

4.3.4. Boron isotopes

The relative proportions of two aqueous boron species in seawater [i.e., B(OH)₃ and B(OH)₄[−]] are a function of pH (Hemming and Hanson, 1992; Pagani et al., 2005; Hönisch et al., 2007; Pagani and Spivack, 2007), therefore the boron isotopic compositions of marine carbonates potentially can be used to reconstruct seawater pH and identify ocean acidification events in deep-time (Lemarchand et al., 2000; Joachimski et al., 2005; Kasemann et al., 2005, 2010; Hönisch et al., 2012; Clarkson et al., 2015; Martinez-Botí et al., 2015; Gutjahr et al., 2017).

Clarkson et al. (2015) suggested that ocean acidification occurred in the Neotethys Ocean during the earliest Triassic based on boron isotope records from the United Arab Emirates (U.A.E.), and proposed a causal link with the second pulse of the Permo-Triassic mass extinction. Correlation with other sections in the Neotethys and Palaeotethys regions were based on (i) one conodont sample contained *Hindeodus parvus*, (ii) Neotethys regional stratigraphy, and (iii) carbon isotope records (Clarkson et al., 2013, 2015). Subsequently, the PTB and two pulses of mass extinction (EP1 and EP2) were decided in Wadi Bih, U.A.E., corresponding to the bases of beds 27c, 25, and 28 at the Meishan GSSP section, respectively (Clarkson et al., 2015). According to Clarkson et al. (2015), the $\delta^{11}\text{B}$ values (i.e., seawater pH) remained stable across the first pulse of mass extinction (EP1) and the period of NCIE. Such pattern was interpreted as a result of slow injection of carbon into the

atmosphere (Clarkson et al., 2015). After the $\delta^{13}\text{C}$ stabilization above the PTB, $\delta^{11}\text{B}$ began to decrease rapidly, with its minimum coincident with the second pulse of mass extinction (EP2). The suggested cause of such a rapid decrease in $\delta^{11}\text{B}$ (indicative of an abrupt ocean acidification) was a rapid and large injection of carbon, although the $\delta^{13}\text{C}$ values sustained stable at this time (Clarkson et al., 2015). The asynchronous behavior of $\delta^{13}\text{C}$ and $\delta^{11}\text{B}$ in U.A.E. remains enigmatic (Silva-Tamayo et al., 2018), as if the globally recognized NCIE at EP1 is interpreted as a response to the CO_2 transferred from a high $p\text{CO}_2$ atmosphere into the surface ocean, coherent patterns in $\delta^{13}\text{C}$ and $\delta^{11}\text{B}$ would be expected.

4.3.5. Redox proxies (Fe , Mo , U)

A large array of physical and geochemical proxies have been applied to reconstruct oceanic redox conditions around the end-Permian mass extinction, such as: sedimentary facies (Wignall and Hallam, 1992; Isozaki, 1997), pyrite framboid sizes (Wignall et al., 2005; Shen et al., 2007; Bond and Wignall, 2010; Liao et al., 2010; Li et al., 2016; Huang et al., 2017, 2019a; Xiao et al., 2018), Th/U ratios (Wignall and Twitchett, 1996), cerium anomalies (Kakuwa and Matsumoto, 2006; Loope et al., 2013; Eltom et al., 2017), sulfur isotopes (Kajiwara et al., 1994; Kaiho et al., 2006; Riccardi et al., 2006; Shen et al., 2011c; Zhang et al., 2015, 2017; Saitoh et al., 2017), biomarkers (Grice et al., 2005a, 2005b; Xie et al., 2005; Cao et al., 2009), iron speciation (Grice et al., 2005a; Clarkson et al., 2016; Shen et al., 2016; Xiang et al., 2016; Lei et al., 2017), uranium isotopes (Brennecke et al., 2011; Lau et al., 2016; Elrick et al., 2017; Zhang et al., 2018a, 2018b), and molybdenum isotopes (Proemse et al., 2013; Chen et al., 2019). However, the results of a single proxy at different sections or multiple proxies at a single location did not always agree with one another, implying strong spatial and temporal variability of redox patterns, and/or some proxies may not be as effective as claimed.

Iron speciation proxies, including $\text{Fe}_{\text{HR}}/\text{Fe}_{\text{T}}$ (the ratio of highly reactive iron to total iron) and $\text{Fe}_{\text{py}}/\text{Fe}_{\text{HR}}$ (the proportion of the highly reactive iron pool that is in the form of pyrite), have been employed at the Shangsi (Xiang et al., 2016), Daxiakou (Shen et al., 2016), and Ganxi (Lei et al., 2017) sections in the northern marginal basin of the Yangtze Platform (Yin et al., 2014), and a shelf-to-basin transect in the Arabian Margin of the Neotethys Ocean (Clarkson et al., 2016). These results suggested that at any given location, the development of redox conditions is periodic (Clarkson et al., 2016; Shen et al., 2016; Xiang et al., 2016; Lei et al., 2017). In a regional palaeogeographic framework, the timing of transitions between oxic, anoxic, euxinic, and ferruginous conditions are different from section to section (Clarkson et al., 2016; Lei et al., 2017). Therefore, it is difficult to assess whether anoxia has caused the end-Permian mass extinction from a global perspective. For instance, at the Shangsi section, iron speciation proxies indicated predominantly oxic, rather than euxinic conditions immediately below and during the mass extinction (Clarkina yini-C. meishanensis-Hindeodus changxingensis zones), thus suggesting that impinging sulfidic water should not be regarded as the proximal trigger for the extinction (Xiang et al., 2016).

Proemse et al. (2013) studied molybdenum isotopes ($\delta^{98/95}\text{Mo}$) from the Sverdrup Basin in Canadian Arctic, which was located in the northwestern margin of Pangaea during the Permian-Triassic. By comparing two sections representing different water depth, their results showed that in deep-water slope settings (Buchanan Lake section), a large shift in $\delta^{98/95}\text{Mo}$ values from $-2.02\text{\textperthousand}$ to $+2.23\text{\textperthousand}$ occurred below the mass extinction level, consistent with euxinic conditions. In sub-storm wave base shelf environments (West Blind Fiord section), only little change were shown in the $\delta^{98/95}\text{Mo}$ values ($-1.34\text{\textperthousand}$ to $+0.05\text{\textperthousand}$), suggesting oxic conditions across the EPME. This sharp contrast implicated that, widespread oceanic anoxic to euxinic conditions from deep to shallow-water environments is probably an overstatement.

Because of the long residence time (~500 kyr) of uranium (U) in the ocean, seawater U is well-mixed and exhibits globally uniform U

concentrations and isotopic compositions in seawater. Microbially mediated reduction of U(VI) to U(IV) under anoxic conditions at the sediment-water interface results in a substantial decrease in uranium solubility and a measurable change in $^{238}\text{U}/^{235}\text{U}$. Because ^{238}U is preferentially reduced and immobilized relative to ^{235}U , the $\delta^{238}\text{U}$ value of seawater U(VI) decreases as the areal extent of bottom water anoxia increases. Consequently, a global increase in the extent of anoxic bottom waters will cause simultaneous decrease in U concentrations and $\delta^{238}\text{U}$ of carbonate sediments (Brennecke et al., 2011; Lau et al., 2016). In short, seawater is expected to have lower $\delta^{238}\text{U}$ values at times of expanded oceanic anoxia and higher $\delta^{238}\text{U}$ values at times of enhanced oceanic oxygenation. To date, there are five published studies have investigated redox condition changes during the Permian-Triassic using the $\delta^{238}\text{U}$ proxy (Brennecke et al., 2011; Lau et al., 2016; Elrick et al., 2017; Zhang et al., 2018a, 2018b), including the Dawen, Dajiang, Guandao sections in the Great Bank of Guizhou (Brennecke et al., 2011; Lau et al., 2016), Daxiakou section in the northern marginal basin of the Yangtze Platform (Elrick et al., 2017), Taskent section in Turkey (Lau et al., 2016) and Zal section in Iran (Zhang et al., 2018b) on the western margin of the Palaeotethys Ocean, and Kamura section in Japan that was deposited in the open Panthalassan Ocean (Zhang et al., 2018a). These seven palaeogeographically widely separated sections exhibit a similar negative shift in $\delta^{238}\text{U}$ across the mass extinction horizon, supporting bulk carbonate $\delta^{238}\text{U}$ as a useful proxy for investigating redox changes at a global scale, as opposed to most commonly used proxies providing local redox information. However, until a robust chronostratigraphic correlation is conducted using tools such as conodont zones, $\delta^{13}\text{C}$ records, and U—Pb dating, to put the observed $\delta^{238}\text{U}$ signals in a refined temporal framework (Fig. 5), whether oceanic anoxia caused the end-Permian mass extinction from a global perspective remains arguable.

4.3.6. Hg, Zn, and Ni anomalies

In recent years, anomalies in the concentration and isotopic compositions of metallic elements (e.g., Hg, Zn, and Ni) recognized in sedimentary records were developed as new tools in understanding the relationship between LIP volcanism and mass extinctions (Rothman et al., 2014; Bergquist, 2017; Liu et al., 2017c; Rampino et al., 2017; Thibodeau and Bergquist, 2017; Percival et al., 2018) and have attracted remarkable attentions.

To our knowledge, there are at least seven published papers regarding the Hg proxy in the Permian (Sanei et al., 2012; Grasby et al., 2013, 2016, 2017; Wang et al., 2018c; Huang et al., 2019b; Kwon et al., 2019). Across the end-Permian mass extinction level, mercury proxy data (Hg concentration and Hg isotopes) have been reported from the Buchanan Lake and Smith Creek sections in Canadian Arctic (Sanei et al., 2012; Grasby et al., 2013, 2017), Festningen section in Spitsbergen (Grasby et al., 2016), Meishan GSSP section (Grasby et al., 2017; Wang et al., 2018c), and Daxiakou and Shangsi sections in South China (Wang et al., 2018c).

Although an enrichment in sedimentary mercury (Hg/TOC) is observed around the mass extinction horizon at each of those studied PTB sections (Sanei et al., 2012; Grasby et al., 2013, 2016, 2017; Wang et al., 2018c), of particular importance are the precise timing and duration of the elevated Hg concentrations, and how they correlate with the now precisely dated Siberian Traps magmatism (Burgess and Bowring, 2015) and end-Permian mass extinction (Burgess et al., 2014; Shen et al., 2019a), as well as with other palaeoenvironmental proxies that are also potentially linked with the Siberian Traps magmatism (Fig. 5).

According to data from the Meishan GSSP section (Grasby et al., 2017; Wang et al., 2018c), the mercury spike only appeared at the very top of Bed 24 (0.8 cm below the EPME horizon) and slightly dropped in the lower half of Bed 25 (Fig. 6a). Relative higher values (~200 ppb/wt.%) occurred near the onset of $\delta^{13}\text{C}_{\text{carb}}$ decline and during the sill intrusion phase of the Siberian Traps magmatism (Fig. 5a), and the rest are all below 100 ppb/wt.%. Using Monte Carlo simulations,

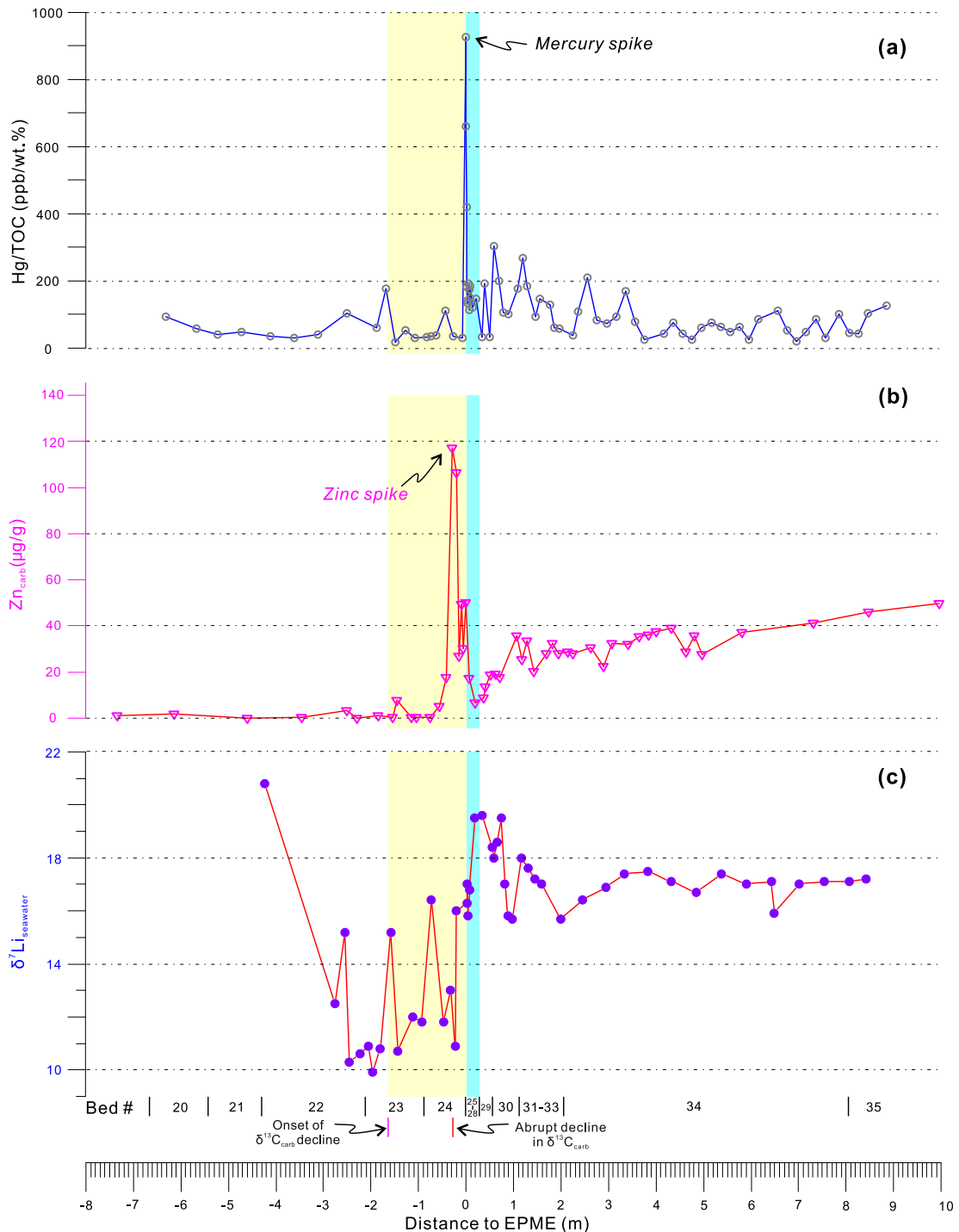


Fig. 6. (a) Hg concentration changes at the Meishan GSSP section, based on data from Wang et al. (2018c); (b) Zn concentration changes at the Meishan GSSP section, based on data from Liu et al. (2017c); (c) Reconstructed $\delta^7\text{Li}_{\text{seawater}}$ from the Meishan GSSP section, based on data from Sun et al. (2018). Bed numbers and distances to the end-Permian mass extinction (EPME) horizon (0 m) are shown at the bottom; the light-yellow and ice-blue bands represent the negative carbon isotopic shift and maximum mass extinction interval, respectively. The zinc spike occurred slightly earlier, at ~30 cm below the EPME horizon and coeval with the abrupt shift in $\delta^{13}\text{C}_{\text{carb}}$; the mercury spike appeared later, at the very top of Bed 24 (0.8 cm below the EPME horizon) and near contemporaneous with the $\delta^{13}\text{C}_{\text{carb}}$ minimum; the change in $\delta^7\text{Li}_{\text{seawater}}$ started prior to and persisted up to the mass extinction interval.

the mercury spike can be calculated at 251.941 ± 0.037 Ma, which is 58 ± 54 kyr younger than the onset of $\delta^{13}\text{C}_{\text{carb}}$ decline at 251.999 ± 0.039 Ma, and 9 ± 56 kyr younger than the abrupt shift in $\delta^{13}\text{C}_{\text{carb}}$ at 251.950 ± 0.042 Ma. During most of the negative shift of $\delta^{13}\text{C}_{\text{carb}}$ (Interval II, Fig. 5b), Hg concentrations remain close to the baseline (<100 ppb/wt.‰).

Isotopic compositions of mercury, including mass-dependent fractionation (MDF, denoted by $\delta^{202}\text{Hg}$) and mass-independent fractionation

(MIF, denoted by $\Delta^{199}\text{Hg}$), can be used to determine the sources and pathways of Hg anomalies because the two different pathways, terrestrial runoffs and atmospheric Hg^{2+} deposition, have very different isotopic signatures (Bergquist and Blum, 2007, 2009; Blum et al., 2014; Yin et al., 2015; Thibodeau and Bergquist, 2017). Essentially, marine sediments which receive Hg through terrestrial runoffs tend to have more negative $\Delta^{199}\text{Hg}$ and $\delta^{202}\text{Hg}$ values compared with oceanic sediments dominated by atmospheric Hg^{2+} deposition, which have positive

$\Delta^{199}\text{Hg}$ and less negative $\delta^{202}\text{Hg}$ values (Thibodeau and Bergquist, 2017). Comparisons of $\Delta^{199}\text{Hg}$ and $\delta^{202}\text{Hg}$ data between the Meishan section, South China (nearshore upper slope setting) and Buchanan Lake section, Canadian Arctic (bathyal to near-abyssal environment) (Grasby et al., 2017), and among the Meishan, Shangsi, and Daxiakou sections in South China (the latter two are both deposited in lower slope to deep basin environment, and the Daxiakou section is inferred to be deeper than the Shangsi section) (Wang et al., 2018c) confirmed such pattern. Available data so far (Sanei et al., 2012; Grasby et al., 2013, 2016, 2017; Wang et al., 2018c) indicated that Hg loading to the marine environments around the PTB appears to have been global in extent. However, in different sedimentary settings, the sources of Hg can vary from primarily direct atmospheric Hg^{2+} deposition in deep-water environment, to additional inputs from terrestrial runoff due to massive biomass burning and soil erosion in nearshore shallower environment (Grasby et al., 2017; Wang et al., 2018c).

Zinc concentrations and isotopic compositions of bulk carbonates from Meishan (Liu et al., 2017c) showed abrupt changes that are largely comparable with the negative shift of $\delta^{13}\text{C}_{\text{carb}}$ prior to the mass extinction in terms of timing and duration (Fig. 5). Zinc concentrations abruptly increase from $<10 \mu\text{g/g}$ to $\sim 120 \mu\text{g/g}$ at $\sim 30 \text{ cm}$ below the EMPE horizon (Fig. 6b), which is slightly earlier than the mercury spike. Using Monte Carlo simulations, the zinc spike can be calculated at $251.952 \pm 0.035 \text{ Ma}$, which is $47 \pm 52 \text{ kyr}$ younger than the onset of $\delta^{13}\text{C}_{\text{carb}}$ decline at $251.999 \pm 0.039 \text{ Ma}$, coeval with the abrupt shift in $\delta^{13}\text{C}_{\text{carb}}$ at $251.950 \pm 0.042 \text{ Ma}$, and $11 \pm 51 \text{ kyr}$ prior to the mass extinction at $251.941 \pm 0.037 \text{ Ma}$. The rapid negative shift in $\delta^{66}\text{Zn}$ from 0.84% down to 0.34% occurred at $\sim 64 \text{ cm}$ below the EPME horizon, which can be calculated as $251.965 \pm 0.033 \text{ Ma}$, and is $34 \pm 51 \text{ kyr}$ younger than the onset of $\delta^{13}\text{C}_{\text{carb}}$ decline, but $15 \pm 53 \text{ kyr}$ earlier than the abrupt shift in $\delta^{13}\text{C}_{\text{carb}}$, $13 \pm 48 \text{ kyr}$ earlier than the zinc spike, and $24 \pm 49 \text{ kyr}$ prior to the mass extinction. This abrupt decrease in $\delta^{66}\text{Zn}$ values was suggested as clear evidence for the increase of isotopically light Zn input from volcanic ashes, hydrothermal fluids, and/or extremely fast weathering of fresh volcanic rocks (Liu et al., 2017c). Correlated with the history of the Siberian Traps magmatism, the Zn and Hg concentration changes at the precisely calibrated Meishan GSSP section, either scaled against absolute age (Fig. 5e, f) or stratigraphic depth (Fig. 6a, b), indicated that the switch from dominantly extrusive eruptions to widespread sill intrusions is likely the most significant phase of the Siberian Traps eruptions and could potentially be the last straw.

Combining published data from Meishan (Kaiho et al., 2001; Rothman et al., 2014) and Shangsi (Xiang et al., 2016) in South China, southern Israel (Sandler et al., 2006), western Slovenia (Dolenec et al., 2001), Spitzbergen (Grasby et al., 2015), Gartnerkoefel GK-1 core from the Carnic Alps (Attrep et al., 1991), with their own data from Hungary, Japan, and Spiti, India, Rampino et al. (2017) recently suggested that the nickel anomalies at the end of the Permian was also a worldwide phenomenon, and proposed that the source of the nickel anomalies at the PTB were Ni-rich volatiles released by the Siberian Traps volcanism, and by coeval Ni-rich magma intrusions. At the Meishan GSSP section, both Kaiho et al. (2001) and Rothman et al. (2014) confirmed that the nickel enrichment occurred at $<10 \text{ cm}$ below the mass extinction horizon, slightly earlier than the mercury spike but highly comparable in terms of the overall patterns for both nickel and mercury concentration changes.

Using 2D micro-X-ray fluorescence imaging and 3D micro-X-ray computed tomography on Noril'sk nickel sulfide, combined with simple thermodynamic modeling, Le Vaillant et al. (2017) proposed a mechanism on how nickel, normally retained at depth in magmatic minerals, could have been mobilized and dispersed globally. According to their model (Le Vaillant et al., 2017), (i) Extensive contamination of the magma by assimilation of volatile-rich evaporites allowed the production of extremely large amounts of sulfide melt, which scavenges Ni from the magma. (ii) A proportion of this Ni present in the sulfide

melt was then transferred into the magmatic vapor phase through close physical interaction between sulfide melt and vapor bubbles. This interaction, which occurred within the subvolcanic intrusions that host the orebodies, was made possible by their shallow depth. Finally, (iii) eruption of volatile-enriched lavas released the Ni-enriched volcanic gas, producing Ni-enriched aerosols, in a form that allows it to be transported long distances, as observed in sedimentary records (Rampino et al., 2017). This flotation mechanism (Mungall et al., 2015; Le Vaillant et al., 2017) may also be effective for other metals such as copper and platinum.

4.3.7. Terrestrial impacts and weathering proxies

In terrestrial realm, massive degassing of CO_2 , SO_2 , H_2S , HCl , HF , and sulfate aerosols from LIP magmatism could also affect the environment in many ways. Using gas flux data (Svensen et al., 2009; Aarnes et al., 2011; Black et al., 2012) and geochronology of the Siberian Traps (Kamo et al., 2003), Black et al. (2014b) carried out three-dimensional global climate modeling of atmospheric chemistry during the Siberian Traps volcanism. Their simulations suggested that both CO_2 and SO_2 released from the Siberian Traps could have caused acid rain globally, although pH rebounds quickly (within 1 year) after eruptions cease. Methane (CH_4) and methyl chloride (CH_3Cl) emissions can produce steady-state ozone depletion of 60–70% globally, and recovery typically takes ~ 10 years after the cessation of emissions. Since the Siberian Traps magmatism was likely episodic (Pavlov et al., 2011), pulses of acidic rain and ozone depletion may have occurred throughout the Siberian Traps magmatism. Mutagenesis of pollen from herbaceous lycopsids and gymnosperm flora were suggested as fossil evidence of acid rain and ozone layer destruction (Visscher et al., 2004; Foster and Afonin, 2005; Hochuli et al., 2017; Benca et al., 2018).

Direct geochemical proxies indicating terrestrial acidification are arguable. A working hypothesis was proposed by Sephton et al. (2015), suggesting that analysis of variations in relative proportions of vanillin and vanillic acid extracted from soil organic matter may offer the possibility to detect major changes in soil acidity. According to their study, ratios of vanillic acid to vanillin [acid to aldehyde ratio, $(\text{Ad}/\text{Al})_v$] in organic matter assemblage from marls around the PTB at the Vigo Meano section in Southern Alps, Italy were regarded as proxy evidence for pulses of soil acidification ($\text{pH} < 4$) across the mass extinction interval (Sephton et al., 2015).

In addition to acid rain and ozone destruction, wildfires are also widely considered as a killer on land. An elevated abundance of black carbon particles, including charcoal, cenosphere and soot, found in the marine Meishan GSSP section (Xie et al., 2007; Shen et al., 2008, 2011b), along with increased PAH (polynuclear aromatic hydrocarbons) concentrations (Shen et al., 2011b), were regarded as direct evidence of wildfires. More interestingly, the elevation in black carbon contents and PAH concentrations (Shen et al., 2011b) occurred above the mass extinction horizon, and was near synchronous with the rapid warming (Chen et al., 2016b). Wildfire-derived charcoals and PAHs were also preserved in the terrestrial and transitional sections in Guizhou and Yunnan (Shen et al., 2011a; Zhang et al., 2016) and marine sections in Guangxi (Shen et al., 2011a). Correlation with the Meishan GSSP section on the basis of carbon isotopic chemostratigraphy and U—Pb geochronology suggested that wildfires were frequent in the upper part of the Kayitou Formation in terrestrial sections, above the abrupt decline in $\delta^{13}\text{C}_{\text{org}}$ and mass extinction horizon (Shen et al., 2011a; Zhang et al., 2016). Although direct, high-resolution palaeotemperature records from terrestrial sections are currently unavailable, at least not comparable with the marine profiles (Joachimski et al., 2012; Schobben et al., 2014; Chen et al., 2016b; Shen et al., 2019a), it is reasonable to suspect that rapid warming on land also occurred above the mass extinction horizon but still within the maximum extinction interval, if the wildfire-derived charcoals and PAHs can be regarded as faithful indicators of substantial rise in temperatures. This further supports the suggestion that climate warming was most likely

not a primary cause for the end-Permian mass extinction, but rather a later participant or a catalyst that increased the pace of biodiversity decline (Chen et al., 2016b). It is worth pointing out that, although in the low-latitude region such as South China where the terrestrial and marine end-Permian mass extinctions were likely synchronous (Shen et al., 2011a; Zhang et al., 2016), a recent study by Fielding et al. (2019) showed a rather different story in the Sydney Basin, Australia of the southern high-latitude area. Based on palynology coupled with high-precision CA-ID-TIMS dating and geochemical analyses such as $\delta^{13}\text{C}_{\text{org}}$ and element concentrations, their results (Fielding et al., 2019) suggested that the terrestrial extinction interval in the Sydney Basin, represented by a collapse of the *Glossopteris* flora, cessation of coal-forming conditions, and enhanced levels of phytoplankton and AOM (amorphous organic matter), occurred ~370 kyr prior to the onset of the marine extinction interval as represented by at the Meishan GSSP section.

Continental weathering, on the other hand, plays a pivotal role in closely linking the atmosphere, crust, and ocean systems, more prominently during LIPs volcanism. The Siberian Traps eruptions are suspected to have produced enormous volume of basalts and pyroclastic materials onto the continent, released massive amount of CO₂ and SO₂ into the atmosphere, caused acid rain and global warming, led to wildfires, soil erosion, and ultimately led to terrestrial ecosystem destruction, enhanced continental weathering, increased runoff delivering excessive nutrients to ocean system, increased marine productivity, oceanic anoxia, and marine mass extinction. However, silicate and carbonate weathering consumes atmospheric CO₂, therefore also works in an opposite direction. Essentially, there is a tug of war between volcanic and metamorphic degassing and silicate and carbonate weathering, and the outcome primarily controls climate and fate of ecosystems (Walker et al., 1981; Berner, 1991; Kump et al., 2000; Dessert et al., 2003; Saltzman, 2017; Johansson et al., 2018).

Weathering intensity changes, preferably constrained with high-resolution temporal controls, can be useful in assessing the link between LIP volcanism and mass extinction. Bulk and clay mineralogy, major elemental oxide abundances and CIA (chemical index of alteration) values are the commonly used tools in terrestrial sections to evaluate weathering and climatic changes, such as in the cases of PTB intervals in the Karoo Basin (Gastaldo et al., 2014), SW China (Xu et al., 2017b), North China (Cao et al., 2019), and Sydney Basin, Australia (Fielding et al., 2019). In marine settings, in addition to mineralogical and elemental indicators (Chen et al., 2015; Zhao and Zheng, 2015; Hong et al., 2017; Xu et al., 2017a), a large number of isotopic proxies (e.g., Sr, Nd, Os, Li) are also available. At the Meishan GSSP section, CIA proxy (Chen et al., 2015), carbonate-based $^{87}\text{Sr}/^{86}\text{Sr}$ (Cao et al., 2009), and conodont-based $^{87}\text{Sr}/^{86}\text{Sr}$ (Song et al., 2015; Dudas et al., 2017) have been applied.

In a recent study, Sun et al. (2018) used lithium isotopes to track weathering intensity changes around the PTB at the Meishan section. Coupled with major and trace elements data, the composite profiles of lithium concentrations and isotopic compositions from carbonates and claystones showed prominent changes around the mass extinction horizon (Sun et al., 2018). As the residence time of Li in seawater (~1.2 Myr) is much longer than the oceanic mixing time (~1000 years), Li in seawater is well-mixed vertically as well as laterally homogeneous in both elemental concentrations and isotopic compositions, therefore marine carbonates provide an archive for contemporary Li isotopic compositions of seawater (Chan and Edmond, 1988; Tomascak, 2004; Chan et al., 2006; Tomascak et al., 2016; Penniston-Dorland et al., 2017). Li isotopes are excellent tracers of silicate weathering (dominant in LIP events) with an advantage over other isotopic systems that are also sensitive to carbonate weathering (e.g., Sr) and biological activity (e.g., Os) (Penniston-Dorland et al., 2017). As lithium isotopic fractionation between seawater and marine sediments is relatively constant ($\Delta_{\text{SW-biogenic carbonate}} \sim 3\text{--}5\%$; $\Delta_{\text{SW-clay}} \sim 16\text{--}19\%$), after evaluating the relative proportions of carbonates and clays in different rock types

(e.g., chert limestone, claystone, argillaceous mudstone, and carbonaceous mudstone) at Meishan, the contemporary isotopic compositions of lithium in seawater ($\delta^7\text{Li}_{\text{seawater}}$) can be calculated based on the measured $\delta^7\text{Li}$ from sedimentary rocks (Sun et al., 2018). The results (Figs. 5g, 6c) showed that the $\delta^7\text{Li}_{\text{seawater}}$ values elevated at 251.948 ± 0.036 Ma (i.e., ~20 cm below the EPME), which is 9 ± 51 kyr before the mass extinction horizon and near synchronous with the abrupt shift in $\delta^{13}\text{C}_{\text{carb}}$. Correlation with the history of the Siberian Traps magmatism (Fig. 5a) indicated that, the enormous volume of fresh basalts that were available after the cessation of lava eruptions, combined with massive release of CO₂ and substantial rise in global temperatures during the sill intrusion phase, most likely have provided perfect conditions for enhanced silicate weathering on land.

5. Permian LIPs as potential causes of environmental/biodiversity changes

Large-scale volcanic eruptions were frequent during the Permian Period, characterized by the emplacement of at least four LIPs (Fig. 7), including the Early Permian (Cisuralian) Tarim LIP in NW China and Panjal Traps in the Himalaya, the late Capitanian (Guadalupian) Emeishan LIP in SW China and northern Vietnam, and the latest Permian-Early Triassic Siberian Traps in Siberia, Russia. Temporal correlation between the Permian biodiversity changes and volcanism (Fig. 2) hinted that the Siberian Traps and Emeishan LIP volcanism most likely caused (or at least contributed) to the end-Permian and end-Guadalupian mass extinctions, respectively, whereas the Early Permian (Cisuralian) volcanism (e.g., Tarim, and Panjal) probably played a positive role, leading to the flourishing of ecosystems. In this section, some recent advances in the study of the four Permian LIPs (Tarim, Panjal, Emeishan, and Siberian) are briefly reviewed, with special interests on their main characteristics such as timing and tempo, spatial distribution and volume, and magma-wall rock interactions.

5.1. Tarim Large Igneous Province

Although much of the Early Permian Tarim LIP in NW China is covered by the Taklamagan desert, industrial geophysical surveys and oil exploration in recent years provided new data suggesting the extent of this intraplate magmatism may exceed 0.25–0.3 × 10⁶ km², and the entire volume of the Tarim basalts was estimated to be ~0.15 × 10⁶ km³ (Xu et al., 2014) or 0.3 × 10⁶ km³ (Usui and Tian, 2017). Precise geochronological constraint on the temporal evolution of the Tarim LIP was proven to be challenging (Li et al., 2011; Wei et al., 2014; Shangguan et al., 2016). After re-evaluating of reliable ages available in the literature, Xu et al. (2014) suggested that the Tarim LIP comprises three main magmatic episodes. Episode I was emplaced at ~300 Ma, and spatially very restricted, such as diamondiferous kimberlites in Wajilitag and probably some lamprophyre dykes from Keliyang in SW Tarim. Episode II is characterized by flood basalts, low-Nb-Ta rhyolites, and volcanic pyroclastics, and formed at 292–287 Ma with a peak activity at ~290 Ma. The spatial distribution of this magmatic pulse is very extensive, probably covering the entire Tarim LIP with typical sections located at Keping and Damusi. Episode III is marked by ultramafic-mafic-felsic intrusions, low- and high-Nb-Ta rhyolites, and some mafic and felsic dykes. This last episode was emplaced between 284 and 272 Ma, with a peak activity at ~280 Ma, and the spatial distribution appears to be confined in the Bachu Uplift, Piqiang, and along the Tarim Craton's margin towards the contact with the Tianshan orogenic belt.

5.2. Panjal Traps

The breakup of Pangaea along the southern Tethys margin of Gondwana during the Early Permian (Cisuralian) produced a > 13,000 km-long string of lenticular-shaped terranes collectively known as



Fig. 7. A Permian palaeogeographic reconstruction showing the position of four LIPs, including the Tarim LIP (~300–280 Ma), Panjal Traps (~289 Ma), Emeishan LIP (~260 Ma), and Siberian Traps (~252 Ma); subduction-related arc magmatism was common along the Palaeotethys margins during the late Permian-Early Triassic; details can be found in Stampfli and Borel (2004).

“Cimmeria”. Magmatism associated with the Cimmerian rifting were widespread, including the Panjal Trap in Kashmir, the single largest contiguous outcropping of Early Permian flood basalts, and Arbor, Nar-Tsum, Bhot Kosi, Selong volcanic groups and Qiangtang mafic dykes in the Himalaya and Lhasa terrane.

The Panjal Traps cover an area of $\sim 10,000 \text{ km}^2$ exposed primarily around the Kashmir Valley along the Pir Panjal and Zanskar mountain ranges within the state of Jammu and Kashmir and are continuous into Pakistan (Shellnutt, 2018), and the estimated original area of Panjal-related magmatism could be around $\sim 0.2 \times 10^6 \text{ km}^2$ (Ernst and Buchan, 2003). The Panjal Traps consist mostly of basalt with minor amounts of basaltic andesites, rhyolites, and dacites. The reported total thickness of the volcanic rocks ranges between $\sim 3000 \text{ m}$ in the Pir Panjal Range (western Kashmir) and $\leq 300 \text{ m}$ in the Zanskar Range (eastern Kashmir), with individual flow units within the volcanic pile typically around 30 m thick. Therefore, if only considering the volcanic sequences in the Kashmir region, the volume of the Panjal Traps is in the range of $0.003\text{--}0.03 \times 10^6 \text{ km}^3$; if using the estimated spatial distribution of Ernst and Buchan (2003) and estimating an average thickness of $\sim 500 \text{ m}$, the total volume of Panjal-related basalts in the Himalaya and Lhasa terranes could be around $\sim 0.1 \times 10^6 \text{ km}^3$. A series of U—Pb, Ar—Ar, and Rb—Sr ages have been reported from various rock types in the western Himalaya, which makes it difficult to definitively constraint the duration of the Panjal-related magmatism. At the moment, it is quite possible that the Panjal Traps erupted around $\sim 289 \text{ Ma}$ and was underway in the Early Permian (Shellnutt, 2018).

5.3. Emeishan Large Igneous Province

The Emeishan LIP represents the second major magmatic event during the Permian. Flood basalts and associated intrusions of the Emeishan LIP are widespread in SW China and northern Vietnam, with its main portion bounded by the Longmenshan thrust fault in the northwest and the Ailaoshan-Red River slip fault in the southwest. Due to complicated tectonic movements and erosions in this region, a minimum estimate of $\sim 0.25 \times 10^6 \text{ km}^2$ was suggested (Xu et al., 2001), or in excess of $0.5 \times 10^6 \text{ km}^2$ when the Jinping area (Xiao et al., 2003), and the Zongza block, Ganze-Litang belt, and Songpan-Ganze block were also included (Xiao et al., 2004a, 2004b). Subsequent investigations in the Song Da zone in northern Vietnam (Hanski et al., 2004; Wang et al., 2007; Hoa et al., 2008; Tran et al., 2015; Usuki et al., 2015), western Guangxi (Fan et al., 2004, 2008; Liu et al., 2017d), and northeastern Sichuan (Li et al., 2017) have extended the distribution up to $\sim 0.7 \times 10^6 \text{ km}^2$ (Li et al., 2017). The thickness varies considerably from over 5000 m in the west (the inner zone) to several hundred meters in the east (the outer zone), thus a conservative estimate of the entire volume of the Emeishan flood basalts is $\sim 0.3 \times 10^6 \text{ km}^3$ (Xu et al., 2001), or $\sim 0.6 \times 10^6 \text{ km}^3$ (Shellnutt, 2014).

Geochronological dating from the extrusive and intrusive rocks of the Emeishan LIP and volcanic ashes in the marine sedimentary units around the GLB using different techniques have generated a large array of ages (Fig. 8a) (Shellnutt, 2014; Zhong et al., 2014; Huang

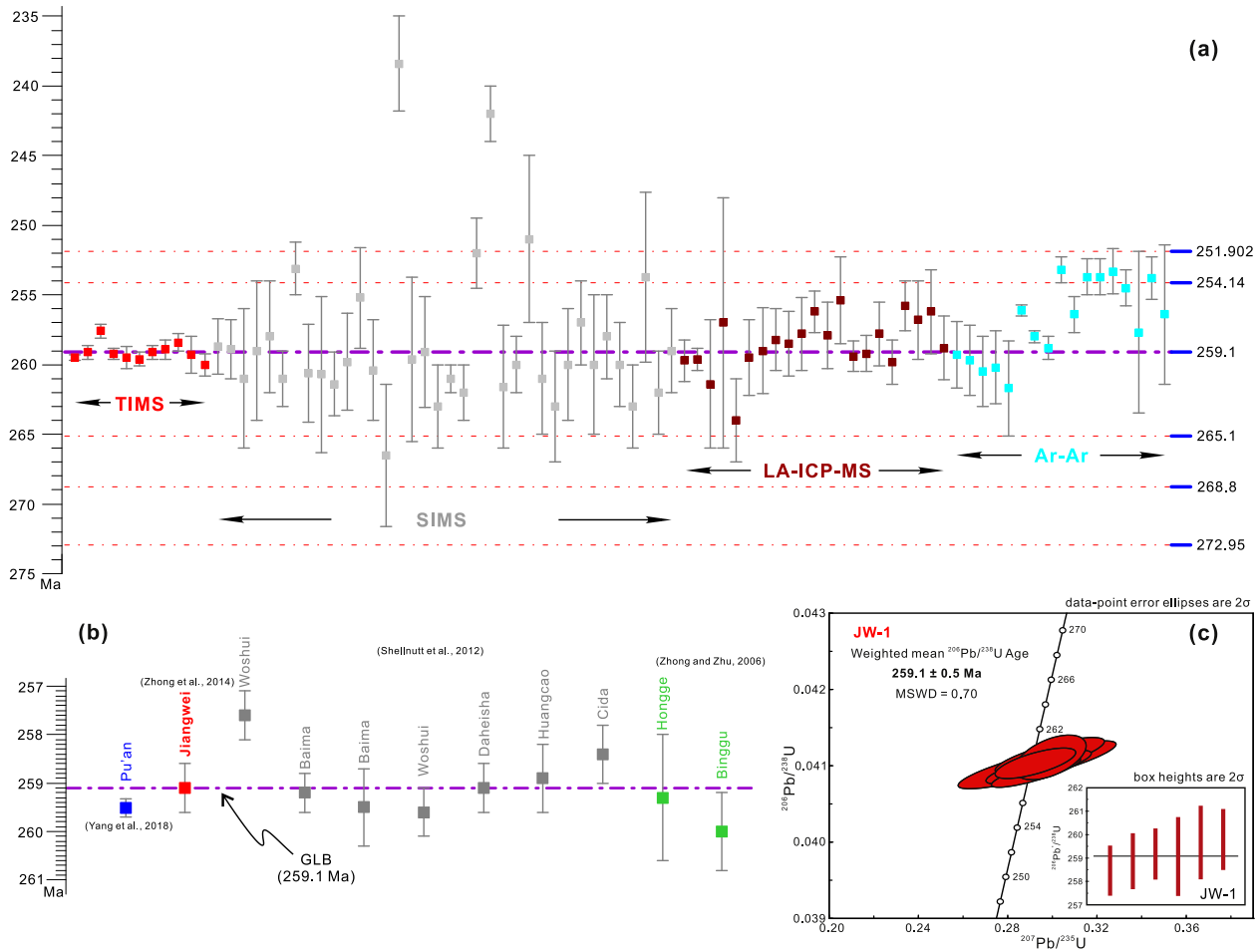


Fig. 8. (a) A compilation of published geochronological ages from the extrusive and intrusive rocks of the Emeishan LIP, updated from Shellnutt (2014), Zhong et al. (2014), Huang et al. (2018), Li et al. (2018), and Yang et al. (2018); several ages of the Permian stage boundaries (Fig. 1) are shown on the right. (b) A portion of (a), only showing the high-precision TIMS ages (Zhong and Zhu, 2006; Shellnutt et al., 2012; Zhong et al., 2014; Yang et al., 2018). (c) Concordia plot for the felsic ignimbrite sample (JW-1) from the Jiangwei section in Dali, Yunnan suggested the termination age of the Emeishan flood basalts at 259.1 ± 0.5 Ma (Zhong et al., 2014), which is also temporally used as the age of the GLB (Fig. 1).

et al., 2018; Li et al., 2018). High-precision CA-TIMS (chemical-abrasion thermal ionization mass spectrometry) dating from the Panxi region (Shellnutt et al., 2012) yielded a range of ages between >257 Ma and ~ 260 Ma. In contrast, relative ages based on conodont biostratigraphy (Sun et al., 2010) suggested that the eruption began in the *Jinogondolella altudaensis* Zone (~ 263 Ma) and greatly increased in extent and volume in the *J. xuanhanensis* Zone (~ 262 Ma), and the total duration spanned at least the *J. altudaensis-Clarkina postbitteri hongshuiensis* zones (~ 263 – 260 Ma). Based on the updated Permian timescale (Fig. 1), in which the Capitanian is constrained between 265.1 and 259.1 Ma and represented by the complete conodont succession at the Penglaitan-Tieqiao sections in Guangxi (Mei et al., 1998; Jin et al., 2006; Sun et al., 2017), the suggested earliest eruption and peak ages from Sun et al. (2010) can be recalculated around ~ 263.5 and ~ 260.9 Ma, respectively (Chen and Xu, 2017). In addition, recent high-precision CA-TIMS dating on the felsic ignimbrite near the uppermost part of the Emeishan lava succession in Dali, Yunnan (Zhong et al., 2014) yielded a weighted mean U–Pb age of 259.1 ± 0.5 Ma (Fig. 8b, c), which was interpreted as the termination age of the Emeishan flood basalts. Considering these new evidence, we hereby suggest that the main phase of the Emeishan LIP occurred between ~ 260.9 and 259.1 Ma, and the earliest eruption happened at ~ 263.5 Ma. As for the waning stage of the Emeishan volcanism, it may extended to ~ 257.8 Ma in the early Wuchiapingian (Bagherpour et al., 2018a, 2018b; Huang et al., 2018).

5.4. Siberian Traps

As the largest continental flood basalts event in the Phanerozoic, the Siberian Traps is widespread in the northwestern Siberian Craton, the Taimyr Peninsula to the north, to the west in the West Siberian Basin and further west reaching the Ural Mountains, and to the south in the Kuznetsk Basin and in the Central Asian fold belt (Reichow et al., 2009). Because a substantial portion of the Siberian Traps is covered by thick sedimentary sequences or was removed by erosion, the accurate extent and volume is difficult of estimate. A conservative “working estimate” (Reichow et al., 2009; Saunders and Reichow, 2009) suggested 5×10^6 km 2 and 3×10^6 km 3 for the size and volume, respectively, whereas Ivanov (2007) estimated these numbers could be higher as around 7×10^6 km 2 and 4×10^6 km 3 . The Siberian Traps is composed of lava, pyroclastic, and intrusive rocks, but the percentage of each component varies in different estimations (Vasil'ev et al., 2000; Ross et al., 2005; Burgess and Bowring, 2015).

Ivanov et al. (2013) compiled some of the published $^{40}\text{Ar}/^{39}\text{Ar}$ and U–Pb ages (Kamo et al., 1996, 2003; Reichow et al., 2002, 2009; Ivanov et al., 2005; Svensen et al., 2009) and suggested two pulses for the Siberian flood basalt magmatism, one around the PTB (~ 252 Ma) and another in the Middle Triassic (~ 242 Ma). Using high-precision CA-TIMS dating technique, Burgess and Bowring (2015) and Burgess et al. (2017) identified three distinct stages of magmatic activity of the Siberian Traps (Fig. 9).

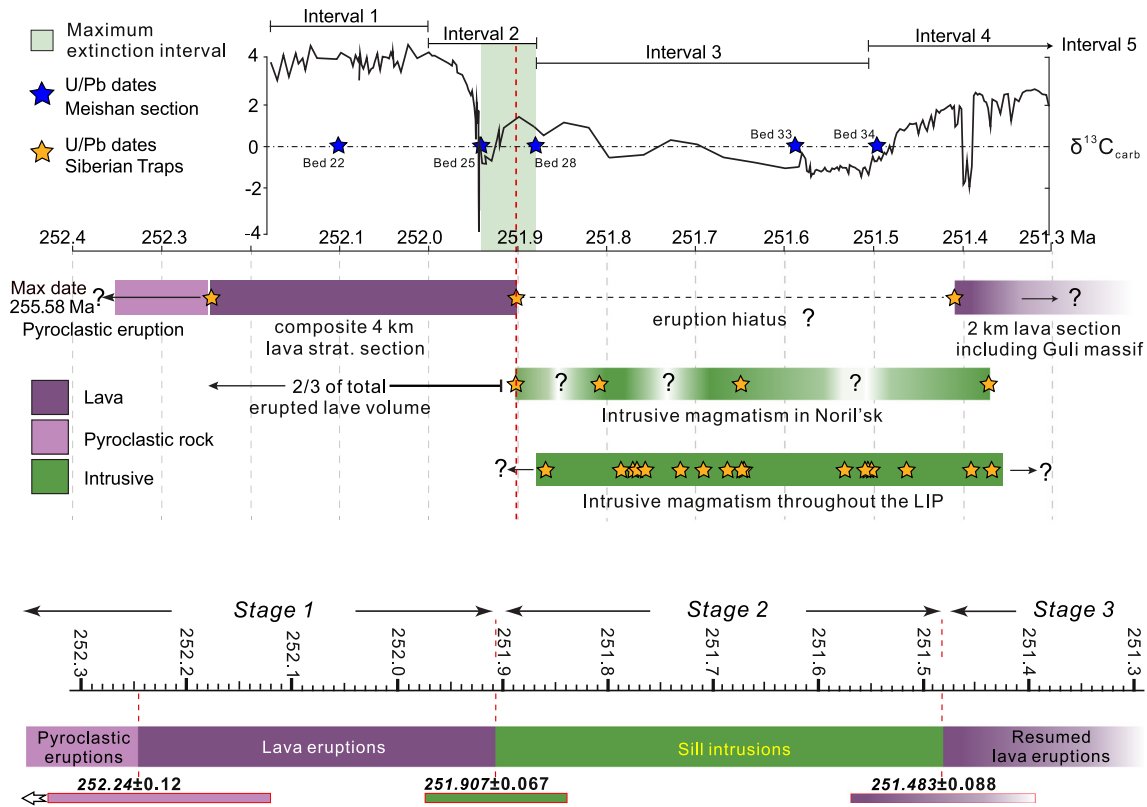


Fig. 9. A composite geochronological framework for the Siberian Traps magmatism based on a series of high-precision U–Pb ages from Siberia, correlated with the U–Pb ages, carbonate carbon isotope changes and maximum mass extinction interval at Meishan (Burgess et al., 2014; Burgess and Bowring, 2015) (above); a simplified three-stage subdivision for the evolution of the Siberian Traps magmatism (Burgess et al., 2017), with addition of the mean and uncertainty of the transitional ages (below).

Stage 1, began just prior to 252.24 ± 0.12 Ma, was characterized by initial pyroclastic eruptions followed by lava effusion. During this stage, an estimated 2/3 of the total volume of Siberian Traps lavas was emplaced ($>1 \times 10^6 \text{ km}^3$). Dating the onset of Siberian Traps magmatism is important but also challenging, since no zircon-bearing samples (except for xenocrysts) have been found within the basal Siberian Traps lava flows from the Maymecha-Kotuy or Noril'sk sections. Using ID-TIMS (isotope dilution thermal ionization mass spectrometry) dating method, Kamo et al. (2003) reported a weighted mean U–Pb age of 251.7 ± 0.4 Ma based on perovskite recovered from a melanephelinite sample collected ~200 m above the base of the Arydzhangsky Suite in the Maymecha-Kotuy area, and suggested this age as the onset of Siberian flood volcanism. Re-sampling and analyzing of perovskite crystals from the Arydzhangsky Suite yielded U–Pb ages of 252.20 ± 0.12 Ma and 252.27 ± 0.11 Ma. The mean of these two overlapping dates at 252.24 ± 0.12 Ma was suggested as the best estimate of the minimum age for the onset of Siberian Traps magmatism (Burgess and Bowring, 2015).

Stage 2, began at 251.907 ± 0.067 Ma and ended at 251.483 ± 0.088 Ma, was characterized by cessation of extrusive magmatism and onset of widespread sill intrusions. This timeline was based on a series of high-precision zircon U–Pb ages from sills throughout the Siberian Traps (Burgess and Bowring, 2015), with majority of the dates came from Noril'sk region, where the cross-cutting relationship between intrusions and lavas and/or volcaniclastic rocks are clear.

Lava eruptions resumed at 251.483 ± 0.088 Ma after a hiatus of ~420 kyr, marking the beginning of Stage 3. This age was dated from a wedged, crystal-rich, felsic tuff collected at ~160 m above the base of the Delkansky Suite in the Maymecha-Kotuy area, including the Guli volcanic-intrusive complex (Kamo et al., 2003). Both extrusive and intrusive magmatism occurred during Stage 3, which lasted until at least 251.354 ± 0.088 Ma, an age dated from the Scholokhovskoe pipe in

Nepa and likely representing the youngest sill of the Siberian Traps. The end of Stage 3 was estimated at 250.2 ± 0.3 Ma, based on baddeleyites extracted from carbonatite in the Guli complex (Kamo et al., 2003).

5.5. Examining the LIP-mass extinction association

Many LIP events occurred throughout the Phanerozoic, but only a number of them can be confidently correlated with biodiversity losses that can be ranked as major mass extinctions (Raup and Sepkoski, 1982; Bambach, 2006; Alroy et al., 2008; McGhee et al., 2013; Stanley, 2016). This raises an obvious question: What makes a LIP event deadly? Assessing the characteristics of individual LIPs, such as palaeogeographic location, age and duration, size and volume, magma source, and plume-lithosphere-crust interactions, may shed some light on the pursuit of an answer. For this reason, main characteristics of the four Permian LIPs (Tarim, Panjal, Emeishan, and Siberian) are summarized in Table 1, with special interests on features such as volcanic fluxes (i.e., eruption rates) and plume-lithosphere-crust interactions, which are critical in determining their potentials of affecting Earth's surface system.

High-precision geochronology is obviously pivotal in establishing the link between LIP volcanism and environmental and biological changes, which means that ideally the history of LIP eruptions, environmental changes recorded in the marine and terrestrial realms, and biodiversity changes should be correlated in a unified, high-precision temporal framework. The evolution of the Siberian Traps has been well constrained (Burgess and Bowring, 2015), whereas temporal constraints on the Emeishan LIP (Shellnutt et al., 2012; Zhong et al., 2014), as well as the Tarim LIP (Xu et al., 2014) and Panjal Traps (Shellnutt, 2018), are less than ideal. In stratigraphic successions, although significant progress has been made in the calibration of the

Table 1

Comparison of main characteristics of four Permian LIPs (Tarim, Panjal, Emeishan, and Siberian).

	Tarim LIP	Panjal Traps	Emeishan LIP	Siberian Traps
Present-day location	Xinjiang, NW China	Kashmir, northern Nepal, southern Tibet	SW China, northern Vietnam	Siberia, central-north Russia
Palaeogeographic location	Tarim Block; ~30°N	Northern margin of Gondwana; ~45°S	East Palaeotethys; ~10°S	Siberian Craton; ~60°N
Area (Mkm ²)	0.25–0.3	0.01–0.2	0.25–0.7	5–7
Volume (Mkm ³)	0.15–0.3	0.003–0.1	0.3–0.6	3–4
Age	Three episodes: 300–290–280 Ma	~289 Ma	Maximum duration: ~263.5–257.8 Ma; Main eruption: ~260.9–259.1 Ma	Three stages: 252.24–251.907 – 251.483 – 251.354 Ma
Duration of main pulse	>5 Myr	/	<1 Myr	~300 kyr

Permian timescale in the last decade (Ramezani and Bowring, 2018), some intervals such as the upper Cisuralian, lower Guadalupian, and Guadalupian-Lopingian boundary are yet to be precisely confined with high-precision U–Pb geochronology (Lucas and Shen, 2018b; Ramezani and Bowring, 2018; Shen et al., 2019b). Nevertheless, current available data enforced the temporal correlations between Siberian Traps and end-Permian mass extinction, and between Emeishan Traps and end-Guadalupian mass extinction.

There are many variables deciding if a LIP event has the potential to cause extreme environmental and biological changes (Bond and Wignall, 2014; Courtillot and Fluteau, 2014; Ernst, 2014; Self et al., 2014; Bond and Grasby, 2017; Ernst and Youbi, 2017), and LIPs should be comprehensively examined on a case-by-case basis. By comparison of the main characteristics of four Permian LIPs, a most striking feature of the Siberian Traps is its enormous areal distribution and volume, and short duration. According to the high-precision age model from Burgess and Bowring (2015), in which they suggested two-thirds of the total pyroclastic/lava volume of 4×10^6 km³ of the Siberian Traps was erupted in ~300 kyr, a volcanic flux (i.e., eruption rate) of 8.9 km³/yr can be calculated. The area and volume, and age and duration of other Permian LIPs are less well constrained. A rough estimate would give a flux of 0.3–0.6 km³/yr for the Emeishan LIP and 0.03–0.06 km³/yr for the Tarim LIP. Therefore, high volcanic flux is probably one of the key factors distinguishing the Siberian Traps from other Permian LIPs.

In addition to the volcanic flux, another key element deciding the killing potential of LIP eruptions is gas production. Various models on the source of volatiles released during the Siberian Traps magmatism have been put forward in the past years, accompanied with corresponding estimations (Sobolev et al., 2009, 2011; Svensen et al., 2009, 2018; Aarnes et al., 2011; Black et al., 2012, 2014a; Polozov et al., 2016; Broadley et al., 2018). Svensen et al. (2009) and follow-up studies (Aarnes et al., 2011; Polozov et al., 2016; Svensen et al., 2018) emphasized the significance of contact metamorphism when ascending magma interacted predominantly with the Cambrian evaporites and the Carboniferous-Permian coals. According to their estimation (Svensen et al., 2009), total gas production for CO₂, CH₄, CH₃Cl, and CH₃Br are in the range of 39,000–114,000, 14,300–41,900, 5200–15,300, and 87–255 Gt (Gigatonnes), respectively. Petrological and geochemical studies on olivine phenocrysts, melt and spinel inclusions from Noril'sk (Sobolev et al., 2009, 2011) suggested that the formation of magmas was significantly affected by the contamination from ancient recycled oceanic crust. Moreover, the initial magmas are significantly enriched in Cl compared with typical mantle melts, and the Cl content increases considerably during magma evolution, owing probably to interaction with evaporites (Sobolev et al., 2009). Sobolev et al. (2011) estimated that, with the involvement of recycled oceanic crust, the total volume of CO₂ and HCl gases released would be >170,000 and 18,000 Gt, respectively.

Similarly, by measuring concentrations of S, Cl, and F from melt inclusions from the Siberian Traps, Black et al. (2012) estimated that the sum of degassing from intrusive and extrusive rocks to be approximately ~6300–7800 Gt S, ~3400–8700 Gt Cl, and ~7100–13,600 Gt F.

Subsequent sulfur isotopic evidence (Black et al., 2014a) also implied crustal contamination, indicating the volatile sources from mantle and crust (e.g., evaporites, shales, and coals). More recently, Broadley et al. (2018) presented halogen (Cl, Br, and I) compositions of sub-continental lithospheric mantle xenoliths emplaced before and after the eruption of the Siberian flood basalts, and suggested that the Siberian lithosphere is massively enriched in halogens from the infiltration of subducted seawater-derived volatiles. They estimated that up to 70% of lithospheric halogens were assimilated into the plume and released to the atmosphere, and degassed Cl, Br, and I were in the range of 3500–10,400, 9.6–29.0, and 0.2–0.5 Gt, respectively (Broadley et al., 2018).

Ganino and Arndt (2009) recognized the importance of sedimentary rock types in basins beneath the flood basalts and the far greater impact of sediment-derived gases in comparison with emission of magmatic gases. Using the Panzhihua intrusion as a representative of an average sill in the Emeishan LIP, assuming the total volume of the erupted basalt in the Emeishan LIP was $\sim 1 \times 10^6$ km³ (Courtillot and Renne, 2003), and following the estimation of CO₂ release from Deccan volcanism (Self et al., 2006), Ganino and Arndt (2009) estimated that 61,600–145,600 Gt metamorphic CO₂ and 16,800 Gt magmatic CO₂ were released during the Emeishan LIP eruptions. If the total volume is only in the range of 0.3 $\times 10^6$ km³ (Xu et al., 2001) to 0.6 $\times 10^6$ km³ (Shellnutt, 2014), metamorphic and magmatic CO₂ emission would be about half of the above values. By measuring sulfur contents in olivine-hosted melt inclusions from Dali picrites, Zhang et al. (2013) calculated that 1 km³ of the Emeishan basalts can release 5 Mt of SO₂ into the atmosphere. Therefore, a total of 1500–3000 Gt SO₂ would have been released if the volume of the Emeishan LIP is in the range of 0.3 $\times 10^6$ km³ (Xu et al., 2001) to 0.6 $\times 10^6$ km³ (Shellnutt, 2014).

Estimations of gas emission from the Tarim LIP and Panjal Traps are currently not available. However, stratigraphic and sedimentological correlation across the Tarim LIP based on boreholes, outcrops, and seismic profiles (Li et al., 2014) indicated that the wall rocks beneath the Tarim flood basalts are mostly sandstone, mudstone, and siltstone units. According to Ganino and Arndt (2009), these types of sedimentary rocks are “gas-poor” and contact metamorphism under such conditions most likely has only minor environmental impact.

In summary, among the four LIPs in the Permian, the combination of high volcanic flux (Burgess and Bowring, 2015), contact metamorphism with evaporites and coals (Svensen et al., 2009), and plume-lithosphere-crust interactions (Sobolev et al., 2011; Broadley et al., 2018) for the Siberian Traps magmatism certainly made it the most deadly. With high-precision geochronological constraints on both the Siberian Traps magmatism (Burgess and Bowring, 2015) and the end-Permian mass extinction (Burgess et al., 2014; Shen et al., 2019a), variations of geochemical proxies preserved in marine and non-marine settings can be used to examine the links between LIP magmatism, environmental changes and mass extinctions with confidence. Using the best-calibrated Meishan GSSP section as an example (Fig. 5), the timeline of major changes in geochemical proxies such as $\delta^{13}\text{C}_{\text{carb}}$, $\delta^{18}\text{O}_{\text{apatite}}$, $\delta^{44/40}\text{Ca}_{\text{apatite}}$, [Zn] and $\delta^{66}\text{Zn}$, Hg/TOC, and

$\delta^7\text{Li}_{\text{seawater}}$ strongly suggests that, the switch from dominantly extrusive eruptions to widespread sill intrusions is the most significant aliquot of the total, erupted/emplaced history of the Siberian Traps (Burgess and Bowring, 2015; Burgess et al., 2017; Svensen et al., 2018), and is most likely the trigger for the end-Permian mass extinction.

At the moment, among three highly suspected kill mechanisms (i.e., climate warming, ocean acidification, and anoxia) for the end-Permian mass extinction in the marine realm (Fig. 10), ocean acidification, as indicated by evidence such as calcium isotopes in bulk carbonates (Payne et al., 2010; Lau et al., 2017; Silva-Tamayo et al., 2018) and conodont apatite (Hinojosa et al., 2012), and microstructures in brachiopod fossils (Garbelli et al., 2017), is most likely the primary cause, since those changes occurred prior to and across the mass extinction horizon. Rapid rising in seawater temperatures, as suggested by high-resolution oxygen isotopic records measured on conodont apatite from the Meishan, Shangsi, Daijiagou, Liangfengya (Chen et al., 2016b), Penglaitan (Shen et al., 2019a) sections in South China, and Abadeh, Kuh-e-Ali Bashi, and Zal sections in Iran (Korte et al., 2004; Chen et al., 2013; Schobben et al., 2014), occurred above the mass extinction horizon but within the maximum extinction interval, therefore, climate warming is probably not a primary cause, but rather a later participant or a catalyst that increased the pace of biodiversity decline (Chen et al., 2016b). Ocean anoxia is more complex, as a large array of redox proxies reported from different sedimentary environments ranging from deep ocean to shallow carbonate platform often contradict one another (Proemse et al., 2013; Xiang et al., 2016; Lei et al., 2017).

Therefore, ocean anoxia acting as a cause of the end-Permian mass extinction is probably conditional on water depth.

In terrestrial realm, various kill mechanisms such as acidic rain, ozone depletion, aridity and wildfires caused by global warming, hypoxia, and toxic metal poisoning have been proposed in the past (Fig. 10). Although mass extinction on land and in the ocean during the latest Permian-earliest Triassic were likely contemporaneous (Shen et al., 2011a; Zhang et al., 2016), given the updated high-precision geochronological constraints on the Siberian Traps magmatism (Burgess and Bowring, 2015) and end-Permian mass extinction (Burgess et al., 2014; Shen et al., 2019a), finding direct geochemical evidence with comparable temporal resolution to support these kill mechanisms in terrestrial realm remains a challenging task.

As for the Emeishan LIP, although contact metamorphism with wall rocks (e.g., limestone, dolomite, and shale) has been suggested (Ganino and Arndt, 2009), low volcanic flux of 0.3–0.6 km³/yr (this study) and medium gas emission (Ganino and Arndt, 2009; Zhang et al., 2013) probably limited its potential. Nonetheless, after collectively assessing key evidence from the late Guadalupian-early Lopingian, such as the turnover of major fossil groups, long-term and short-term sea-level changes, and variation of geochemical proxies across the GLB (e.g., $\delta^{13}\text{C}_{\text{carb}}$, $\delta^{18}\text{O}_{\text{apatite}}$, $^{87}\text{Sr}/^{86}\text{Sr}$, $\delta^{44}/^{40}\text{Ca}$, $\delta^{34}\text{S}$, and Hg/TOC), we suspect that the largest regression and Emeishan LIP volcanism are the combined triggers, and climate change (Chen et al., 2011), ocean anoxia (Zhang et al., 2015), and gaseous metal loading (Huang et al., 2019b) are primary kill mechanisms for biodiversity loss in the end-Guadalupian (Fig. 4).

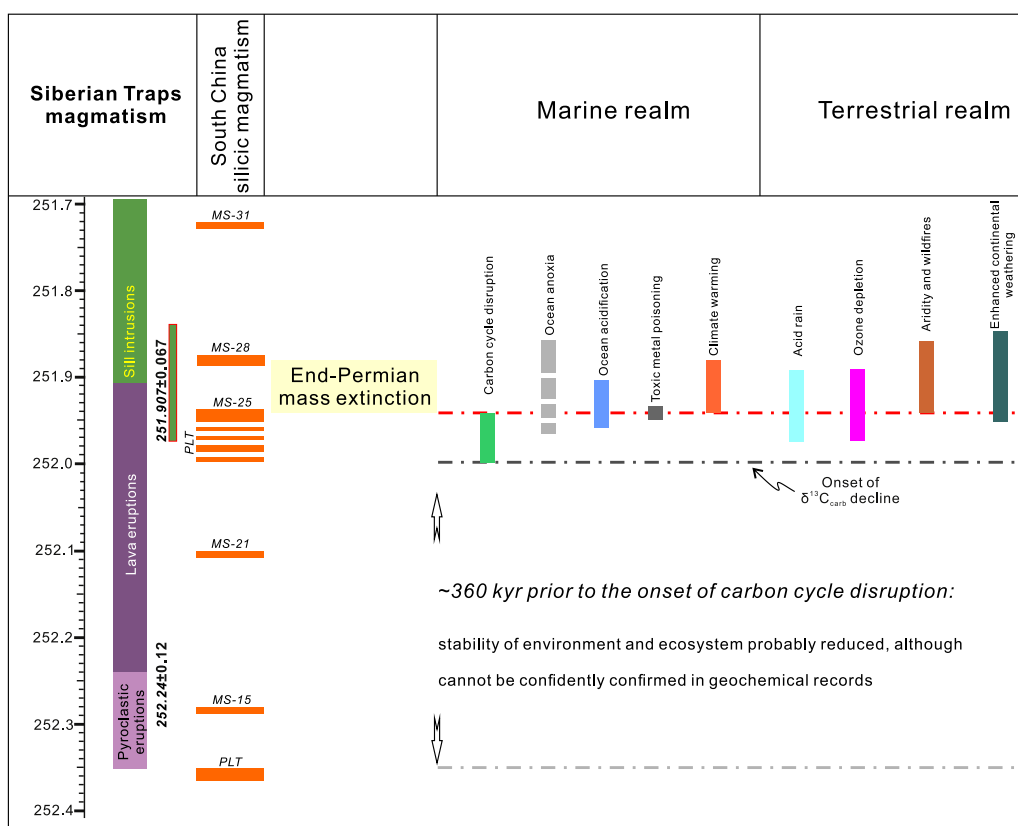


Fig. 10. A preliminary summary of major environmental changes in the marine and terrestrial realms during the latest Permian-earliest Triassic, correlated with the timeline of Siberian Traps (Burgess and Bowring, 2015) and South China silicic magmatism, implicating the sill intrusion phase of the Siberian Traps combined with intensified South China silicic volcanic eruptions as the ultimate trigger for the end-Permian mass extinction. Age-constrained volcanic ash layers and/or tuffaceous sandstones from Meishan (Shen et al., 2011a; Burgess et al., 2014) and Penglaitan (Shen et al., 2019a) are indicated (MS = Meishan; PLT = Penglaitan); light grey, dark grey, and red dash lines indicate the onset of intensified South China silicic volcanism at 252.359 ± 0.038 Ma (Shen et al., 2019a), $\delta^{13}\text{C}_{\text{carb}}$ decline at 251.999 ± 0.039 Ma (Burgess et al., 2014), and the end-Permian mass extinction at 251.941 ± 0.037 Ma (Burgess et al., 2014), respectively. Timing for various environmental changes in the terrestrial realm are not well constrained, although we suspect that acid rain and ozone depletion likely corresponded to the onset of sill intrusions as gas production (e.g., SO₂, CO₂) substantially increased; aridity, wildfires, and enhanced continental weathering closely linked with temperature change, therefore they probably occurred at the onset of rapid warming (Chen et al., 2016b) and continued during the Early Triassic hothouse condition (Sun et al., 2012).

Corresponding parameters for the Tarim LIP and Panjal Traps are not well constrained (Shellnutt, 2014, 2018). Given the long-lasting but episodic nature, volcanic flux and gas emission of the Early Permian magmatism (Tarim, Panjal, and other Cimmerian rifting-related volcanic eruptions) are most certainly low comparing with the Emeishan LIP and Siberian Traps. However, pulsating eruptions, instead of rapid emplacement for a typical LIP (<1 Myr), may have played a positive role in affecting the environment and biosphere, as evident from rising of $p\text{CO}_2$ and flourishing of ecosystems during the latest Carboniferous-Early Permian (Montañez, 2016).

6. Arc magmatism and the end-Permian mass extinction

Although the LIP volcanism is preferably considered as a principle trigger for mass extinction events, especially in the case of the end-Permian mass extinction, some weaknesses are associated with this model. One of the difficulties encountered is that the eruption of flood basalts, the dominant component of LIP, likely does not release sufficient toxic and greenhouse gases to trigger global changes. In addition, fissure style of flood basalt volcanism in many LIPs cannot ensure injection of volcanic ashes into the stratosphere, a condition required by the LIP-mass extinction model. This has led to modified version of LIP-mass extinction model invoking addition of crustal S and C in LIP-emitted gas budget (Svensen et al., 2009). Alternatively, continental arc magmatism has been recently proposed as causes of global environmental changes (He et al., 2014; Lee et al., 2015; McKenzie et al., 2016).

In the shadow of the enormous Siberian Traps flood basalt volcanism, arc magmatism during the Permian-Triassic transition and its role in the environmental and biological changes are often underestimated. The main phase of the Choiyoi silicic igneous province in the southwestern margin of Gondwana has a long duration of 30 to 40 Myr (Rocha-Campos et al., 2011; Sato et al., 2015), with its termination age at ~251.9 Ma (Rocha-Campos et al., 2011) that is contemporaneous with the Siberian Traps magmatism (Burgess and Bowring, 2015). Geochronological and provenancial studies on volcanic tuffs from the southern Gondwanan basins in South America and Africa (e.g., Parana, Karoo) indicated that those widespread ash falls may relate to the Choiyoi silicic magmatism (Rocha-Campos et al., 2011; McKay et al., 2016; Castillo et al., 2017; Viglietti et al., 2018).

In the Tethys realm, continental arc magmatism has been invoked as a trigger for the end-Permian mass extinction (Sengör and Atayman, 2009; He et al., 2014). In the extensively studied South China region, widespread volcanic ash layers have long been recognized in the sedimentary records (Yin et al., 1992). At the Meishan GSSP section (Fig. 11), the most dramatic biodiversity decline occurred at the base

of Bed 25, which is a distinct, thick volcanic ash layer that can be traced at the same stratigraphic level wide across South China. Given this temporal coincidence between the PTB volcanic ashes and mass extinction, understanding of volcanism producing these ashes in South China is therefore the key to identify the cause of mass extinction. Recent investigations on whole-rock petrology, mineralogy, major and trace elements, and zircon U-Pb ages and Hf-O isotopic compositions (Gao et al., 2013, 2015; He et al., 2014; Liao et al., 2016; Wang et al., 2018a, 2019; Zhao et al., 2019) suggested that the PTB volcanic ash layers were derived from arc magmatism along convergent continental margins around the South China Block, rather than from the Siberian Traps (He et al., 2014). For instance, zircons extracted from the PTB volcanic ashes from the Meishan, Shangsi, Chaotian, and Dongpan sections have negative $\varepsilon_{\text{Hf}}(t)$ (−12.9 to −2.0) and $\delta^{18}\text{O}$ (6.8 to 10.9‰), consistent with a crustal-derived acidic origin, most likely during the Palaeotethys arc magmatism (He et al., 2014).

Indeed, more and more studies (He et al., 2014; Wang et al., 2019; Zhao et al., 2019) started to emphasize the importance of regional arc volcanism and their contribution to the end-Permian mass extinction. If the number of volcanic ash layers and their thickness can be regarded as indicators of frequency and intensity of volcanic eruptions (He et al., 2014; Wang et al., 2019; Zhao et al., 2019), silicic magmatism is evidently more frequent and intense in the latest Permian and earliest Triassic, as shown in the condensed Shangsi section (Huang et al., 2018; Yuan et al., 2019) and highly expanded Penglaitan section (Shen et al., 2019a). However, the presence or absence of volcanic ash layers and/or tuffaceous sandstones (e.g., Penglaitan) depends on many factors, such as volcanic explosivity, atmospheric dispersal, hydrodynamic condition, and depositional environment. Moreover, arc magmatism is often not preferred as the primary cause of the end-Permian mass extinction because of its relatively long duration and low eruption rate comparing to that associated with the Siberian Traps. The amount of products from Palaeotethys arc magmatism (e.g., volcanic ash, and gas) is also likely small comparing to the massive Siberian Traps eruptions. However, modern example of arc magmatism such as Pinatubo (Hansen et al., 1992; McCormick et al., 1995) and Toba (Rampino and Self, 1992; Rampino and Ambrose, 2000) show its devastating nature and potential cause for global changes.

A possible model is that low-latitude, silicic magmatism around the South China Block and high-latitude Siberian Traps flood basalt volcanism have both contributed (Fig. 10). From at least ~420 kyr before the mass extinction, or around 252.359 ± 0.038 Ma for the South China arc magmatism (Shen et al., 2019a), prior to 252.24 ± 0.12 Ma for the pyroclastic eruptions of the Siberian Traps (Burgess and Bowring, 2015), combined effects have put the contemporaneous

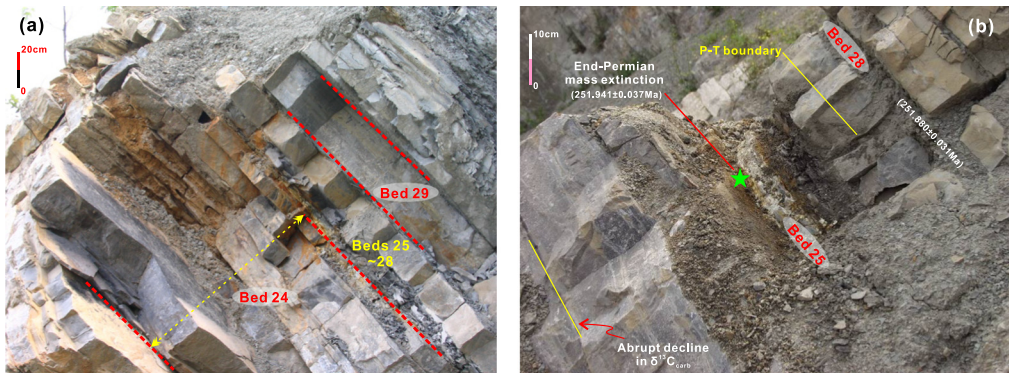


Fig. 11. Field photos showing the PTB interval at the Meishan GSSP section. (a) An overview of Beds 24–29, in which dramatic environmental and biological changes occurred (Fig. 5), except the onset of $\delta^{13}\text{C}_{\text{carb}}$ decline that happened in the middle of Bed 23, ~70 cm below the base of Bed 24 (Burgess et al., 2014). (b) A close-up view of Beds 25–28, which represents the maximum extinction interval (Shen et al., 2011a; Burgess et al., 2014); the abrupt decrease in $\delta^{13}\text{C}_{\text{carb}}$ occurred at ~30 cm below the end-Permian mass extinction horizon, which is located at the base of Bed 25, a distinct volcanic ash layer that can be traced at the same stratigraphic level wide across South China. Hf-O isotopic compositions of zircons from Beds 25 and 28 show high $\delta^{18}\text{O}$ values (6.8 to 9.1‰) and negative $\varepsilon_{\text{Hf}}(t)$ values (−12.1 to −2.7), indicating a crustal-derived acidic origin, rather than mantle origin from the Siberian Traps (He et al., 2014).

environment and ecosystem under continuous pressure; only until ~58 kyr prior to the mass extinction, marked by the onset of $\delta^{13}\text{C}_{\text{carb}}$ decline at 251.999 ± 0.039 Ma, the impact has become obvious, as shown by variation of multiple geochemical proxies in this pre-extinction short interval (Fig. 5). The most deadly blow likely happened around 251.939 ± 0.031 Ma (Shen et al., 2019a), when the Siberian Traps magmatism switched from dominantly extrusive eruptions to widespread sill intrusions (Burgess and Bowring, 2015), and the intensity of South China silicic magmatism significantly increased (He et al., 2014; Wang et al., 2019; Zhao et al., 2019), as indicated by a thick and widespread ash layer equivalent to Bed 25 at Meishan.

7. Conclusion

In perspective, the link between Permian (as well as other periods) LIPs and major environmental and biological changes rests on three pillars: comprehensive biodiversity patterns, high-precision geochronology, and robust geochemical proxies. The last decade or so have witnessed rapid progress in each field. Compilation and quantitative analyses on vast fossil data in the Paleobiology Database (PBDB; <https://paleobiodb.org/>) and Geobiodiversity Database (GBDB; <http://geobiodiversity.com/>) have enhanced our understanding of the evolutionary history of biosphere (Alroy et al., 2008; Shen et al., 2011a; Wang et al., 2014; Zaffos et al., 2017). The significant progress in single-zircon U–Pb analysis by CA-TIMS and/or ID-TIMS techniques (Ramezani et al., 2007; Shen et al., 2011a; Schmitz and Davydov, 2012; Shellnutt et al., 2012; Burgess et al., 2014; Zhong et al., 2014; Burgess and Bowring, 2015; Wu et al., 2017; Ramezani and Bowring, 2018; Shen et al., 2019a) provide refined temporal constraints on the history of Permian LIP magmatism and sedimentary successions. Accumulation of data on conventional geochemical proxies (e.g., C, O, S, N) and development of non-traditional geochemical proxies (e.g., Hg, B, Mo, U, Zn) shed light on the underlying mechanisms linking the LIP magmatism with biotic crisis. Given the rapid increase of information, the “standard model” of possible environmental and biological consequences of LIP events, as exemplified by the couplet of Siberian Traps/end-Permian mass extinction (Wignall, 2001, 2007; Algeo et al., 2011), should develop towards the direction of high-resolution, time-dependent, geo-systematic integrations. Network-based palaeoecological analyses to dissect how the biotic crisis was unfolded (Erwin, 2014; Muscente et al., 2018), and climate modeling based on comprehensive records with high-precision temporal constraints (Black et al., 2018; Penn et al., 2018), may prove enlightening for future research on the links between massive volcanism, environmental perturbations, and biological events.

Nonetheless, our survey on (i) the biodiversity changes in the Permian, especially the end-Guadalupian and end-Permian mass extinctions, (ii) variation of geochemical proxies preserved in the Permian sedimentary records, (iii) main characteristics of four Permian LIPs (e.g., Tarim, Panjal, Emeishan, and Siberian), and (iv) arc magmatism in the Tethys realm during the late Permian-Early Triassic, collectively suggests:

- (1) Whether the widespread and episodic Early Permian (Cisuralian) LIP eruptions (e.g., Tarim, and Panjal) were associated with global events is largely uncertain, as there are no obvious changes precisely corresponding to each episode of massive volcanism. However, this does not rule out the possibility that the Early Permian (Cisuralian) LIP volcanism has contributed to contemporaneous environmental and biological changes, especially the gradual climate warming and flourishing of ecosystems.
- (2) The end-Guadalupian mass extinction (i.e., pre-Lopingian crisis) was not severe as previously thought, and it only happened at the community level and was taxonomically selective. However, considering key evidence from the late Guadalupian-early Lopingian, such as the turnover of major fossil groups, long-term and short-term sea-level changes, and variation of geochemical proxies across the GLB (e.g., $\delta^{13}\text{C}_{\text{carb}}$, $\delta^{18}\text{O}_{\text{apatite}}$, $^{87}\text{Sr}/^{86}\text{Sr}$, $\delta^{44}/^{40}\text{Ca}_{\text{apatite}}$,

$\delta^{34}\text{S}$, and Hg/TOC), we suspect that the largest regression and Emeishan LIP volcanism are the combined triggers, and climate change, ocean anoxia, and gaseous metal loading are primary kill mechanisms for biodiversity loss in the end-Guadalupian.

- (3) High volcanic flux (i.e., eruption rate) and gas production ensured the Siberian Traps eruptions most deadly, in comparison with other LIPs. Moreover, the high-precision timeline of major changes in geochemical proxies such as $\delta^{13}\text{C}_{\text{carb}}$, $\delta^{18}\text{O}_{\text{apatite}}$, $\delta^{44}/^{40}\text{Ca}_{\text{apatite}}$, [Zn] and $\delta^{66}\text{Zn}$, Hg/TOC, and $\delta^{7}\text{Li}_{\text{seawater}}$ strongly suggests that, the switch from dominantly extrusive eruptions to widespread emplaced history of the Siberian Traps, and is the most plausible trigger for the end-Permian mass extinction.
- (4) Arc volcanism in the Palaeotethys realm could have also played an important role in the end-Permian mass extinction, given the fact that volcanic ash layers around the PTB in South China are crustal-derived acidic origin, rather than mantle origin from the Siberian Traps, and continental arc volcanism is more frequent and intense in the latest Permian and earliest Triassic, corresponding to the most dramatic biodiversity decline.

Acknowledgements

T.J. Horscroft and M. Santosh are thanked for the invitation of this contribution. We also thank S.Z. Shen, F.Y. Wu, C.Q. Cao, B. He, and Y.T. Zhong for useful discussions and suggestions. The comments from two anonymous reviewers are gratefully appreciated. This work was financially supported by the Strategic Priority Research Program (B) of the Chinese Academy of Sciences (XDB18000000) and National Basic Research Program of China (2011CB808906). This is contribution No. IS-2664 from GIGCAS.

References

- Aarnes, I., Fristad, K., Planke, S., Svensen, H., 2011. The impact of host-rock composition on devolatilization of sedimentary rocks during contact metamorphism around mafic sheet intrusions. *Geochemistry Geophysics Geosystems* 12, Q10019.
- Algeo, T.J., Chen, Z.Q., Fraiser, M.L., Twitchett, R.J., 2011. Terrestrial-marine teleconnections in the collapse and rebuilding of Early Triassic marine ecosystems. *Palaearcogeogr. Palaeoclimatol. Palaeoecol.* 308, 1–11.
- Alroy, J., Aberhan, M., Bottjer, D.J., Foote, M., Fursich, F.T., Harries, P.J., Hendy, A.J., Holland, S.M., Ivany, L.C., Kiessling, W., Kosnik, M.A., Marshall, C.R., McGowan, A.J., Miller, A.J., Olszewski, T.D., Patzkowsky, M.E., Peters, S.E., Villier, L., Wagner, P.J., Bonuso, N., Borkow, P.S., Bremnes, B., Clapham, M.E., Fall, L.M., Ferguson, C.A., Hanson, V.L., Krug, A.Z., Layou, K.M., Leckey, E.H., Nurnberg, S., Powers, C.M., Sessa, J.A., Simpson, C., Tomasovich, A., Visaggi, C.C., 2008. Phanerozoic trends in the global diversity of marine invertebrates. *Science* 321, 97–100.
- Attrep, M.J., Orth, C.J., Quintana, L.R., 1991. The Permian-Triassic of the Gartnerkoefel-1 core (Carnic Alps, Austria): Geochemistry of common and trace elements II—INAA and RNAA. *Abhandlung der Geologischen Bundesanstalt* 45, 123–137.
- Bagherpour, B., Bucher, H., Baud, A., Brosse, M., Vennemann, T., Martini, R., Kuang, G.D., 2017. Onset, development, and cessation of basal Early Triassic microbialites (BETM) in the Nanpanjiang pull-apart Basin, South China Block. *Gondwana Res.* 44, 178–204.
- Bagherpour, B., Bucher, H., Schneebeli-Hermann, E., Vennemann, T., Chiaradia, M., Shen, S.Z., 2018a. Early Late Permian coupled carbon and strontium isotope chemostratigraphy from South China: Extended Emeishan volcanism? *Gondwana Res.* 58, 58–70.
- Bagherpour, B., Bucher, H., Yuan, D.X., Leu, M., Zhang, C., Shen, S.Z., 2018b. Early Wuchiapingian (Lopingian, late Permian) drowning event in the South China block suggests a late eruptive phase of Emeishan large Igneous Province. *Glob. Planet. Chang.* 169, 119–132.
- Bambach, R.K., 2006. Phanerozoic biodiversity mass extinctions. *Annu. Rev. Earth Planet. Sci.* 34, 127–155.
- Bambach, R.K., Knoll, A.H., Wang, S.C., 2004. Origination, extinction, and mass depletions of marine diversity. *Paleobiology* 30, 522–542.
- Baud, A., Magaritz, M., Holser, W.T., 1989. Permian-Triassic of the Tethys: Carbon isotope studies. *Geol. Rundsch.* 78, 649–677.
- Benca, J.P., Duijnsteek, I.A.P., Looy, C.V., 2018. UV-B-induced forest sterility: Implications of ozone shield failure in Earth's largest extinction. *Sci. Adv.* 4, e1700618.
- Bergquist, B.A., 2017. Mercury, volcanism, and mass extinctions. *Proc. Natl. Acad. Sci. U. S. A.* 114, 8675–8677.
- Bergquist, B.A., Blum, J.D., 2007. Mass-dependent and -independent fractionation of Hg isotopes by photoreduction in aquatic systems. *Science* 318, 417–420.

- Bergquist, R.A., Blum, J.D., 2009. The odds and evens of mercury isotopes: applications of mass-dependent and mass-independent isotope fractionation. *Elements* 5, 353–357.
- Berner, R.A., 1991. Atmospheric oxygen over Phanerozoic time. *Am. J. Sci.* 291, 339–376.
- Black, B.A., Elkins-Tanton, L.T., Rowe, M.C., Peate, I.J., 2012. Magnitude and consequences of volatile release from the Siberian Traps. *Earth Planet. Sci. Lett.* 317, 363–373.
- Black, B.A., Hauri, E.H., Elkins-Tanton, L.T., Brown, S.M., 2014a. Sulfur isotopic evidence for sources of volatiles in Siberian Traps magmas. *Earth Planet. Sci. Lett.* 394, 58–69.
- Black, B.A., Lamarque, J.F., Shields, C.A., Elkins-Tanton, L.T., Kiehl, J.T., 2014b. Acid rain and ozone depletion from pulsed Siberian Traps magmatism. *Geology* 42, 67–70.
- Black, B.A., Neely, R.R., Lamarque, J.-F., Elkins-Tanton, L.T., Kiehl, J.T., Shields, C.A., Mills, M.J., Bardeen, C., 2018. Systematic swings in end-Permian climate from Siberian Traps carbon and sulfur outgassing. *Nat. Geosci.* 11, 949–954.
- Blum, J.D., Sherman, L.S., Johnson, M.W., 2014. Mercury isotopes in earth and environmental sciences. *Annu. Rev. Earth Planet. Sci.* 42, 249–269.
- Bond, D.P.G., Grasby, S.E., 2017. On the causes of mass extinctions. *Palaeogeogr. Palaeoclimatol. Palaeoecol.* 478, 3–29.
- Bond, D.P.G., Wignall, P.B., 2010. Pyrite frambooid study of marine Permian-Triassic boundary sections: a complex anoxic event and its relationship to contemporaneous mass extinction. *Geol. Soc. Am. Bull.* 122, 1265–1279.
- Bond, D.P.G., Wignall, P.B., 2014. Large igneous provinces and mass extinctions: an update. Keller, G., Kerr, A.C. (Eds.), *Volcanism, Impacts, and Mass Extinctions: Causes and Effects*. Geological Society of America Special Paper 505, 29–55.
- Bond, D.P.G., Hilton, J., Wignall, P.B., Ali, J.R., Stevens, L.G., Sun, Y.D., Lai, X.L., 2010a. The Middle Permian (Capitanian) mass extinction on land and in the oceans. *Earth Sci. Rev.* 102, 100–116.
- Bond, D.P.G., Wignall, P.B., Wang, W., Izon, G., Jiang, H.S., Lai, X.L., Sun, Y.D., Newton, R.J., Shao, L.Y., Vedrine, S., Cope, H., 2010b. The mid-Capitanian (Middle Permian) mass extinction and carbon isotope record of South China. *Palaeogeogr. Palaeoclimatol. Palaeoecol.* 292, 282–294.
- Bowring, S.A., Erwin, D.H., Jin, Y.G., Martin, M.W., Davidek, K., Wang, W., 1998. U/Pb zircon geochronology and tempo of the end-Permian mass extinction. *Science* 280, 1039–1045.
- Brand, U., Posenato, R., Came, R., Affek, H., Angiolini, L., Azmy, K., Farabegoli, E., 2012. The end-Permian mass extinction: a rapid volcanic CO₂ and CH₄-climatic catastrophe. *Chem. Geol.* 322, 121–144.
- Brayard, A., Escarguel, G., Bucher, H., Monnet, C., Bruhwiler, T., Goudemand, N., Galfetti, T., Guex, J., 2009. Good genes and good luck: ammonoid diversity and the end-Permian mass extinction. *Science* 325, 1118–1121.
- Brennecke, G.A., Herrmann, A.D., Algeo, T.J., Anbar, A.D., 2011. Rapid expansion of oceanic anoxia immediately before the end-Permian mass extinction. *Proc. Natl. Acad. Sci. U. S. A.* 108, 17631–17634.
- Broadley, M.W., Barry, P.H., Ballentine, C.J., Taylor, L.A., Burgess, R., 2018. End-Permian extinction amplified by plume-induced release of recycled lithospheric volatiles. *Nat. Geosci.* 11, 682–687.
- Buggisch, W., Wang, X.D., Alekseev, A.S., Joachimski, M.M., 2011. Carboniferous-Permian carbon isotope stratigraphy of successions from China (Yangtze platform), USA (Kansas) and Russia (Moscow Basin and Urals). *Palaeogeogr. Palaeoclimatol. Palaeoecol.* 301, 18–38.
- Buggisch, W., Krainer, K., Schaffhauser, M., Joachimski, M., Korte, C., 2015. Late Carboniferous to Late Permian carbon isotope stratigraphy: a new record from post-Variscan carbonates from the Southern Alps (Austria and Italy). *Palaeogeogr. Palaeoclimatol. Palaeoecol.* 433, 174–190.
- Burgess, S.D., Bowring, S.A., 2015. High-precision geochronology confirms voluminous magmatism before, during, and after Earth's most severe extinction. *Sci. Adv.* 1, e1500470.
- Burgess, S.D., Bowring, S.A., Shen, S.Z., 2014. High-precision timeline for Earth's most severe extinction. *Proc. Natl. Acad. Sci. U. S. A.* 111, 3316–3321.
- Burgess, S.D., Muirhead, J.D., Bowring, S.A., 2017. Initial pulse of Siberian Traps sills as the trigger of the end-Permian mass extinction. *Nat. Commun.* 8, 164.
- Burke, W.H., Denison, R.E., Hetherington, E.A., Koepnick, R.B., Nelson, H.F., Otto, J.B., 1982. Variation of seawater ⁸⁷Sr/⁸⁶Sr throughout Phanerozoic time. *Geology* 10, 516–519.
- Cao, C.Q., Wang, W., Jin, Y.G., 2002. Carbon isotope excursions across the Permian-Triassic boundary in the Meishan section, Zhejiang Province, China. *Chin. Sci. Bull.* 47, 1125–1129.
- Cao, C.Q., Love, G.D., Hays, L.E., Wang, W., Shen, S.Z., Summons, R.E., 2009. Biogeochemical evidence for euxinic oceans and ecological disturbance presaging the end-Permian mass extinction event. *Earth Planet. Sci. Lett.* 281, 188–201.
- Cao, C.Q., Cui, C., Chen, J., Summons, R.E., Shen, S.Z., Zhang, H., 2018. A positive C-isotope excursion induced by sea-level fall in the middle Capitanian of South China. *Palaeogeogr. Palaeoclimatol. Palaeoecol.* 505, 305–316.
- Cao, Y., Song, H., Algeo, T.J., Chu, D., Du, Y., Tian, L., Wang, Y., Tong, J., 2019. Intensified chemical weathering during the Permian-Triassic transition recorded in terrestrial and marine successions. *Palaeogeogr. Palaeoclimatol. Palaeoecol.* 519, 166–177.
- Castillo, P., Fanning, C.M., Pankhurst, R.J., Herve, F., Rapela, C.W., 2017. Zircon O- and Hf-isotope constraints on the genesis and tectonic significance of Permian magmatism in Patagonia. *J. Geol. Soc.* 174, 803–816.
- Chan, L.H., Edmond, J.M., 1988. Variation of lithium isotope composition in the marine environment: a preliminary report. *Geochim. Cosmochim. Acta* 52, 1711–1717.
- Chan, L.H., Leeman, W.P., Plank, T., 2006. Lithium isotopic composition of marine sediments. *Geochemistry Geophysics Geosystems* 7, Q06005.
- Charbonnier, G., Follmi, K.B., 2017. Mercury enrichments in lower Aptian sediments support the link between Ontong Java large igneous province activity and oceanic anoxic episode 1a. *Geology* 45, 63–66.
- Chen, B., Joachimski, M.M., Sun, Y.D., Shen, S.Z., Lai, X.L., 2011. Carbon and conodont apatite oxygen isotope records of Guadalupian-Lopingian boundary sections: climatic or sea-level signal? *Palaeogeogr. Palaeoclimatol. Palaeoecol.* 311, 145–153.
- Chen, B., Joachimski, M.M., Shen, S.Z., Lambert, L.L., Lai, X.L., Wang, X.D., Chen, J., Yuan, D.X., 2013. Permian ice volume and palaeoclimate history: oxygen isotope proxies revisited. *Gondwana Res.* 24, 77–89.
- Chen, B., Joachimski, M.M., Wang, X.D., Shen, S.Z., Qi, Y.P., Qie, W.K., 2016a. Ice volume and paleoclimate history of the Late Paleozoic Ice Age from conodont apatite oxygen isotopes from Naqing (Guizhou, China). *Palaeogeogr. Palaeoclimatol. Palaeoecol.* 448, 151–161.
- Chen, J., Xu, Y.G., 2017. Permian large igneous provinces and their impact on paleoenvironment and biodiversity: progresses and perspectives. *Bull. Mineral. Petrol. Geochem.* 36, 374–393 (in Chinese).
- Chen, J., Beatty, T.W., Henderson, C.M., Rowe, H., 2009. Conodont biostratigraphy across the Permian-Triassic boundary at the Dawen section, Great Bank of Guizhou, Guizhou Province, South China: Implications for the Late Permian extinction and correlation with Meishan. *J. Asian Earth Sci.* 36, 442–458.
- Chen, J., Shen, S.Z., Li, X.H., Xu, Y.G., Joachimski, M.M., Bowring, S.A., Erwin, D.H., Yuan, D.X., Chen, B., Zhang, H., Wang, Y., Cao, C.Q., Zheng, Q.F., Mu, L., 2016b. High-resolution SIMS oxygen isotope analysis on conodont apatite from South China and implications for the end-Permian mass extinction. *Palaeogeogr. Palaeoclimatol. Palaeoecol.* 448, 26–38.
- Chen, J.B., Zhao, L.S., Algeo, T.J., Zhou, L., Zhang, L., Qiu, H., 2019. Evaluation of paleomarine redox conditions using Mo-isotope data in low-[Mo] sediments: a case study from the Lower Triassic of South China. *Palaeogeogr. Palaeoclimatol. Palaeoecol.* 519, 178–193.
- Chen, J.S., Shao, M.R., Huo, W.G., Yao, Y.Y., 1984. Carbon isotope of carbonate strata at Permian-Triassic boundary in Changxing, Zhejiang. *Sci. Geol. Sin.* 19, 88–93 (in Chinese).
- Chen, J.T., Montañez, I.P., Qi, Y.P., Shen, S.Z., Wang, X.D., 2018. Strontium and carbon isotopic evidence for decoupling of pCO₂ from continental weathering at the apex of the late Paleozoic glaciation. *Geology* 46, 395–398.
- Chen, Z.Q., Yang, H., Luo, M., Benton, M.J., Kaiho, K., Zhao, L., Huang, Y., Zhang, K., Fang, Y., Jiang, H., Qiu, H., Li, Y., Tu, C., Shi, L., Zhang, L., Feng, X., Chen, L., 2015. Complete biotic and sedimentary records of the Permian-Triassic transition from Meishan section, South China: ecologically assessing mass extinction and its aftermath. *Earth Sci. Rev.* 149, 67–107.
- Cheng, C., Li, S., Xie, X., Cao, T., Manger, W.L., Busbey, A.B., 2019. Permian carbon isotope and clay mineral records from the Xikou section, Zhen'an, Shaanxi Province, central China: climatological implications for the easternmost Paleo-Tethys. *Palaeogeogr. Palaeoclimatol. Palaeoecol.* 514, 407–422.
- Clapham, M.E., 2015. Ecological consequences of the Guadalupian extinction and its role in the brachiopod-mollusk transition. *Paleobiology* 41, 266–279.
- Clapham, M.E., Payne, J.L., 2011. Acidification, anoxia, and extinction: a multiple logistic regression analysis of extinction selectivity during the Middle and Late Permian. *Geology* 39, 1059–1062.
- Clapham, M.E., Shen, S.Z., Bottjer, D.J., 2009. The double mass extinction revisited: reassessing the severity, selectivity, and causes of the end-Guadalupian biotic crisis (Late Permian). *Paleobiology* 35, 32–50.
- Clarkson, M.O., Richoz, S., Wood, R.A., Maurer, F., Krystyn, L., McGurry, D.J., Astratti, D., 2013. A new high-resolution d¹³C record for the Early Triassic: insights from the Arabian Platform. *Gondwana Res.* 24, 233–242.
- Clarkson, M.O., Kasemann, S.A., Wood, R.A., Lenton, T.M., Daines, S.J., Richoz, S., Ohnmueller, F., Meixner, A., Poulton, S.W., Tipper, E.T., 2015. Ocean acidification and the Permo-Triassic mass extinction. *Science* 348, 229–232.
- Clarkson, M.O., Wood, R.A., Poulton, S.W., Richoz, S., Newton, R.J., Kasemann, S.A., Bowyer, F., Krystyn, L., 2016. Dynamic anoxic ferruginous conditions during the end-Permian mass extinction and recovery. *Nat. Commun.* 7, 12236.
- Courtillot, V., 1999. *Evolutionary Catastrophes: The Science of Mass Extinction*. Cambridge University Press, New York.
- Courtillot, V., Fluteau, F., 2014. A review of the embedded time scales of flood basalt volcanism with special emphasis on dramatically short magmatic pulses. Keller, G., Kerr, A.C. (Eds.), *Volcanism, Impacts, and Mass Extinctions: Causes and Effects*. Geological Society of America Special Paper 505, 301–317.
- Courtillot, V.E., Renne, P.R., 2003. On the ages of flood basalt events. *Compt. Rendus Geosci.* 335, 113–140.
- Cui, Y., Bercovici, A., Yu, J.X., Kump, L.R., Freeman, K.H., Su, S.G., Vajda, V., 2017. Carbon cycle perturbation expressed in terrestrial Permian-Triassic boundary sections in South China. *Glob. Planet. Chang.* 148, 272–285.
- Dessert, C., Dupre, B., Gaillardet, J., Francois, L.M., Allegre, C.J., 2003. Basalt weathering laws and the impact of basalt weathering on the global carbon cycle. *Chem. Geol.* 202, 257–273.
- Dolenec, T., Lojen, S., Ramovs, A., 2001. The Permian-Triassic boundary in Western Slovenia (Idrijca Valley section): magnetostratigraphy, stable isotopes, and elemental variations. *Chem. Geol.* 175, 175–190.
- Doney, S.C., Fabry, V.J., Feely, R.A., Kleypas, J.A., 2009. Ocean Acidification: The Other CO₂ Problem. *Annu. Rev. Mar. Sci.* 1, 169–192.
- Dudas, F.O., Yuan, D.X., Shen, S.Z., Bowring, S.A., 2017. A conodont-based revision of the ⁸⁷Sr/⁸⁶Sr seawater curve across the Permian-Triassic boundary. *Palaeogeogr. Palaeoclimatol. Palaeoecol.* 470, 40–53.
- Elrick, M., Polyak, V., Algeo, T.J., Romaniello, S., Asmerom, Y., Herrmann, A.D., Anbar, A.D., Zhao, L.S., Chen, Z.Q., 2017. Global-ocean redox variation during the middle-late Permian through Early Triassic based on uranium isotope and Th/U trends of marine carbonates. *Geology* 45, 163–166.
- Eltom, H.A., Abdullaif, O.M., Babalola, L.O., 2017. Redox conditions through the Permian-Triassic transition in the upper Khuff formation, Saudi Arabia. *Palaeogeogr. Palaeoclimatol. Palaeoecol.* 472, 203–215.
- Ernst, R.E., 2014. *Large Igneous Provinces*. Cambridge University Press, Cambridge, UK.

- Ernst, R.E., Buchan, K.L., 2003. Recognizing mantle plumes in the geological record. *Annu. Rev. Earth Planet. Sci.* 31, 469–523.
- Ernst, R.E., Youbi, N., 2017. How Large Igneous Provinces affect global climate, sometimes cause mass extinctions, and represent natural markers in the geological record. *Palaeogeogr. Palaeoclimatol. Palaeoecol.* 478, 30–52.
- Erwin, D.H., 1990. The End-Permian Mass Extinction. *Annu. Rev. Ecol. Syst.* 21, 69–91.
- Erwin, D.H., 2006. Dates and rates: temporal resolution in the deep time stratigraphic record. *Annu. Rev. Earth Planet. Sci.* 34, 569–590.
- Erwin, D.H., 2014. Temporal acuity and the rate and dynamics of mass extinctions. *Proc. Natl. Acad. Sci. U. S. A.* 111, 3203–3204.
- Fan, W.M., Wang, Y.J., Peng, T.P., Miao, L.C., Guo, F., 2004. Ar-Ar and U-Pb geochronology of Late Paleozoic basalts in western Guangxi and its constraints on the eruption age of Emeishan basalt magmatism. *Chin. Sci. Bull.* 49, 2318–2327.
- Fan, W.M., Zhang, C.H., Wang, Y.J., Guo, F., Peng, T.P., 2008. Geochronology and geochemistry of Permian basalts in western Guangxi Province, Southwest China: evidence for plume-litho sphere interaction. *Lithos* 102, 218–236.
- Fielding, C.R., Frank, T.D., McLoughlin, S., Vajda, V., Mays, C., Tevyaw, A.P., Winguth, A., Winguth, C., Nicoll, R.S., Bocking, M., 2019. Age and pattern of the southern high-latitude continental end-Permian extinction constrained by multiproxy analysis. *Nat. Commun.* 10, 385.
- Font, E., Adatte, T., Sial, A.N., de Lacerda, L.D., Keller, G., Punekar, J., 2016. Mercury anomaly, Deccan volcanism, and the end-Cretaceous mass extinction. *Geology* 44, 171–174.
- Foster, C.B., Afonin, S.A., 2005. Abnormal pollen grains: an outcome of deteriorating atmospheric conditions around the Permian-Triassic boundary. *J. Geol. Soc.* 162, 653–659.
- Ganino, C., Arndt, N.T., 2009. Climate changes caused by degassing of sediments during the emplacement of large igneous provinces. *Geology* 37, 323–326.
- Gao, Q.L., Zhang, N., Xia, W.C., Feng, Q.L., Chen, Z.Q., Zheng, J.P., Griffin, W.L., O'Reilly, S.Y., Pearson, N.J., Wang, G.Q., Wu, S., Zhong, W.L., Sun, X.F., 2013. Origin of volcanic ash beds across the Permian-Triassic boundary, Daxiakou, South China: Petrology and U-Pb age, trace elements and Hf-isotope composition of zircon. *Chem. Geol.* 360, 41–53.
- Gao, Q.L., Chen, Z.Q., Zhang, N., Griffin, W.L., Xia, W.C., Wang, G.Q., Jiang, T.F., Xia, X.F., O'Reilly, S.Y., 2015. Ages, Trace Elements and Hf-Isotopic Compositions of Zircons from Claystones around the Permian-Triassic Boundary in the Zunyi Section, South China: Implications for Nature and Tectonic Setting of the Volcanism. *J. Earth Sci.* 26, 872–882.
- Garbelli, C., Angiolini, L., Brand, U., Shen, S.Z., Jadoul, F., Posenato, R., Azmy, K., Cao, C.Q., 2016. Neotethys seawater chemistry and temperature at the dawn of the end Permian mass extinction. *Gondwana Res.* 35, 272–285.
- Garbelli, C., Angiolini, L., Shen, S.Z., 2017. Biomineralization and global change: a new perspective for understanding the end-Permian extinction. *Geology* 45, 19–22.
- Gastaldo, R.A., Neveling, J., 2016. Comment on: "Anatomy of a mass extinction: Sedimentological and taphonomic evidence for drought-induced die-offs at the Permo-Triassic boundary in the main Karoo Basin, South Africa" by RMH Smith and J. Botha-Brink, *Palaeogeography, Palaeoclimatology, Palaeoecology* 396:99–118. *Palaeogeogr. Palaeoclimatol. Palaeoecol.* 447, 88–91.
- Gastaldo, R.A., Neveling, J., Clark, C.K., Newbury, S.S., 2009. The terrestrial Permian-Triassic boundary event bed is a nonevent. *Geology* 37, 199–202.
- Gastaldo, R.A., Knight, C.L., Neveling, J., Tabor, N.J., 2014. Latest Permian paleosols from Wapadsberg Pass, South Africa: Implications for Changhsingian climate. *Geol. Soc. Am. Bull.* 126, 665–679.
- Gastaldo, R.A., Kamo, S.L., Neveling, J., Geissman, J.W., Bamford, M., Looy, C.V., 2015. Is the vertebrate-defined Permian-Triassic boundary in the Karoo Basin, South Africa, the terrestrial expression of the end-Permian marine event? *Geology* 43, 939–942.
- Gastaldo, R.A., Neveling, J., Geissman, J.W., Kamo, S.L., 2018. A lithostratigraphic and magnetostratigraphic framework in a geochronologic context for a purported Permian-Triassic boundary section at Old (West) Loetsberg Pass, Karoo Basin, South Africa. *Geological Society of America Bulletin* 130, 1411–1438.
- Grasby, S.E., Sanei, H., Beauchamp, B., Chen, Z.H., 2013. Mercury deposition through the Permo-Triassic Biotic Crisis. *Chem. Geol.* 351, 209–216.
- Grasby, S.E., Beauchamp, B., Bond, D.P.G., Wignall, P.B., Talavera, C., Galloway, J.M., Piepjahn, K., Reinhardt, L., Blomeier, D., 2015. Progressive environmental deterioration in northwestern Pangea leading to the latest Permian extinction. *Geol. Soc. Am. Bull.* 127, 1331–1347.
- Grasby, S.E., Beauchamp, B., Bond, D.P.G., Wignall, P.B., Sanei, H., 2016. Mercury anomalies associated with three extinction events (Capitanian Crisis, Latest Permian Extinction and the Smithian/Spathian Extinction) in NW Pangea. *Geol. Mag.* 153, 285–297.
- Grasby, S.E., Shen, W.J., Yin, R.S., Gleason, J.D., Blum, J.D., Lepak, R.F., Hurley, J.P., Beauchamp, B., 2017. Isotopic signatures of mercury contamination in latest Permian oceans. *Geology* 45, 55–58.
- Grice, K., Cao, C.Q., Love, G.D., Bottcher, M.E., Twitchett, R.J., Grosjean, E., Summons, R.E., Turgeon, S.C., Dunning, W., Jin, Y.G., 2005a. Photic zone euxinia during the Permian-Triassic superoxic event. *Science* 307, 706–709.
- Grice, K., Twitchett, R.J., Alexander, R., Foster, C.B., Looy, C., 2005b. A potential biomarker for the Permian-Triassic ecological crisis. *Earth Planet. Sci. Lett.* 236, 315–321.
- Grossman, E.L., 2012. Applying oxygen isotope paleothermometry in deep time. The Paleontological Society Papers 18, 39–67.
- Grossman, E.L., Yancey, T.E., Jones, T.E., Bruckschen, P., Chuvashov, B., Mazzullo, S.J., Mii, H.-s., 2008. Glaciation, aridification, and carbon sequestration in the Permo-Carboniferous: the isotopic record from low latitudes. *Palaeogeogr. Palaeoclimatol. Palaeoecol.* 268, 222–233.
- Grotzinger, J.P., Jordan, T.H., 2014. Understanding Earth. 7th edition. W.H. Freeman and Company, New York.
- Groves, J.R., Wang, Y., 2009. Foraminiferal diversification during the late Paleozoic ice age. *Paleobiology* 35, 367–392.
- Groves, J.R., Wang, Y., 2013. Timing and size selectivity of the Guadalupian (Middle Permian) fusulinoidean extinction. *J. Paleontol.* 87, 183–196.
- Guex, J., Schoene, B., Bartolini, A., Spangenberg, J., Schaltegger, U., O'Dogherty, L., Taylor, D., Bucher, H., Atudorei, V., 2012. Geochronological constraints on post-extinction recovery of the ammonoids and carbon cycle perturbations during the Early Jurassic. *Palaeogeogr. Palaeoclimatol. Palaeoecol.* 346, 1–11.
- Gutjahr, M., Ridgwell, A., Sexton, P.F., Anagnostou, E., Pearson, P.N., Páliké, H., Norris, R.D., Thomas, E., Foster, G.L., 2017. Very large release of mostly volcanic carbon during the Palaeocene-Eocene Thermal Maximum. *Nature* 548, 573.
- Hannisdal, B., Peters, S.E., 2011. Phanerozoic Earth system evolution and marine biodiversity. *Science* 334, 1121–1124.
- Hansen, J., Lacis, A., Ruedy, R., Sato, M., 1992. Potential climate impact of Mount Pinatubo eruption. *Geophys. Res. Lett.* 19, 215–218.
- Hanski, E., Walker, R.J., Huhta, H., Polyakov, G.V., Balykin, P.A., Tran Trong, H., Ngo Thi, P., 2004. Origin of the Permian-Triassic komatiites, northwestern Vietnam. *Contrib. Mineral. Petrol.* 147, 453–469.
- Haq, B.U., Schutter, S.R., 2008. A chronology of Paleozoic sea-level changes. *Science* 322, 64–68.
- He, B., Xu, Y.G., Chung, S.L., Xiao, L., Wang, Y., 2003. Sedimentary evidence for a rapid, kilometer-scale crustal doming prior to the eruption of the Emeishan flood basalts. *Earth Planet. Sci. Lett.* 213, 391–405.
- He, B., Xu, Y.G., Huang, X.L., Luo, Z.Y., Shi, Y.R., Yang, Q.J., Yu, S.Y., 2007. Age and duration of the Emeishan flood volcanism, SW China: Geochemistry and SHRIMP zircon U-Pb dating of silicic ignimbrites, post-volcanic Xuanwei Formation and clay tuff at the Chaotian section. *Earth Planet. Sci. Lett.* 255, 306–323.
- He, B., Xu, Y.G., Zhong, Y.T., Guan, J.P., 2010. The Guadalupian-Lopingian boundary mudstones at Chaotian (SW China) are clastic rocks rather than acidic tuffs: Implication for a temporal coincidence between the end-Guadalupian mass extinction and the Emeishan volcanism. *Lithos* 119, 10–19.
- He, B., Zhong, Y.T., Xu, Y.G., Li, X.H., 2014. Triggers of Permo-Triassic boundary mass extinction in South China: the Siberian Traps or Paleo-Tethys ignimbrite flare-up? *Lithos* 204, 258–267.
- Hemming, N.G., Hanson, G.N., 1992. Boron isotopic composition and concentration in modern marine carbonates. *Geochim. Cosmochim. Acta* 56, 537–543.
- Henderson, C.M., Davydov, V.I., Wardlaw, B.R., 2012. The Permian Period. In: Gradstein, F.M., Ogg, J.G., Schmitz, M.D., Ogg, G.M. (Eds.), *The Geological Time Scale 2012*. vol. 2. Elsevier, Amsterdam, pp. 653–680.
- Henkes, G.A., Passey, B.H., Grossman, E.L., Shenton, B.J., Yancey, T.E., Perez-Huerta, A., 2018. Temperature evolution and the oxygen isotope composition of Phanerozoic oceans from carbonate clumped isotope thermometry. *Earth Planet. Sci. Lett.* 490, 40–50.
- Hinojosa, J.L., Brown, S.T., Chen, J., DePaolo, D.J., Paytan, A., Shen, S.Z., Payne, J.L., 2012. Evidence for end-Permian ocean acidification from calcium isotopes in biogenic apatite. *Geology* 40, 743–746.
- Hoa, T.T., Izokh, A.E., Polyakov, G.V., Borisenko, A.S., Anh, T.T., Balykin, P.A., Phuong, N.T., Rudnev, S.N., Van, V.V., Nien, B.A., 2008. Permo-Triassic magmatism and metallogeny of Northern Vietnam in relation to the Emeishan plume. *Russ. Geol. Geophys.* 49, 480–491.
- Hochuli, P.A., Schneebeli-Hermann, E., Mangerud, G., Bucher, H., 2017. Evidence for atmospheric pollution across the Permian-Triassic transition. *Geology* 45, 1123–1126.
- Holser, W.T., Schonlaub, H.P., Attrep, M., Boeckelmann, K., Klein, P., Magaritz, M., Orth, C.J., Fenninger, A., Jenny, C., Kralik, M., Mauritsch, H., Pak, E., Schramm, J.M., Stattegger, K., Schmoller, R., 1989. A unique geochemical record at the Permian/Triassic boundary. *Nature* 337, 39–44.
- Hong, H.L., Fang, Q., Zhao, L.L., Schoepfer, S., Wang, C.W., Gong, N.N., Li, Z.H., Chen, Z.Q., 2017. Weathering and alteration of volcanic ashes in various depositional settings during the Permo-Triassic transition in South China: Mineralogical, elemental and isotopic approaches. *Palaeogeogr. Palaeoclimatol. Palaeoecol.* 486, 46–57.
- Hönisch, B., Hemming, N.G., Loose, B., 2007. Comment on "A critical evaluation of the boron isotope-pH proxy: The accuracy of ancient ocean pH estimates" by M. Pagani, D. Lemarchand, A. Spivack and J. Gaillardet. *Geochim. Cosmochim. Acta* 71, 1636–1641.
- Hönisch, B., Ridgwell, A., Schmidt, D.N., Thomas, E., Gibbs, S.J., Sluijs, A., Zeebe, R., Kump, L., Martindale, R.C., Greene, S.E., Kiessling, W., Ries, J., Zachos, J.C., Royer, D.L., Barker, S., Marchitto, T.M., Moyer, R., Pelejero, C., Ziveri, P., Foster, G.L., Williams, B., 2012. The geological record of ocean acidification. *Science* 335, 1058–1063.
- Hounslow, M.W., Balabanov, Y.P., 2018. A geomagnetic polarity timescale for the Permian, calibrated to stage boundaries. In: Lucas, S.G., Shen, S.Z. (Eds.), *The Permian Timescale*. *Geol. Soc. Lond. Spec. Publ.* 450, 61–103.
- Huang, H., Cawood, P.A., Hou, M.C., Ni, S.J., Yang, J.H., Du, Y.S., Wen, H.G., 2018. Provenance of Late Permian volcanic ash beds in South China: Implications for the age of Emeishan volcanism and its linkage to climate cooling. *Lithos* 314, 293–306.
- Huang, Y.G., Chen, Z.Q., Wignall, P.B., Zhao, L.S., 2017. Latest Permian to Middle Triassic redox condition variations in ramp settings, South China: Pyrite frambooid evidence. *Geol. Soc. Am. Bull.* 129, 229–243.
- Huang, Y.G., Chen, Z.Q., Algeo, T.J., Zhao, L.S., Baud, A., Bhat, G.M., Zhang, L., Guo, Z., 2019a. Two-stage marine anoxia and biotic response during the Permo-Triassic transition in Kashmir, northern India: pyrite frambooid evidence. *Glob. Planet. Chang.* 172, 124–139.
- Huang, Y.G., Chen, Z.Q., Wignall, P.B., Grasby, S.E., Zhao, L.S., Wang, X.D., Kaiho, K., 2019b. Biotic responses to volatile volcanism and environmental stresses over the Guadalupian-Lopingian (Permian) transition. *Geology* 47, 175–178.
- Isozaki, Y., 1997. Permo-triassic boundary superanoxia and stratified superocean: Records from lost deep sea. *Science* 276, 235–238.

- Isozaki, Y., Servais, T., 2018. The Hirnantian (Late Ordovician) and end-Guadalupian (Middle Permian) mass-extinction events compared. *Lethaia* 51, 173–186.
- Isozaki, Y., Kawahata, H., Minoshima, K., 2007a. The Capitanian (Permian) Kamura cooling event: the beginning of the Paleozoic–Mesozoic transition. *Palaeoworld* 16, 16–30.
- Isozaki, Y., Kawahata, H., Ota, A., 2007b. A unique carbon isotope record across the Guadalupian–Lopingian (Middle–Upper Permian) boundary in mid-oceanic paleo-atoll carbonates: the high-productivity "Kamura event" and its collapse in Panthalassa. *Glob. Planet. Chang.* 55, 21–38.
- Isozaki, Y., Aljinović, D., Kawahata, H., 2011. The Guadalupian (Permian) Kamura event in European Tethys. *Palaeogeogr. Palaeoclimatol. Palaeoecol.* 308, 12–21.
- Ivanov, A.V., 2007. Evaluation of Different Models for the Origin of the Siberian Traps. *Plates, Plumes and Planetary Processes*. vol. 430 pp. 669–689.
- Ivanov, A.V., Rasskazov, S.V., Feoktistov, G.D., He, H.Y., Boven, A., 2005. $^{40}\text{Ar}/^{39}\text{Ar}$ dating of Ural'skiy sill in the south-eastern Siberian Traps Large Igneous Province: evidence for long-lived magmatism. *Terra Nova* 17, 203–208.
- Ivanov, A.V., He, H.Y., Yan, L.K., Ryabov, V.V., Shevko, A.Y., Palesskii, S.V., Nikolaeva, I.V., 2013. Siberian Traps large igneous province: evidence for two flood basalt pulses around the Permo-Triassic boundary and in the Middle Triassic, and contemporaneous granitic magmatism. *Earth Sci. Rev.* 122, 58–76.
- Jin, Y.G., 1991. The two stages of end-Permian mass extinction. *Palaeoworld* 1, 39.
- Jin, Y.G., 1993. Pre-Lopingian benthos crisis. *Comptes-Rendus 12th International Congress on Carboniferous and Permian*. vol. 2, pp. 269–278.
- Jin, Y.G., Zhang, J., Shang, Q.H., 1994. Two phases of end-Permian mass extinction. In: Embry, A.F., Beauchamp, B., Glass, D.J. (Eds.), *Pangea: Global environments and resources*. vol. 17. Canadian Society of Petroleum Geologists, Memoir, pp. 813–822.
- Jin, Y.G., Wang, Y., Wang, W., Shang, Q.H., Cao, C.Q., Erwin, D.H., 2000. Pattern of marine mass extinction near the Permian-Triassic boundary in South China. *Science* 289, 432–436.
- Jin, Y.G., Shen, S.Z., Henderson, C.M., Wang, X.D., Wang, W., Wang, Y., Cao, C.Q., Shang, Q.H., 2006. The Global Stratotype Section and Point (GSSP) for the boundary between the Capitanian and Wuchiapingian Stage (Permian). *Episodes* 29, 253–262.
- Joachimski, M.M., Simon, L., van Geldern, R., Lecuyer, C., 2005. Boron isotope geochemistry of Paleozoic brachiopod calcite: Implications for a secular change in the boron isotope geochemistry of seawater over the Phanerozoic. *Geochim. Cosmochim. Acta* 69, 4035–4044.
- Joachimski, M.M., Lai, X.L., Shen, S.Z., Jiang, H.S., Luo, G.M., Chen, B., Chen, J., Sun, Y.D., 2012. Climate warming in the latest Permian and the Permian-Triassic mass extinction. *Geology* 40, 195–198.
- Johansson, L., Zahirovic, S., Müller, R.D., 2018. The interplay between the eruption and weathering of Large Igneous Provinces and the deep-time carbon cycle. *Geophys. Res. Lett.* 45, 5380–5389.
- Jost, A.B., Mundil, R., He, B., Brown, S.T., Altiner, D., Sun, Y.D., DePaolo, D.J., Payne, J.L., 2014. Constraining the cause of the end-Guadalupian extinction with coupled records of carbon and calcium isotopes. *Earth Planet. Sci. Lett.* 396, 201–212.
- Kaiho, K., Kajiwara, Y., Nakano, T., Miura, Y., Kawahata, H., Tazaki, K., Ueshima, M., Chen, Z.Q., Shi, G.R., 2001. End-Permian catastrophe by a bolide impact: evidence of a gigantic release of sulfur from the mantle. *Geology* 29, 815–818.
- Kaiho, K., Chen, Z.Q., Kawahata, H., Kajiwara, Y., Sato, H., 2006. Close-up of the end-Permian mass extinction horizon recorded in the Meishan section, South China: Sedimentary, elemental, and biotic characterization and a negative shift of sulfate sulfur isotope ratio. *Palaeogeogr. Palaeoclimatol. Palaeoecol.* 239, 396–405.
- Kajiwara, Y., Yamakita, S., Ishida, K., Ishiga, H., Imai, A., 1994. Development of a largely anoxic stratified ocean and its temporary massive mixing at the Permian-Triassic boundary supported by the sulfur isotopic record. *Palaeogeogr. Palaeoclimatol. Palaeoecol.* 111, 367–379.
- Kakuwa, Y., Matsumoto, R., 2006. Cerium negative anomaly just before the Permian and Triassic boundary event - the upward expansion of anoxia in the water column. *Palaeogeogr. Palaeoclimatol. Palaeoecol.* 229, 335–344.
- Kamo, S.L., Czamanske, G.K., Krogh, T.E., 1996. A minimum U-Pb age for Siberian flood-basalt volcanism. *Geochim. Cosmochim. Acta* 60, 3505–3511.
- Kamo, S.L., Czamanske, G.K., Amelin, Y., Fedorenko, V.A., Davis, D.W., Trofimov, V.R., 2003. Rapid eruption of Siberian flood-volcanic rocks and evidence for coincidence with the Permian-Triassic boundary and mass extinction at 251 Ma. *Earth Planet. Sci. Lett.* 214, 75–91.
- Kasemann, S.A., Hawkesworth, C.J., Prave, A.R., Fallick, A.E., Pearson, P.N., 2005. Boron and calcium isotope composition in Neoproterozoic carbonate rocks from Namibia: evidence for extreme environmental change. *Earth Planet. Sci. Lett.* 231, 73–86.
- Kasemann, S.A., Prave, A.R., Fallick, A.E., Hawkesworth, C.J., Hoffmann, K.H., 2010. Neoproterozoic ice ages, boron isotopes, and ocean acidification: implications for a snowball Earth. *Geology* 38, 775–778.
- Keller, G., Mateo, P., Punekar, J., Khozeym, H., Gertsch, B., Spangenberg, J., Bitchong, A.M., Adatte, T., 2018. Environmental changes during the Cretaceous-Paleogene mass extinction and Paleocene-Eocene Thermal Maximum: implications for the Anthropocene. *Gondwana Res.* 56, 69–89.
- Knoll, A.H., Bambach, R.K., Payne, J.L., Pruss, S., Fischer, W.W., 2007. Paleophysiology and end-Permian mass extinction. *Earth Planet. Sci. Lett.* 256, 295–313.
- Koch, J.T., Frank, T.D., 2012. Imprint of the Late Palaeozoic Ice Age on stratigraphic and carbon isotopic patterns in marine carbonates of the Orogena Basin, New Mexico, USA. *Sedimentology* 59, 291–318.
- Komar, N., Zeebe, R.E., 2016. Calcium and calcium isotope changes during carbon cycle perturbations at the end-Permian. *Paleoceanography* 31, 115–130.
- Korte, C., Kozur, H.W., 2010. Carbon-isotope stratigraphy across the Permian-Triassic boundary: a review. *J. Asian Earth Sci.* 39, 215–235.
- Korte, C., Kozur, H.W., Joachimski, M.M., Strauss, H., Veizer, J., Schwark, L., 2004. Carbon, sulfur, oxygen and strontium isotope records, organic geochemistry and biostratigraphy across the Permian/Triassic boundary in Abadeh, Iran. *Int. J. Earth Sci.* 93, 565–581.
- Korte, C., Jasper, T., Kozur, H.W., Veizer, J., 2005. $\delta^{18}\text{O}$ and $\delta^{13}\text{C}$ of Permian brachiopods: a record of seawater evolution and continental glaciation. *Palaeogeogr. Palaeoclimatol. Palaeoecol.* 224, 333–351.
- Korte, C., Jones, P.J., Brand, U., Mertmann, D., Veizer, J., 2008. Oxygen isotope values from high-latitudes: Clues for Permian sea-surface temperature gradients and Late Palaeozoic deglaciation. *Palaeogeogr. Palaeoclimatol. Palaeoecol.* 269, 1–16.
- Kump, L.R., Brantley, S.L., Arthur, M.A., 2000. Chemical weathering, atmospheric CO₂, and climate. *Annu. Rev. Earth Planet. Sci.* 28, 611–667.
- Kump, L.R., Braeber, T.J., Ridgwell, A., 2009. Ocean acidification in deep time. *Oceanography* 22, 94–107.
- Kwon, H., Kim, M.G., Lee, Y.I., 2019. Mercury evidence from the Sino-Korean block for Emeishan volcanism during the Capitanian mass extinction. *Geol. Mag.* 156, 1105–1110.
- Lau, K.V., Maher, K., Altiner, D., Kelley, B.M., Kump, L.R., Lehrmann, D.J., Silva-Tamayo, J.C., Weaver, K.L., Yu, M.Y., Payne, J.L., 2016. Marine anoxia and delayed Earth system recovery after the end-Permian extinction. *Proc. Natl. Acad. Sci. U. S. A.* 113, 2360–2365.
- Lau, K.V., Maher, K., Brown, S.T., Jost, A.B., Altiner, D., DePaolo, D.J., Eisenhauer, A., Kelley, B.M., Lehrmann, D.J., Paytan, A., Yu, M., Silva-Tamayo, J.C., Payne, J.L., 2017. The influence of seawater carbonate chemistry, mineralogy, and diagenesis on calcium isotope variations in Lower-Middle Triassic carbonate rocks. *Chem. Geol.* 471, 13–37.
- Le Vaillant, M., Barnes, S.J., Mungall, J.E., Mungall, E.L., 2017. Role of degassing of the Noril'sk nickel deposits in the Permian-Triassic mass extinction event. *Proc. Natl. Acad. Sci. U. S. A.* 114, 2485–2490.
- Lee, C.-T.A., Thurner, S., Paterson, S., Cao, W., 2015. The rise and fall of continental arcs: Interplays between magmatism, uplift, weathering, and climate. *Earth Planet. Sci. Lett.* 425, 105–119.
- Lehrmann, D.J., Bentz, J.M., Wood, T., Goers, A., Dhillon, R., Akin, S., Li, X.W., Payne, J.L., Kelley, B.M., Meyer, K.M., Schaal, E.K., Suarez, M.B., Yu, M.Y., Qin, Y.J., Li, R.X., Minzoni, M., Henderson, C.M., 2015. Environmental controls on the genesis of marine microbialites and dissolution surface associated with the end-Permian mass extinction: New sections and observations from the Nanpanjiang basin, South China. *Palaios* 30, 529–552.
- Lei, L.D., Shen, J., Li, C., Algeo, T.J., Chen, Z.Q., Feng, Q.L., Cheng, M., Jin, C.S., Huang, J.H., 2017. Controls on regional marine redox evolution during Permian-Triassic transition in South China. *Palaeogeogr. Palaeoclimatol. Palaeoecol.* 486, 17–32.
- Lemarchand, D., Gaillardet, J., Lewin, E., Allegre, C.J., 2000. The influence of rivers on marine boron isotopes and implications for reconstructing past ocean pH. *Nature* 408, 951–954.
- Leonova, T.B., 2009. Ammonoid evolution in marine ecosystems prior to the Permian-Triassic crisis. *Paleontol. J.* 43, 858–865.
- Leonova, T.B., 2011. Permian ammonoids: Biostratigraphic, biogeographical, and ecological analysis. *Paleontol. J.* 45, 1206–1312.
- Leonova, T.B., 2016. Major trends in the evolution of Permian ammonoids. *Paleontol. J.* 50, 131–140.
- Li, D.X., Yang, S.F., Chen, H.L., Cheng, X.G., Li, K., Jin, X.L., Li, Z.L., Li, Y.Q., Zou, S.Y., 2014. Late Carboniferous crustal uplift of the Tarim plate and its constraints on the evolution of the Early Permian Tarim Large Igneous Province. *Lithos* 204, 36–46.
- Li, G.S., Wang, Y.B., Shi, G.R., Liao, W., Yu, L.X., 2016. Fluctuations of redox conditions across the Permian-Triassic boundary—New evidence from the GSSP section in Meishan of South China. *Palaeogeogr. Palaeoclimatol. Palaeoecol.* 448, 48–58.
- Li, H.B., Zhang, Z.C., Santosh, M., Lu, L.S., Han, L., Liu, W., 2017. Late Permian basalts in the Yangtze area, eastern Sichuan Province, SW China: Implications for the geodynamics of the Emeishan flood basalt province and Permian global mass extinction. *J. Asian Earth Sci.* 134, 293–308.
- Li, Y.J., He, H.Y., Ivanov, A.V., Demontrova, E.I., Pan, Y.X., Deng, C.L., Zheng, D.W., Zhu, R.X., 2018. Ar-40/Ar-39 age of the onset of high-Ti phase of the Emeishan volcanism strengthens the link with the end-Guadalupian mass extinction. *Int. Geol. Rev.* 60, 1906–1917.
- Li, Z.L., Chen, H.L., Song, B.A., Li, Y.Q., Yang, S.F., Yu, X., 2011. Temporal evolution of the Permian large igneous province in Tarim Basin in northwestern China. *J. Asian Earth Sci.* 42, 917–927.
- Liao, W., Wang, Y.B., Kershaw, S., Weng, Z.T., Yang, H., 2010. Shallow-marine dysoxia across the Permian-Triassic boundary: evidence from pyrite framboids in the microbialite in South China. *Sediment. Geol.* 232, 77–83.
- Liao, Z.W., Hu, W.X., Cao, J., Wang, X.L., Yao, S.P., Wu, H.G., Wan, Y., 2016. Heterogeneous volcanism across the Permian-Triassic Boundary in South China and implications for the Latest Permian Mass Extinction: New evidence from volcanic ash layers in the Lower Yangtze Region. *J. Asian Earth Sci.* 127, 197–210.
- Liu, C., Jarochowska, E., Du, Y.S., Munnecke, A., Dai, X.D., 2017a. Prevailing anoxia in the Kungurian (Permian) of South China: possible response to divergent climate trends between the tropics and Gondwana. *Gondwana Res.* 49, 81–93.
- Liu, C., Jarochowska, E., Du, Y.S., Vachard, D., Munnecke, A., 2017b. Stratigraphical and $\delta^{13}\text{C}$ records of Permo-Carboniferous platform carbonates, South China: responses to late Paleozoic icehouse climate and icehouse-greenhouse transition. *Palaeogeogr. Palaeoclimatol. Palaeoecol.* 474, 113–129.
- Liu, C., Du, Y., Jarochowska, E., Yan, J., Munnecke, A., Lu, G., 2018. A major anomaly in the carbon cycle during the late Cisuralian (Permian): timing, underlying triggers and implications. *Palaeogeogr. Palaeoclimatol. Palaeoecol.* 491, 112–122.
- Liu, S.A., Wu, H.C., Shen, S.Z., Jiang, G.Q., Zhang, S.H., Lv, Y.W., Zhang, H., Li, S.G., 2017c. Zinc isotope evidence for intensive magmatism immediately before the end-Permian mass extinction. *Geology* 45, 343–346.
- Liu, X.J., Liang, Q.D., Li, Z.L., Castillo, P.R., Shi, Y., Xu, J.F., Huang, X.L., Liao, S., Huang, W.L., Wu, W.N., 2017d. Origin of Permian extremely high Ti/Y mafic lavas and dykes from Western Guangxi, SW China: Implications for the Emeishan mantle plume magmatism. *J. Asian Earth Sci.* 141, 97–111.

- Loope, G.R., Kump, L.R., Arthur, M.A., 2013. Shallow water redox conditions from the Permian-Triassic boundary microbialite: the rare earth element and iodine geochemistry of carbonates from Turkey and South China. *Chem. Geol.* 351, 195–208.
- Lucas, S.G., 2018. Permian tetrapod biochronology, correlation and evolutionary events, in: Lucas, S.G., Shen, S.Z. (Eds.), *The Permian timescale*. Geol. Soc. Lond., Spec. Publ. 450, 405–444.
- Lucas, S.G., Shen, S.Z., 2018a. The Permian timescale. *Geol. Soc. Lond., Spec. Publ.* 450.
- Lucas, S.G., Shen, S.Z., 2018b. The Permian timescale: an introduction, in: Lucas, S.G., Shen, S.Z. (Eds.), *The Permian timescale*. Geol. Soc. Lond., Spec. Publ. 450, 1–19.
- Luz, B., Kolodny, Y., Kovach, J., 1984. Oxygen isotope variations in phosphate of biogenic apatites. III. Conodonts. *Earth Planet. Sci. Lett.* 69, 255–262.
- MacLeod, K.G., Quinton, P.C., Bassett, D.J., 2017. Warming and increased aridity during the earliest Triassic in the Karoo Basin, South Africa. *Geology* 45, 483–486.
- Martinez-Botí, M.A., Marino, G., Foster, G.L., Ziveri, P., Henehan, M.J., Rae, J.W.B., Mortyn, P.G., Vance, D., 2015. Boron isotope evidence for oceanic carbon dioxide leakage during the last deglaciation. *Nature* 518, 219–222.
- McArthur, J.M., Howarth, R.J., Shields, G.A., 2012. Strontium isotope stratigraphy. In: Gradstein, F.M., Ogg, J.G., Schmitz, M.D., Ogg, G.M. (Eds.), *The Geological Time Scale 2012*. Elsevier, Amsterdam, pp. 127–144.
- McCormick, M.P., Thomason, L.W., Trepte, C.R., 1995. Atmospheric effects of the Mt Pinatubo eruption. *Nature* 373, 399–404.
- McGhee, G.R., Clapham, M.E., Sheehan, P.M., Bottjer, D.J., Droser, M.L., 2013. A new ecological-severity ranking of major Phanerozoic biodiversity crises. *Palaeogeogr. Palaeoclimatol. Palaeoecol.* 370, 260–270.
- McKay, M.P., Coble, M.A., Hessler, A.M., Weislogel, A.L., Fildani, A., 2016. Petrogenesis and provenance of distal volcanic tuffs from the Permian-Triassic Karoo Basin, South Africa: a window into a dissected magmatic province. *Geosphere* 12, 1–14.
- McKenzie, N.R., Horton, B.K., Loomis, S.E., Stockli, D.F., Planavsky, N.J., Lee, C.-T.A., 2016. Continental arc volcanism as the principal driver of icehouse-greenhouse variability. *Science* 352, 444–447.
- Mei, S.L., Jin, Y.G., Wardlaw, B.R., 1998. Conodont succession of the Guadalupian-Lopingian boundary strata in Laibin of Guangxi, China and west Texas. USA. *Palaeoworld* 9, 53–76.
- Mii, H.S., Shi, G.R., Cheng, C.J., Chen, Y.Y., 2012. Permian Gondwanaland paleoenvironment inferred from carbon and oxygen isotope records of brachiopod fossils from Sydney Basin, southeast Australia. *Chem. Geol.* 291, 87–103.
- Mii, H.S., Shi, G.R., Wang, C., 2013. Late Paleozoic middle-latitude Gondwana environment-stable isotope records from Western Australia. *Gondwana Res.* 24, 125–138.
- Montañez, I.P., 2016. A Late Paleozoic climate window of opportunity. *Proc. Natl. Acad. Sci.* 113, 2334–2336.
- Mundil, R., Metcalfe, I., Ludwig, K.R., Renne, P.R., Oberli, F., Nicoll, R.S., 2001. Timing of the Permian-Triassic biotic crisis: implications from new zircon U/Pb age data (and their limitations). *Earth Planet. Sci. Lett.* 187, 131–145.
- Mundil, R., Ludwig, K.R., Metcalfe, I., Renne, P.R., 2004. Age and timing of the Permian mass extinctions: U/Pb dating of closed-system zircons. *Science* 305, 1760–1763.
- Mungall, J.E., Brenan, J.M., Godel, B., Barnes, S., Gaillard, F., 2015. Transport of metals and sulphur in magmas by flotation of sulphide melt on vapour bubbles. *Nat. Geosci.* 8, 216.
- Muscente, A.D., Prabhu, A., Zhong, H., Eleish, A., Meyer, M.B., Fox, P., Hazen, R.M., Knoll, A.H., 2018. Quantifying ecological impacts of mass extinctions with network analysis of fossil communities. *Proc. Natl. Acad. Sci. U. S. A.* 115, 5217–5222.
- Pagani, M., Spivack, A., 2007. Response to the comment by B. Höönsch, N.G. Hemming, B. Loose on "A critical evaluation of the boron isotope-pH proxy: The accuracy of ancient ocean pH estimates". *Geochim. Cosmochim. Acta* 71, 1642.
- Pagani, M., Lemarchand, D., Spivack, A., Gaillardet, J., 2005. A critical evaluation of the boron isotope-pH proxy: the accuracy of ancient ocean pH estimates. *Geochim. Cosmochim. Acta* 69, 953–961.
- Pavlov, V.E., Fluteau, F., Veselovskiy, R.V., Fetisova, A.M., Latyshev, A.V., 2011. Secular geomagnetic variations and volcanic pulses in the Permian-Triassic traps of the Norilsk and Maimecha-Kotui provinces. *Izvestiya-Physics of the Solid Earth* 47, 402–417.
- Payne, J.L., Lehrmann, D.J., Wei, J.Y., Orchard, M.J., Schrag, D.P., Knoll, A.H., 2004. Large perturbations of the carbon cycle during recovery from the end-Permian extinction. *Science* 305, 506–509.
- Payne, J.L., Lehrmann, D.J., Follett, D., Seibel, M., Kump, L.R., Riccardi, A., Altiner, D., Sano, H., Wei, J., 2007. Erosional truncation of uppermost Permian shallow-marine carbonates and implications for Permian-Triassic boundary events. *Geol. Soc. Am. Bull.* 119, 771–784.
- Payne, J.L., Lehrmann, D.J., Follett, D., Seibel, M., Kump, L.R., Riccardi, A., Altiner, D., Sano, H., Wei, J.Y., 2009. Erosional truncation of uppermost Permian shallow-marine carbonates and implications for Permian-Triassic boundary events: Reply. *Geol. Soc. Am. Bull.* 121, 957–959.
- Payne, J.L., Turchyn, A.V., Paytan, A., Depaolo, D.J., Lehrmann, D.J., Yu, M., Wei, J., 2010. Calcium isotope constraints on the end-Permian mass extinction. *Proc. Natl. Acad. Sci. U. S. A.* 107, 8543–8548.
- Penn, J.L., Deutscher, C., Payne, J.L., Sperling, E.A., 2018. Temperature-dependent hypoxia explains biogeography and severity of end-Permian marine mass extinction. *Science* 362, eaat1327.
- Penniston-Dorland, S., Liu, X.-M., Rudnick, R.L., 2017. Lithium isotope geochemistry. *Reviews in Mineralogy & Geochemistry* 82, 165–217.
- Percival, L.M.E., Ruhl, M., Hesselbo, S.P., Jenkyns, H.C., Mather, T.A., Whiteside, J.H., 2017. Mercury evidence for pulsed volcanism during the end-Triassic mass extinction. *Proc. Natl. Acad. Sci. U. S. A.* 114, 7929–7934.
- Percival, L.M.E., Jenkyns, H.C., Mather, T.A., Dickson, A.J., Batenburg, S.J., Ruhl, M., Hesselbo, S.P., Barclay, R., Jarvis, I., Robinson, S.A., Woelders, L., 2018. Does large igneous province volcanism always perturb the mercury cycle? Comparing the records of Oceanic Anoxic Event 2 and the end-Cretaceous to other Mesozoic events. *Am. J. Sci.* 318, 799–860.
- Peters, S.E., Foote, M., 2001. Biodiversity in the Phanerozoic: a reinterpretation. *Paleobiology* 27, 583–601.
- Polozov, A.G., Svensen, H.H., Planke, S., Grishina, S.N., Fristad, K.E., Jerram, D.A., 2016. The basalt pipes of the Tunguska Basin (Siberia, Russia): high temperature processes and volatile degassing into the end-Permian atmosphere. *Palaeogeogr. Palaeoclimatol. Palaeoecol.* 441, 51–64.
- Proemse, B.C., Grasby, S.E., Wieser, M.E., Mayer, B., Beauchamp, B., 2013. Molybdenum isotopic evidence for oxic marine conditions during the latest Permian extinction. *Geology* 41, 967–970.
- Prokoph, A., Shields, G., Veizer, J., 2008. Compilation and time-series analysis of a marine carbonate $\delta^{18}\text{O}$, $\delta^{13}\text{C}$, $^{87}\text{Sr}/^{86}\text{Sr}$ and $\delta^{34}\text{S}$ database through Earth history. *Earth Sci. Rev.* 87, 113–133.
- Qiu, Z., Sun, S., Wei, H.Y., Wang, Q.C., Zou, C.N., Zhang, Y.J., 2016. SIMS zircon U-Pb dating from bentonites in the Penglaitan Global Stratotype Section for the Guadalupian-Lopingian boundary (GLB), South China. *Geol. J.* 51, 811–816.
- Racki, G., Rakocinski, M., Marynowski, L., Wignall, P.B., 2018. Mercury enrichments and the Frasnian-Famennian biotic crisis: a volcanic trigger proved? *Geology* 46, 543–546.
- Ramezani, J., Bowring, S.A., 2018. Advances in numerical calibration of the Permian timescale based on radioisotopic geochronology, in: Lucas, S.G., Shen, S.Z. (Eds.), *The Permian timescale*. Geol. Soc. Lond., Spec. Publ. 450, 51–60.
- Ramezani, J., Schmitz, M.D., Davydov, V.I., Bowring, S.A., Snyder, W.S., Northrup, C.J., 2007. High-precision $^{87}\text{Sr}/^{86}\text{Sr}$ zircon age constraints on the Carboniferous-Permian boundary in the southern Urals stratotype. *Earth Planet. Sci. Lett.* 256, 244–257.
- Rampino, M.R., Ambrose, S.H., 2000. Volcanic winter in the Garden of Eden: the Toba supereruption and the late Pleistocene human population crash. In: McCoy, F.W., Heiken, G. (Eds.), *Volcanic Hazards and Disasters in Human Antiquity*. vol. 345, pp. 71–82 Geological Society of America Special Paper.
- Rampino, M.R., Self, S., 1992. Volcanic winter and accelerated glaciation following the Toba super-eruption. *Nature* 359, 50–52.
- Rampino, M.R., Stothers, R.B., 1988. Flood basalt volcanism during the past 250 million years. *Science* 241, 663–668.
- Rampino, M.R., Rodriguez, S., Baransky, E., Cai, Y., 2017. Global nickel anomaly links Siberian Traps eruptions and the latest Permian mass extinction. *Sci. Rep.* 7, 12416.
- Raup, D.M., Sepkoski, J.J., 1982. Mass extinctions in the marine fossil record. *Science* 215, 1501–1503.
- Reichow, M.K., Saunders, A.D., White, R.V., Pringle, M.S., Al'Mukhamedov, A.I., Medvedev, A.I., Kirda, N.P., 2002. $^{40}\text{Ar}/^{39}\text{Ar}$ dates from the West Siberian Basin: Siberian flood basalts province doubled. *Science* 296, 1846–1849.
- Reichow, M.K., Pringle, M.S., Al'Mukhamedov, A.I., Allen, M.B., Andreichev, V.L., Buslov, M.M., Davies, C.E., Fedoseev, G.S., Fitton, J.G., Inger, S., Medvedev, A.Y., Mitchell, C., Puchkov, V.N., Safonova, I.Y., Scott, R.A., Saunders, A.D., 2009. The timing and extent of the eruption of the Siberian Traps large igneous province: Implications for the end-Permian environmental crisis. *Earth Planet. Sci. Lett.* 277, 9–20.
- Rey, K., Amiot, R., Fourel, F., Rigaudier, T., Abdala, F., Day, M.O., Fernandez, V., Fluteau, F., France-Lanord, C., Rubidge, B.S., Smith, R.M., Viglietti, P.A., Zipfel, B., Lecuyer, C., 2016. Global climate perturbations during the Permo-Triassic mass extinctions recorded by continental tetrapods from South Africa. *Gondwana Res.* 37, 384–396.
- Rey, K., Day, M.O., Amiot, R., Goedert, J., Lecuyer, C., Sealy, J., Rubidge, B.S., 2018. Stable isotope record implicates aridification without warming during the late Capitanian mass extinction. *Gondwana Res.* 59, 1–8.
- Riccardi, A.L., Arthur, M.A., Kump, L.R., 2006. Sulfur isotopic evidence for chemocline upward excursions during the end-Permian mass extinction. *Geochim. Cosmochim. Acta* 70, 5740–5752.
- Robock, A., 2000. Volcanic eruptions and climate. *Rev. Geophys.* 38, 191–219.
- Rocha-Campos, A.C., Basei, M.A., Nutman, A.P., Kleiman, L.E., Varela, R., Llambias, E., Canile, F.M., Rosa, da, O.d.C.R., 2011. 30 million years of Permian volcanism recorded in the Choyoi igneous province (W Argentina) and their source for younger ash fall deposits in the Paraná Basin: SHRIMP U-Pb zircon geochronology evidence. *Gondwana Res.* 19, 509–523.
- Rong, J.Y., Huang, B., 2014. Study of Mass Extinction over the past thirty years: a synopsis. *SCIENCE CHINA Earth Sciences* 44, 377–404 (in Chinese).
- Ross, P.S., Peate, I.U., McClintock, M.K., Xu, Y.G., Skilling, I.P., White, J.D.L., Houghton, B.F., 2005. Mafic volcanoclastic deposits in flood basalt provinces: a review. *J. Volcanol. Geotherm. Res.* 145, 281–314.
- Rothman, D.H., 2017. Thresholds of catastrophe in the Earth system. *Sci. Adv.* 3, e1700906.
- Rothman, D.H., Fournier, G.P., French, K.L., Alm, E.J., Boyle, E.A., Cao, C.Q., Summons, R.E., 2014. Methanogenic burst in the end-Permian carbon cycle. *Proc. Natl. Acad. Sci. U. S. A.* 111, 5462–5467.
- Saitoh, M., Ueno, Y., Matsu'ura, F., Kawamura, T., Isozaki, Y., Yao, J.X., Ji, Z.S., Yoshida, N., 2017. Multiple sulfur isotope records at the end-Guadalupian (Permian) at Chaotian, China: implications for a role of bioturbation in the Phanerozoic sulfur cycle. *J. Asian Earth Sci.* 135, 70–79.
- Saltzman, M.R., 2017. Silicate weathering, volcanic degassing, and the climate tug of war. *Geology* 45, 763–764.
- Sandler, A., Eshet, Y., Schilman, B., 2006. Evidence for a fungal event, methane-hydrate release and soil erosion at the Permian-Triassic boundary in southern Israel. *Palaeogeogr. Palaeoclimatol. Palaeoecol.* 242, 68–89.
- Sanei, H., Grasby, S.E., Beauchamp, B., 2012. Latest Permian mercury anomalies. *Geology* 40, 63–66.

- Sato, A.M., Llambías, E.J., Basei, M.A.S., Castro, C.E., 2015. Three stages in the Late Paleozoic to Triassic magmatism of southwestern Gondwana, and the relationships with the volcanogenic events in coeval basins. *J. S. Am. Earth Sci.* 63, 48–69.
- Saunders, A., Reichow, M., 2009. The Siberian Traps and the End-Permian mass extinction: a critical review. *Chin. Sci. Bull.* 54, 20–37.
- Schmitz, M.D., Davydov, V.I., 2012. Quantitative radiometric and biostratigraphic calibration of the Pennsylvanian-Early Permian (*Cisuralian*) time scale and pan-Euramerican chronostratigraphic correlation. *Geol. Soc. Am. Bull.* 124, 549–577.
- Schobben, M., Joachimski, M.M., Korn, D., Leda, L., Korte, C., 2014. Palaeotethys seawater temperature rise and an intensified hydrological cycle following the end-Permian mass extinction. *Gondwana Res.* 26, 675–683.
- Schobben, M., van de Velde, S., Gliwa, J., Leda, L., Korn, D., Struck, U., Ullmann, C.V., Hairapetian, V., Ghaderi, A., Korte, C., Newton, R.J., Poulton, S.W., Wignall, P.B., 2017. Latest Permian carbonate carbon isotope variability traces heterogeneous organic carbon accumulation and authigenic carbonate formation. *Clim. Past* 13, 1635–1659.
- Self, S., Widdowson, M., Thordarson, T., Jay, A.E., 2006. Volatile fluxes during flood basalt eruptions and potential effects on the global environment: a Deccan perspective. *Earth Planet. Sci. Lett.* 248, 518–532.
- Self, S., Schmidt, A., Mather, T.A., 2014. Emplacement characteristics, time scales, and volcanic gas release rates of continental flood basalt eruptions on Earth. In: Keller, G., Kerr, A.C. (Eds.), *Volcanism, Impacts, and Mass Extinctions: Causes and Effects*. Geological Society of America Special Paper, vol. 505, pp. 319–337.
- Sengör, A.M.C., Atayman, S., 2009. *The Permian extinction and the Tethys: an exercise in global geology*. Geological Society of America Special Paper 448. Colorado, Boulder.
- Septon, M.A., Jiao, D., Engel, M.H., Looy, C.V., Visscher, H., 2015. Terrestrial acidification during the end-Permian biosphere crisis? *Geology* 43, 159–162.
- Sepkoski, J.J., 1981. A factor analytic description of the Phanerozoic marine fossil record. *Paleobiology* 7, 36–53.
- Sepkoski, J.J., 1996. Patterns of Phanerozoic extinction: a perspective from global data bases. In: Walliser, O.H. (Ed.), *Global Events and Event Stratigraphy in the Phanerozoic*. Springer-Verlag, Berlin, pp. 35–51.
- Shangguan, S.M., Peate, I.U., Tian, W., Xu, Y.G., 2016. Re-evaluating the geochronology of the Permian Tarim magmatic province: implications for temporal evolution of magmatism. *J. Geol. Soc.* 173, 228–239.
- Shellnutt, J.G., 2014. The Emeishan large igneous province: a synthesis. *Geosci. Front.* 5, 369–394.
- Shellnutt, J.G., 2018. The Panjal Traps. In: Sensarma, S., Storey, B.C. (Eds.), *Large Igneous Provinces from Gondwana and Adjacent Regions*. Geological Society, London, Special Publications, vol. 463, pp. 59–86.
- Shellnutt, J.G., Denysyn, S.W., Mundil, R., 2012. Precise age determination of mafic and felsic intrusive rocks from the Permian Emeishan large igneous province (SW China). *Gondwana Res.* 22, 118–126.
- Shen, J., Feng, Q.L., Algeo, T.J., Li, C., Planavsky, N.J., Zhou, L., Zhang, M.L., 2016. Two pulses of oceanic environmental disturbance during the Permian-Triassic boundary crisis. *Earth Planet. Sci. Lett.* 443, 139–152.
- Shen, S.Z., Shi, G.R., 1996. Diversity and extinction patterns of Permian Brachiopoda of South China. *Hist. Biol.* 12, 93–110.
- Shen, S.Z., Shi, G.R., 2002. Paleobiogeographical extinction patterns of Permian brachiopods in the Asian-western Pacific region. *Paleobiology* 28, 449–463.
- Shen, S.Z., Shi, G.R., 2009. Latest Guadalupian brachiopods from the Guadalupian/Lopingian boundary GSSP section at Penglaitan in Laibin, Guangxi, South China and implications for the timing of the pre-Lopingian crisis. *Palaeoworld* 18, 152–161.
- Shen, S.Z., Zhang, H., 2017. What caused the five mass extinctions? *Chin. Sci. Bull.* 62, 1119–1135 (in Chinese).
- Shen, S.Z., Zhang, H., Li, W.Z., Mu, L., Xie, J.F., 2006. Brachiopod diversity patterns from Carboniferous to Triassic in South China. *Geol. J.* 41, 345–361.
- Shen, S.Z., Henderson, C.M., Bowring, S.A., Cao, C.Q., Wang, Y., Wang, W., Zhang, H., Zhang, Y.C., Mu, L., 2010. High-resolution Lopingian (Late Permian) timescale of South China. *Geol. J.* 45, 122–134.
- Shen, S.Z., Crowley, J.L., Wang, Y., Bowring, S.A., Erwin, D.H., Sadler, P.M., Cao, C.Q., Rothman, D.H., Henderson, C.M., Ramezani, J., Zhang, H., Shen, Y.N., Wang, X.D., Wang, W., Mu, L., Li, W.Z., Tang, Y.G., Liu, X.L., Liu, L.J., Zeng, Y., Jiang, Y.F., Jin, Y.G., 2011a. Calibrating the end-Permian mass extinction. *Science* 334, 1367–1372.
- Shen, S.Z., Cao, C.Q., Zhang, H., Bowring, S.A., Henderson, C.M., Payne, J.L., Davydov, V.I., Chen, B., Yuan, D.X., Zhang, Y.C., Wang, W., Zheng, Q.F., 2013. High-resolution $\delta^{13}\text{C}_{\text{carb}}$ chemostratigraphy from latest Guadalupian through earliest Triassic in South China and Iran. *Earth Planet. Sci. Lett.* 375, 156–165.
- Shen, S.Z., Ramezani, J., Chen, J., Cao, C.Q., Erwin, D.H., Zhang, H., Xiang, L., Schoepfer, S.D., Henderson, C.M., Zheng, Q.F., Bowring, S.A., Wang, Y., Li, X.H., Wang, X.D., Yuan, D.X., Zhang, Y.C., Mu, L., Wang, J., Wu, Y.S., 2019a. A sudden end-Permian mass extinction in South China. *Geol. Soc. Am. Bull.* 131, 205–223.
- Shen, S.Z., Zhang, H., Zhang, Y.C., Yuan, D.X., Chen, B., He, W.H., Mu, L., Lin, W., Wang, W.Q., Chen, J., Wu, Q., Cao, C.Q., Wang, Y., Wang, X.D., 2019b. Permian integrative stratigraphy and timescale of China. *SCIENCE CHINA Earth Sciences* 62, 154–188.
- Shen, W.J., Lin, Y.T., Xu, L., Li, J.F., Wu, Y.S., Sung, Y.G., 2007. Pyrite framboids in the Permian-Triassic boundary section at Meishan, China: evidence for dysoxic deposition. *Palaeogeogr. Palaeoclimatol. Palaeoecol.* 253, 323–331.
- Shen, W.J., Lin, Y.T., Sun, Y.G., Xu, L., Zhang, H., 2008. Black carbon record across the Permian-Triassic boundary section at Meishan, Changhsing County, Zhejiang Province and its significance. *Acta Petrol. Sin.* 24, 2407–2414 (in Chinese).
- Shen, W.J., Sun, Y.G., Lin, Y.T., Liu, D.H., Chai, P.X., 2011b. Evidence for wildfire in the Meishan section and implications for Permian-Triassic events. *Geochim. Cosmochim. Acta* 75, 1992–2006.
- Shen, Y.A., Farquhar, J., Zhang, H., Masterson, A., Zhang, T.G., Wing, B.A., 2011c. Multiple Sr-isotopic evidence for episodic shoaling of anoxic water during Late Permian mass extinction. *Nat. Commun.* 2, 210.
- Sial, A.N., Gaucher, C., da Silva, M.A., Ferreira, V.P., Pimentel, M.M., Lacerda, L.D., Silva, E.V., Cezario, W., 2010. C-, Sr-isotope and Hg chemostratigraphy of Neoproterozoic cap carbonates of the Sergipano Belt, Northeastern Brazil. *Precambrian Res.* 182, 351–372.
- Sial, A.N., Chen, J.B., Lacerda, L.D., Frei, R., Tewari, V.C., Pandit, M.K., Gaucher, C., Ferreira, V.P., Cirilli, S., Peralta, S., Korte, C., Barbosa, J.A., Pereira, N.S., 2016. Mercury enrichment and Hg isotopes in Cretaceous-Paleogene boundary successions: Links to volcanism and palaeoenvironmental impacts. *Cretac. Res.* 66, 60–81.
- Silva-Tamayo, J.C., Lau, K.V., Just, A.B., Payne, J.L., Wignall, P.B., Newton, R.J., Eisenhauer, A., Depaolo, D.J., Brown, S., Maher, K., Lehrmann, D.J., Altiner, D., Yu, M.Y., Richoz, S., Paytan, A., 2018. Global perturbation of the marine calcium cycle during the Permian-Triassic transition. *Geol. Soc. Am. Bull.* 130, 1323–1338.
- Smith, R.M.H., Botha-Brink, J., 2014. Anatomy of a mass extinction: Sedimentological and taphonomic evidence for drought-induced die-offs at the Permo-Triassic boundary in the main Karoo Basin, South Africa. *Palaeogeogr. Palaeoclimatol. Palaeoecol.* 396, 99–118.
- Sobolev, A.V., Krivolutskaya, N.A., Kuzmin, D.V., 2009. Petrology of the parental melts and mantle sources of Siberian trap magmatism. *Petrology* 17, 253–286.
- Sobolev, S.V., Sobolev, A.V., Kuzmin, D.V., Krivolutskaya, N.A., Petrunin, A.G., Arndt, N.T., Radko, V.A., Vasilev, Y.R., 2011. Linking mantle plumes, large igneous provinces and environmental catastrophes. *Nature* 477, 312–316.
- Song, H.J., Wignall, P.B., Tong, J.N., Yin, H.F., 2013. Two pulses of extinction during the Permian-Triassic crisis. *Nat. Geosci.* 6, 52–56.
- Song, H.J., Wignall, P.B., Tong, J.N., Song, H.Y., Chen, J., Chu, D.L., Tian, L., Luo, M., Zong, K.Q., Chen, Y.L., Lai, X.L., Zhang, K.X., Wang, H.M., 2015. Integrated Sr isotope variations and global environmental changes through the Late Permian to early Late Triassic. *Earth Planet. Sci. Lett.* 424, 140–147.
- Stampfli, G.M., Borel, G.D., 2004. The TRANSMED transects in space and time: constraints on the paleotectonic evolution of the Mediterranean Domain. In: Cavazza, W., Roue, F., Spakman, W., Stampfli, G.M., Ziegler, P. (Eds.), *The TRANSMED Atlas: The Mediterranean Region from Crust to Mantle*. Springer, Berlin Heidelberg, pp. 1–141.
- Stanley, S.M., 2016. Estimates of the magnitudes of major marine mass extinctions in earth history. *Proc. Natl. Acad. Sci. U. S. A.* 113, E6325–E6334.
- Stanley, S.M., Yang, X.N., 1994. A double mass extinction at the end of the Paleozoic Era. *Science* 266, 1340–1344.
- Sun, H., Xiao, Y., Gao, Y., Zhang, G., Casey, J.F., Shen, Y., 2018. Rapid enhancement of chemical weathering recorded by extremely light seawater lithium isotopes at the Permian-Triassic boundary. *Proc. Natl. Acad. Sci. U. S. A.* 115, 3782–3787.
- Sun, Y.D., Lai, X.L., Wignall, P.B., Widdowson, M., Ali, J.R., Jiang, H.S., Wang, W., Yan, C.B., Bond, D.P.G., Vedrine, S., 2010. Dating the onset and nature of the Middle Permian Emeishan large igneous province eruptions in SW China using conodont biostratigraphy and its bearing on mantle plume uplift models. *Lithos* 119, 20–33.
- Sun, Y.D., Joachimski, M.M., Wignall, P.B., Yan, C.B., Chen, Y.L., Jiang, H.S., Wang, L.N., Lai, X.L., 2012. Lethally hot temperatures during the Early Triassic greenhouse. *Science* 338, 366–370.
- Sun, Y.D., Liu, X.T., Yan, J.X., Li, B., Chen, B., Bond, D.P.G., Joachimski, M.M., Wignall, P.B., Wang, X., Lai, X.L., 2017. Permian (Artinskian to Wuchapingian) conodont biostratigraphy in the Tieqiao section, Laibin area, South China. *Palaeogeogr. Palaeoclimatol. Palaeoecol.* 465, 42–63.
- Svensen, H., Planke, S., Polozov, A.G., Schmidbauer, N., Corfu, F., Podladchikov, Y.Y., Jamtveit, B., 2009. Siberian gas venting and the end-Permian environmental crisis. *Earth Planet. Sci. Lett.* 277, 490–500.
- Svensen, H.H., Frolov, S., Akhmanov, G.G., Polozov, A.G., Jerram, D.A., Shiganova, O.V., Melnikov, N.V., Iyer, K., Planke, S., 2018. Sills and gas generation in the Siberian Traps. *Philos. Trans. R. Soc. A Math. Phys. Eng. Sci.* 376, 20170080.
- Thibodeau, A.M., Bergquist, B.A., 2017. Do mercury isotopes record the signature of massive volcanism in marine sedimentary records? *Geology* 45, 95–96.
- Thibodeau, A.M., Ritterbush, K., Yager, J.A., West, A.J., Ibarra, Y., Bottjer, D.J., Berelson, W.M., Bergquist, B.A., Corsetti, F.A., 2016. Mercury anomalies and the timing of biotic recovery following the end-Triassic mass extinction. *Nat. Commun.* 7, 11147.
- Tierney, K.E., 2010. Carbon and strontium isotope stratigraphy of the Permian from Nevada and China: Implications from an icehouse to greenhouse transition. Ph.D. Thesis, The Ohio State University.
- Tomasca, P.B., 2004. Developments in the understanding and application of lithium isotopes in the earth and planetary sciences. *Reviews in Mineralogy & Geochemistry* 55, 153–195.
- Tomasca, P.B., Magna, T., Dohmen, R., 2016. *Advances in Lithium Isotope Geochemistry*. Springer International Publishing, Switzerland.
- Tong, J.N., Zuo, J.X., Chen, Z.Q., 2007. Early Triassic carbon isotope excursions from South China: proxies for devastation and restoration of marine ecosystems following the end-Permian mass extinction. *Geol. J.* 42, 371–389.
- Tran, T.H., Lan, C.Y., Usuki, T., Shellnutt, J.G., Pham, T.D., Tran, T.A., Pham, N.C., Ngo, T.P., Izokh, A.E., Borisenko, A.S., 2015. Petrogenesis of Late Permian silicic rocks of Tu Le basin and Phan Si Pan uplift (NW Vietnam) and their association with the Emeishan large igneous province. *J. Asian Earth Sci.* 109, 1–19.
- Urey, H.C., Lowenstam, H.A., Epstein, S., McKinney, C.R., 1951. Measurement of paleotemperatures and temperatures of the Upper Cretaceous of England, Denmark, and the southeastern United States. *Geol. Soc. Am. Bull.* 62, 399–416.
- Usui, Y., Tian, W., 2017. Paleomagnetic directional groups and paleointensity from the flood basalts in the Tarim large igneous province: implications for eruption frequency. *Earth, Planets and Space* 69, 14.
- Usuki, T., Lan, C.Y., Tran, T.H., Pham, T.D., Wang, K.L., Shellnutt, G.J., Chung, S.L., 2015. Zircon U-Pb ages and Hf isotopic compositions of alkaline silicic magmatic rocks in the

- Phan Si Pan-Tu Le region, northern Vietnam: Identification of a displaced western extension of the Emeishan Large Igneous Province. *J. Asian Earth Sci.* 97, 102–124.
- Vasil'ev, Y.R., Zolotukhin, V.V., Feoktistov, G.D., Prusskaya, S.N., 2000. Evaluation of the volumes and genesis of Permo-Triassic trap magmatism on the Siberian Platform. *Geol. Geofiz.* 41, 1696–1705.
- Veizer, J., Prokoph, A., 2015. Temperatures and oxygen isotopic composition of Phanerozoic oceans. *Earth Sci. Rev.* 146, 92–104.
- Veizer, J., Ala, D., Azmy, K., Bruckschen, P., Buhl, D., Bruhn, F., Carden, G.A.F., Diener, A., Ebnet, S., Godderis, Y., Jasper, T., Korte, C., Pawellek, F., Podlaha, O.G., Strauss, H., 1999. $^{87}\text{Sr}/^{86}\text{Sr}$, $\delta^{13}\text{C}$ and $\delta^{18}\text{O}$ evolution of Phanerozoic seawater. *Chem. Geol.* 161, 59–88.
- Viglietti, P.A., Frei, D., Rubidge, B.S., Smith, R.M.H., 2018. U-Pb detrital zircon dates and provenance data from the Beaufort Group (Karoo Supergroup) reflect sedimentary recycling and air-fall tuff deposition in the Permo-Triassic Karoo foreland basin. *J. Afr. Earth Sci.* 143, 59–66.
- Villier, L., Korn, D., 2004. Morphological disparity of ammonoids and the mark of Permian mass extinctions. *Science* 306, 264–266.
- Visscher, H., Looy, C.V., Collinson, M.E., Brinkhuis, H., van Konijnenburg-van Cittert, J.H.A., Kurschner, W.M., Sephton, M.A., 2004. Environmental mutagenesis during the end-Permian ecological crisis. *Proc. Natl. Acad. Sci. U. S. A.* 101, 12952–12956.
- Walker, J.C.G., Hays, P.B., Kasting, J.F., 1981. A negative feedback mechanism for the long-term stabilization of Earth's surface temperature. *J. Geophys. Res. Oceans* 86, 9776–9782.
- Wang, C.Y., Zhou, M.F., Qi, L., 2007. Permian flood basalts and mafic intrusions in the Jinping (SW China) Song Da (northern Vietnam) district: Mantle sources, crustal contamination and sulfide segregation. *Chem. Geol.* 243, 317–343.
- Wang, M., Zhong, Y.T., Hou, Y.L., Shen, S.Z., Xu, Y.G., He, B., 2018a. Source and extent of the felsic volcanic ashes at the Permian-Triassic boundary in South China. *Acta Petrol. Sin.* 34, 36–48 (in Chinese).
- Wang, W., Cao, C.Q., Wang, Y., 2004. The carbon isotope excursion on GSSP candidate section of Lopingian-Guadalupian boundary. *Earth Planet. Sci. Lett.* 220, 57–67.
- Wang, W.Q., Garbelli, C., Zheng, Q.F., Chen, J., Liu, X.C., Wang, W., Shen, S.Z., 2018b. Permian $^{87}\text{Sr}/^{86}\text{Sr}$ chemostratigraphy from carbonatic sequences in South China. *Palaeogeogr. Palaeoclimatol. Palaeoecol.* 500, 84–94.
- Wang, X.D., Sugiyama, T., 2000. Diversity and extinction patterns of Permian coral faunas of China. *Lethaia* 33, 285–294.
- Wang, X.D., Wang, X.J., Zhang, F., Zhang, H., 2006. Diversity patterns of Carboniferous and Permian rugose corals in South China. *Geol. J.* 41, 329–343.
- Wang, X.D., Cawood, P.A., Zhao, H., Zhao, L.S., Grasby, S.E., Chen, Z.Q., Wignall, P.B., Lv, Z.Y., Han, C., 2018c. Mercury anomalies across the end Permian mass extinction in South China from shallow and deep water depositional environments. *Earth Planet. Sci. Lett.* 496, 159–167.
- Wang, X.D., Cawood, P.A., Zhao, L.S., Chen, Z.Q., Lyu, Z.Y., Ma, B., 2019. Convergent continental margin volcanic source for ash beds at the Permian-Triassic boundary, South China: Constraints from trace elements and Hf-isotopes. *Palaeogeogr. Palaeoclimatol. Palaeoecol.* 519, 154–165.
- Wang, Y., Sadler, P.M., Shen, S.Z., Erwin, D.H., Zhang, Y.C., Wang, X.D., Wang, W., Crowley, J.L., Henderson, C.M., 2014. Quantifying the process and abruptness of the end-Permian mass extinction. *Paleobiology* 40, 113–129.
- Wei, H.Y., Wei, X.M., Qiu, Z., Song, H.Y., Shi, G., 2016. Redox conditions across the G-L boundary in South China: evidence from pyrite morphology and sulfur isotopic compositions. *Chem. Geol.* 440, 1–14.
- Wei, X., Xu, Y.G., Feng, Y.X., Zhao, J.X., 2014. Plume-Lithosphere Interaction in the Generation of the Tarim Large Igneous Province, NW China: Geochronological and Geochemical Constraints. *Am. J. Sci.* 314, 314–356.
- Wenzel, B., Lecuyer, C., Joachimski, M.M., 2000. Comparing oxygen isotope records of Silurian calcite and phosphate– $\delta^{18}\text{O}$ compositions of brachiopods and conodonts. *Geochim. Cosmochim. Acta* 64, 1859–1872.
- Wignall, P.B., 2001. Large igneous provinces and mass extinctions. *Earth Sci. Rev.* 53, 1–33.
- Wignall, P.B., 2007. The End-Permian mass extinction – how bad did it get? *Geobiology* 5, 303–309.
- Wignall, P.B., Hallam, A., 1992. Anoxia as a cause of the Permian/Triassic mass extinction: facies evidence from northern Italy and the western United States. *Palaeogeogr. Palaeoclimatol. Palaeoecol.* 93, 21–46.
- Wignall, P.B., Twitchett, R.J., 1996. Oceanic anoxia and the end Permian mass extinction. *Science* 272, 1155–1158.
- Wignall, P.B., Newton, R., Brookfield, M.E., 2005. Pyrite framboid evidence for oxygen-poor deposition during the Permian-Triassic crisis in Kashmir. *Palaeogeogr. Palaeoclimatol. Palaeoecol.* 216, 183–188.
- Wignall, P.B., Sun, Y.D., Bond, D.P.G., Izon, G., Newton, R.J., Vedrine, S., Widdowson, M., Ali, J.R., Lai, X.L., Jiang, H.S., Cope, H., Bottrell, S.H., 2009. Volcanism, mass extinction, and carbon isotope fluctuations in the Middle Permian of China. *Science* 324, 1179–1182.
- Wu, Q., Ramezani, J., Zhang, H., Wang, T.T., Yuan, D.X., Mu, L., Zhang, Y.C., Li, X.H., Shen, S.Z., 2017. Calibrating the Guadalupian Series (Middle Permian) of South China. *Palaeogeogr. Palaeoclimatol. Palaeoecol.* 466, 361–372.
- Xiang, L., Schoepfer, S.D., Zhang, H., Yuan, D.X., Cao, C.Q., Zheng, Q.F., Henderson, C.M., Shen, S.Z., 2016. Oceanic redox evolution across the end-Permian mass extinction at Shangsi, South China. *Palaeogeogr. Palaeoclimatol. Palaeoecol.* 448, 59–71.
- Xiao, L., Xu, Y.G., Chung, S.L., He, B., Mei, H.J., 2003. Chemostratigraphic Correlation of Upper Permian Lavas from Yunnan Province, China: Extent of the Emeishan Large Igneous Province. *Int. Geol. Rev.* 45, 753–766.
- Xiao, L., Xu, Y.G., Mei, H.J., Zheng, Y.F., He, B., Pirajno, F., 2004a. Distinct mantle sources of low-Ti and high-Ti basalts from the western Emeishan large igneous province, SW China: implications for plume-lithosphere interaction. *Earth Planet. Sci. Lett.* 228, 525–546.
- Xiao, L., Xu, Y.G., Xu, J.F., He, B., Franco, P., 2004b. Chemostratigraphy of flood basalts in the Garze-Litang region and Zongza Block: Implications for western extension of the Emeishan Large Igneous Province, SW China. *Acta Geologica Sinica-English Edition* 78, 61–67.
- Xiao, Y.F., Wu, K., Tian, L., Benton, M.J., Du, Y., Yang, H., Tong, J.N., 2018. Framboidal pyrite evidence for persistent low oxygen levels in shallow-marine facies of the Nanpanjiang Basin during the Permian-Triassic transition. *Palaeogeogr. Palaeoclimatol. Palaeoecol.* 511, 243–255.
- Xie, S.C., 2018. The shift of biogeochemical cycles indicative of the progressive marine ecosystem collapse across the Permian-Triassic boundary: an analog to modern oceans. *SCIENCE CHINA Earth Sciences* 61, 1379–1383.
- Xie, S.C., Pancost, R.D., Yin, H.F., Wang, H.M., Evershed, R.P., 2005. Two episodes of microbial change coupled with Permo/Triassic faunal mass extinction. *Nature* 434, 494–497.
- Xie, S.C., Pancost, R.D., Huang, J.H., Wignall, P.B., Yu, J.X., Tang, X.Y., Chen, L., Huang, X.Y., Lai, X.L., 2007. Changes in the global carbon cycle occurred as two episodes during the Permian-Triassic crisis. *Geology* 35, 1083–1086.
- Xu, G.Z., Deconinck, J.F., Feng, Q.L., Baudin, F., Pellenard, P., Shen, J., Bruneau, L., 2017a. Clay mineralogical characteristics at the Permian-Triassic Shangsi section and their paleoenvironmental and/or paleoclimatic significance. *Palaeogeogr. Palaeoclimatol. Palaeoecol.* 474, 152–163.
- Xu, G.Z., Feng, Q.L., Deconinck, J.F., Shen, J., Zhao, T.Y., Young, A.L., 2017b. High-resolution clay mineral and major elemental characterization of a Permian-Triassic terrestrial succession in southwestern China: Diagenetic and paleoclimatic/paleoenvironmental significance. *Palaeogeogr. Palaeoclimatol. Palaeoecol.* 481, 77–93.
- Xu, Y.G., Chung, S.L., Jahn, B.M., Wu, G.Y., 2001. Petrologic and geochemical constraints on the petrogenesis of Permian-Triassic Emeishan flood basalts in southwestern China. *Lithos* 58, 145–168.
- Xu, Y.G., Wei, X., Luo, Z.Y., Liu, H.Q., Cao, J., 2014. The Early Permian Tarim Large Igneous Province: Main characteristics and a plume incubation model. *Lithos* 204, 20–35.
- Yan, D.T., Zhang, L.Q., Qiu, Z., 2013. Carbon and sulfur isotopic fluctuations associated with the end-Guadalupian mass extinction in South China. *Gondwana Res.* 24, 1276–1282.
- Yang, J.H., Cawood, P.A., Du, Y.S., Condon, D.J., Yan, J.X., Liu, J.Z., Huang, Y., Yuan, D.X., 2018. Early Wuchiapingian cooling linked to Emeishan basaltic weathering? *Earth Planet. Sci. Lett.* 492, 102–111.
- Yin, H.F., Huang, S., Zhang, K.X., Hansen, H.J., Yang, F.Q., Ding, M.H., Bie, X.M., 1992. The effects of volcanism on the Permo-Triassic mass extinction in South China. In: Sweet, W.C., Yang, Z.Y., Dickins, J.M., Ying, H.F. (Eds.), *Permo-Triassic Events in the Eastern Tethys*. Cambridge University Press, Cambridge, pp. 146–157.
- Yin, H.F., Feng, Q.L., Lai, X.L., Baud, A., Tong, J.N., 2007. The protracted Permo-Triassic crisis and multi-episode extinction around the Permian-Triassic boundary. *Glob. Planet. Chang.* 55, 1–20.
- Yin, H.F., Jiang, H.S., Xia, W.C., Feng, Q.L., Zhang, N., Shen, J., 2014. The end-Permian regression in South China and its implication on mass extinction. *Earth Sci. Rev.* 137, 19–33.
- Yin, R.S., Feng, X.B., Chen, B.W., Zhang, J.J., Wang, W.X., Li, X.D., 2015. Identifying the sources and processes of mercury in subtropical estuarine and ocean sediments using Hg isotopic composition. *Environmental Science & Technology* 49, 1347–1355.
- Yuan, D.X., Shen, S.Z., Henderson, C.M., Chen, J., Zhang, H., Feng, H.Z., 2014. Revised conodont-based integrated high-resolution timescale for the Changhsingian Stage and end-Permian extinction interval at the Meishan sections, South China. *Lithos* 204, 220–245.
- Yuan, D.X., Shen, S.Z., Henderson, C.M., 2017. Revised Wuchiapingian conodont taxonomy and succession of South China. *J. Paleontol.* 91, 1199–1219.
- Yuan, D.X., Shen, S.Z., Henderson, C.M., Chen, J., Zhang, H., Zheng, Q.F., Wu, H.C., 2019. Integrative timescale for the Lopingian (late Permian): a review and update from Shangsi, South China. *Earth Sci. Rev.* 188, 190–209.
- Zaffos, A., Finnegan, S., Peters, S.E., 2017. Plate tectonic regulation of global marine animal diversity. *Proc. Natl. Acad. Sci. U. S. A.* 114, 5653–5658.
- Zeng, J., Cao, C.Q., Davydov, V.I., Shen, S.Z., 2012. Carbon isotope chemostratigraphy and implications of paleoclimate changes during the Cisuralian (Early Permian) in the southern Urals, Russia. *Gondwana Res.* 21, 601–610.
- Zhang, F.F., Algeo, T.J., Romanelli, S.J., Cui, Y., Zhao, L.S., Chen, Z.Q., Anbar, A.D., 2018a. Congruent Permian-Triassic $\delta^{238}\text{U}$ records at Panthalassic and Tethyan sites: Confirmation of global-oceanic anoxia and validation of the U-isotope paleoredox proxy. *Geology* 46, 327–330.
- Zhang, F.F., Romanelli, S.J., Algeo, T.J., Lau, K.V., Clapham, M.E., Richoz, S., Herrmann, A.D., Smith, H., Horacek, M., Anbar, A.D., 2018b. Multiple episodes of extensive marine anoxia linked to global warming and continental weathering following the latest Permian mass extinction. *Sci. Adv.* 4, e1602921.
- Zhang, G.J., Zhang, X.L., Li, D.D., Farquhar, J., Shen, S.Z., Chen, X.Y., Shen, Y.A., 2015. Widespread shoaling of sulfidic waters linked to the end-Guadalupian (Permian) mass extinction. *Geology* 43, 1091–1094.
- Zhang, G.J., Zhang, X.L., Hu, D.P., Li, D.D., Algeo, T.J., Farquhar, J., Henderson, C.M., Qin, L.P., Shen, M., Shen, D., Schoepfer, S.D., Chen, K.F., Shen, Y.A., 2017. Redox chemistry changes in the Panthalassic Ocean linked to the end-Permian mass extinction and delayed Early Triassic biotic recovery. *Proc. Natl. Acad. Sci. U. S. A.* 114, 1806–1810.
- Zhang, H., Cao, C.Q., Liu, X.L., Mu, L., Zheng, Q.F., Liu, F., Xiang, L., Liu, L.J., Shen, S.Z., 2016. The terrestrial end-Permian mass extinction in South China. *Palaeogeogr. Palaeoclimatol. Palaeoecol.* 448, 108–124.
- Zhang, Y., Ren, Z.Y., Xu, Y.G., 2013. Sulfur in olivine-hosted melt inclusions from the Emeishan picrites: Implications for S degassing and its impact on environment. *Journal of Geophysical Research-Solid Earth* 118, 4063–4070.
- Zhang, Y.C., Wang, Y., 2018. Permian fusuline biostratigraphy, in: Lucas, S.G., Shen, S.Z. (Eds.), *The Permian Timescale*. Geol. Soc. Lond. Spec. Publ. 450, 253–288.
- Zhao, M.Y., Zheng, Y.F., 2015. The intensity of chemical weathering: Geochemical constraints from marine detrital sediments of Triassic age in South China. *Chem. Geol.* 391, 111–122.

- Zhao, T., Algeo, T.J., Feng, Q., Zi, J.-W., Xu, G., 2019. Tracing the provenance of volcanic ash in Permian-Triassic boundary strata, South China: Constraints from inherited and syn-depositional magmatic zircons. *Palaeogeogr. Palaeoclimatol. Palaeoecol.* 516, 190–202.
- Zheng, W., Gilleadeau, G.J., Kah, L.C., Anbar, A.D., 2018. Mercury isotope signatures record photic zone euxinia in the Mesoproterozoic ocean. *Proc. Natl. Acad. Sci. U. S. A.* 115, 10594–10599.
- Zhong, H., Zhu, W.G., 2006. Geochronology of layered mafic intrusions from the Pan-Xi area in the Emeishan large igneous province, SW China. *Mineral. Deposita* 41, 599–606.
- Zhong, Y.T., He, B., Xu, Y.G., 2013. Mineralogy and geochemistry of claystones from the Guadalupian-Lopingian boundary at Penglaitan, South China: Insights into the pre-Lopingian geological events. *J. Asian Earth Sci.* 62, 438–462.
- Zhong, Y.T., He, B., Mundil, R., Xu, Y.G., 2014. CA-TIMS zircon U-Pb dating of felsic ignimbrite from the Binchuan section: Implications for the termination age of Emeishan large igneous province. *Lithos* 204, 14–19.
- Zuo, J.X., Tong, J.N., Qiu, H., Zhao, L.S., 2006. Carbon isotope composition of the Lower Triassic marine carbonates, lower Yangtze Region, South China. *Sci. China Ser. D Earth Sci.* 49, 225–241.



Dr. Yi-gang Xu is a research professor at Guangzhou Institute of Geochemistry, Chinese Academy of Sciences (GIGCAS). He graduated with a B.Sc. degree in Geochemistry from Zhejiang University in 1987, Ph.D. in Geochemistry from University of Paris 7 in 1994. From 1994 to 1995 he worked as a Postdoctoral Research Fellow at Royal Holloway, University of London, and joined GIGCAS in 1996. Dr. Xu is interested in lithospheric evolution of North China Craton, Permian large igneous provinces (Emeishan and Tarim) and their economic and environmental impact, and the big mantle wedge system under eastern Asia. He has published over 200 scientific papers, with a H-index of 60 (Google Scholar).



Dr. Jun Chen is an assistant research professor at Guangzhou Institute of Geochemistry, Chinese Academy of Sciences (GIGCAS). He obtained his Ph.D. degree in Palaeontology and Stratigraphy from Nanjing Institute of Geology and Palaeontology, Chinese Academy of Sciences (NIGPAS) in 2011. His main research interests include Permian biostratigraphy and palaeontology, palaeotemperature reconstruction using biogenic apatite, and large igneous provinces and their environmental and biological impact.